MONTE CARLO SIMULATIONS OF NUCLEATION OF COLLOIDAL CRYSTALS

Dissertation

zur Erlangung des Grades
„Doktor der Naturwissenschaften“
am Fachbereich Physik, Mathematik und Informatik
der Johannes Gutenberg-Universität Mainz

vorgelegt von
Antonia Statt
geboren in Bad Kreuznach

Mainz, 30. April 2015

JOHANNES GUTENBERG
UNIVERSITÄT MAINZ

Tag der Prüfung: 17.09.2015

ABSTRACT

A crystal nucleus existing in a finite volume may exhibit phase coexistence with a surrounding fluid if the total density of the system exceeds the onset density of freezing. When a crystal nucleus is surrounded by the coexisting fluid in a finite volume in thermal equilibrium, the thermodynamic properties of the fluid, i. e. pressure and chemical potential, are enhanced relative to their coexistence values in a infinite volume. This enhancement is uniquely related to the surface excess free energy of the nucleus.

In this thesis, a model for weakly attractive soft colloidal particles is investigated. We introduce an effective colloid-colloid potential, which is closely related to the Asakura-Oosawa model, although it has no discontinuities. We identify the crystal-fluid interface of the nucleus both on the particle level, using suitable bond order parameters to distinguish the phases, and by a finite size version of the lever rule. In simulations, this model allows for the calculation of the pressure in the liquid using the virial formula directly. A necessary element of the analysis, the pressure at phase coexistence in the thermodynamic limit, is obtained from the interface velocity method. We introduce a method by which the chemical potential in dense liquids can be measured in simulations of systems containing walls. The chemical potential in such systems is homogeneous even if the system is spatially inhomogeneous. One wall shows a rather long range repulsion and creates a region with low density, where the Widom particle insertion method can be applied.

There is neither a need to precisely locate the interface nor to compute the anisotropic interfacial tension to obtain nucleation barriers. Therefore, our analysis is appropriate for crystal nuclei of arbitrary shape. We show that the surface excess free energy can be determined accurately from Monte Carlo simulations over a wide range of nucleus' volumes and the resulting nucleation barriers are independent from the size of the total volume of the system. The classical nucleation theory assumes a spherical nucleus shape, which is not realized when the crystal nucleus is facetted. The interfacial tension can be determined via the ensemble switch method and hence a detailed test of classical nucleation theory is possible. We established that classical nucleation theory works for the model under consideration: The anisotropy of the interfacial tension for the crystals and their resulting non-spherical shape has only a minor effect on the barrier.

In addition, the structural crossover in the pair correlation function in fluid of binary mixtures is investigated. Monte Carlo simulations of a hard sphere fluid and experiments using two differently sized colloidal particles are carried out. We investigate the question whether the structural crossover in 3D is related to the percolation of the neighbour networks in the mixture.

ZUSAMMENFASSUNG

Ein Kristallisationskeim in einem endlichem Volumen kann sich in Phasenkoexistenz mit einer Flüssigkeit befinden, wenn die Gesamtdichte des Systems die Dichte am Gefrierpunkt übersteigt. Die thermodynamischen Eigenschaften der Flüssigkeit um den Keim, d.h. Druck und chemisches Potential, sind im Vergleich zu den Koexistenzwerten in einem unendlich großen System erhöht. Diese Verschiebung hin zu größeren Werten ist eindeutig mit der Oberflächenenergie des Keims verknüpft.

In dieser Arbeit wird ein Modell für schwach anziehende weiche kolloidale Teilchen betrachtet. Dazu wird ein stetiges effektives Potential, welches auf dem Asakura-Oosawa Modell basiert, eingeführt. Die Grenzfläche zwischen den Phasen wird auf der Ebene der Teilchen mit Hilfe von passenden Ordnungsparametern und durch eine Finite-Size Version der LEVER RULE bestimmt. Dieses Modell erlaubt es, auf einfache Weise den Druck in Simulationen unter Verwendung des Virial Theorems zu berechnen. Der Druck bei Phasenkoexistenz im thermodynamischen Limit wird durch die INTERFACE VELOCITY METHOD bestimmt, der für die Analyse benötigt wird. Es wird eine Methode eingeführt, mit der das chemische Potential in dichten Flüssigkeiten von Systemen mit Wänden gemessen werden kann. Obwohl diese Systeme räumlich inhomogen sind, ist das chemische Potential konstant. Eine im System vorhandene Wand führt zu einer langreichweitigen Abstoßung, und damit zu einer Region mit niedriger Dichte, in der dann die WIDOM PARTICLE INSERTION METHOD angewendet werden kann.

Um Nukleationsbarrieren zu erhalten, ist es nicht nötig die Grenzfläche genau zu lokalisieren oder die anisotrope Grenzflächenspannung zu berechnen. Daher ist unsere Methode zur Analyse von Kristallkeimen in beliebiger Form geeignet. Die Oberflächenenergie kann für einen großen Bereich verschiedener Keimgrößen in Monte-Carlo-Simulationen genau bestimmt werden. Das Ergebnis ist unabhängig von der Gesamtsystemgröße. Die klassische Keimbildungstheorie nimmt einen kugelförmigen Keim an, was für facettierte Kristallkeime nicht gegeben ist. Die Oberflächenspannung kann mit der ENSEMBLE SWITCH METHOD bestimmt werden und erlaubt so einen detaillierten Test der klassischen Keimbildungstheorie. Die klassische Keimbildungstheorie trifft auf das hier betrachtete Modell zu: Die Anisotropie der Oberflächenspannung des Kristalls und die resultierende von einer Kugel abweichende Form hat nur einen geringen Effekt auf die Keimbildungsbarriere.

Zusätzlich wird der strukturelle Übergang in der radialen Verteilungsfunktion von flüssigen binären Mischungen untersucht. Es wurden Monte-Carlo-Simulationen einer Hart-Kugel-Flüssigkeit und Experimente mit zwei verschieden großen kolloidalen Teilchen durchgeführt. Der Zusammenhang zwischen dem strukturellen Übergang in 3D und der Perkolation des Nachbar-Netzwerkes in der Mischung wird diskutiert.

PARTS OF THIS WORK WERE PUBLISHED IN:

[1] A. Winkler, D. Winter, P. Chaudhuri, A. Statt, P. Virnau, J. Horbach, and K. Binder, *Computer simulations of structure, dynamics, and phase behavior of colloidal fluids in confined geometry and under shear*, The European Physical Journal Special Topics, **222** (2013)

[2] B.J. Block, D. Deb, F. Schmitz, A. Statt, A. Tröster, A. Winkler, T. Zykova-Timan, P. Virnau and K. Binder, *Computer simulation of heterogeneous nucleation of colloidal crystals at planar walls*, The European Physical Journal Special Topics, **223** (2014)

[3] K. Binder, P. Virnau, and A. Statt, *Perspective: The Asakura-Oosawa model: A colloid prototype for bulk and interfacial phase behavior*, The Journal of Chemical Physics, **141** (2014)

[4] A. Statt, P. Virnau, and K. Binder, *Finite-Size Effects on Liquid-Solid Phase Coexistence and the Estimation of Crystal Nucleation Barriers*, Physical Review Letters, **114** (2015)

[5] A. Statt, P. Virnau, and K. Binder, *Crystal nuclei in melts: A Monte Carlo simulation of a model for attractive colloids*, Molecular Physics, in press (2015)

[6] A. Statt, F. Schmitz, P. Virnau, and K. Binder, *Monte Carlo Simulation of Crystal-Liquid Phase Coexistence*, The European Physical Journal Special Topics, submitted (2015)

CONTENTS

1 INTRODUCTION

Understanding condensed matter is a very challenging field of physics. Usually the systems under consideration are composed of many interacting elements and therefore, one has to deal with macroscopic systems. Quantities characterizing the system as a whole, such as pressure, temperature, or the chemical potential, are more interesting than single particle trajectories. Nevertheless, macroscopic properties of condensed matter systems depend strongly on the microscopic details of the underlying particle interactions.

Especially phase transitions and nucleation are a major topic in condensed matter physics. The latter is described by the so called Classical Nucleation Theory [1, 2] which was developed to describe the vapour-liquid transition in general [3]. One assumption is, that macroscopic properties of the system can be applied to describe microscopic droplets. Classical nucleation theory (CNT) has been utilized to describe crystallization of microscopically small nuclei, which violate the assumptions made by CNT [4]. Applications range from ice crystal formation in the atmosphere, to metallurgy, nanomaterials, and protein crystallization. Despite its vast importance and applications, crystal nucleation is still not fully understood on a quantitative level. Especially the question of how accurate the prediction for the nucleation rate is, has not been answered satisfactorily.

Nucleation rates determined in experiments and simulations are not in agreement, especially for low supersaturations. This discrepancy is still unsolved as stated in a recent review from Palberg [5]. For investigating the discrepancy between experimental results and simulation data, more knowledge about theoretical nucleation barriers is needed as well as for testing the approximations of CNT. Understanding the conditions under which the classical description holds will be useful to understand liquid-solid transitions in condensed matter in general.

Computer simulations are an appropriate tool to study nucleation from first principles [6–8]. Critical nuclei are hard to investigate in simulations, since their occurrence is connected to rare events when the system overcomes a maximum in the free energy surface [9–11]. In this case the nucleus grows from sub-critical to super-critical. Therefore, often the simulation of small nucleation barriers is possible [10, 12] only, whereas larger ones are desired for comparison with experimental results.

Computer simulations allow to connect microscopic properties such as particle interactions to macroscopic properties, such as Laplace pressure. This allows a direct comparison between simulations and experiments. On the other hand, results from simulations can be used to test predictions of approximate theories. Simulations are useful to develop new theories if there is no satisfying or confirmed theory for the behaviour of a system. Simulations therefore provide a

way to test experiments as well as approximations in theoretical models. Hence, computational physics can be seen as an intermediate branch between theoretical and experimental physics. In cases where exact equations are known, that can only be solved approximately, computational methods are often used. These methods become more and more important in many areas of science, for example weather forecasting, engineering and mathematics. Computer simulations are a well established part in the field of statistical mechanics. They are a useful part of the mathematical modeling of many systems of interest in physics, particularly for the study of phase transitions, e. g. nucleation.

An advantage of simulations is that, in principle, any system with specific conditions such as temperature and/or volume can be simulated. Polydispersity, impurities or particle shape anisotropy, can be excluded or investigated separately. One drawback is that computing time and resources are limited. The calculations are often restricted to interaction potentials between two particles and short range forces, so that the underlying theory either has to be simple or needs to be simplified for simulations. Another difference between experiment and simulation is the number of observed particles. Real systems typically contain particle numbers of the order 10^{23}, whereas simulations are often limited to several thousand particles, depending on the actual model and details of computation. Therefore, results from simulations differ from the results one would get for realistic system sizes. Although this difference is not physical, in the sense of the thermodynamic limit, these finite systems are a useful tool to understand physical phenomena like nucleation.

Complex phenomena require a simple model which allows us to focus on exactly those properties of interest, so that fundamental questions about the behaviour of the phenomenon can be answered. In order to study crystal nucleation by simulations, we require a simple model, which shows phase separation into a liquid-like and a solid-like phase.

Colloidal suspensions are good model systems for the study of phase separation and hence nucleation in condensed matter. Colloids are particles, which are typically sphere-like and of the size of µm, that are dispersed in a much smaller solvent. Due to their relatively large size, colloidal systems can be observed in experiments by confocal microscopy and scattering techniques with visible light [13]. Additionally, the rather large diameter of colloids is responsible for long time scales in the order of milliseconds or larger. The interactions of colloids can be tuned to a large extent in experiments, for example by adding salt to the solvent or by modifying their surface, e. g. by coating or grafting polymers. This way one can for example synthesize hard sphere-like systems which are frequently used in theoretical models [14].

Colloidal suspensions themselves can be regarded as models for atomistic systems. They are structurally comparable to an atomic gas and the particles develop short-ranged interactions similar to atoms [14], therefore they exhibit

similar behaviour, such as phase transitions and critical phenomena. We can see the application of colloidal systems in a wide variety of common applications including paints, coatings, ink, creams, foams, tooth paste, to name a few. Consequently, colloidal suspensions are suited to study phase separation, nucleation processes and wetting properties in experiments as well as in computer simulations.

The first part of this thesis in chapter 2 describes the simulation techniques and the underlying statistical mechanics. Especially important for this work is the phase transition in finite systems as explained in section 2.2. A crucial input into Monte Carlo simulations is the well defined model system. The applied models are explained in chapter 3 and their bulk phase behaviour is investigated in section 3.3. For the simulation of two phase coexistence, the ability to distinguish between phases is essential. For this purpose, bond orientational parameters are used and described in section 3.4. The classical nucleation theory is described in detail in chapter 4. The interfacial tension is one important part to calculate predictions from CNT. In computer simulations, the interfacial tension can be calculated by the Ensemble Switch method, which is discussed in section 4.3. For the calculation of the Laplace pressure the precise value of the coexistence pressure is needed. Estimates for the coexistence pressure are obtained by the interfacial velocity method in chapter 5. In chapter 6 the chemical potential in the liquid is calculated with Monte Carlo simulations. Therefore, a method for applying the Widom particle insertion method to dense liquids is introduced. The simulations of a crystal nucleus surrounded by liquid are described in detail in chapter 7 and a discussion of the volume of the nuclei can be found in section 7.2. Nucleation barriers and the Laplace pressure are calculated in section 7.4. Chapter 8 summarizes the obtained results and provides an outlook on the work presented in this thesis.

In collaboration with the group of Paddy Royall and Robert Evans at the University of Bristol the structural crossover of binary hard sphere mixtures were investigated. The preliminary results of this study can be found in Part II.

Part I

HOMOGENEOUS NUCLEATION

2 MONTE CARLO SIMULATIONS

In the following, basic expressions of statistical mechanics and their applications to computer simulations are derived and summarized. Monte Carlo simulations compute results via repeated random sampling and are typically used to study systems in thermal equilibrium and also for dynamical processes in systems where events occur stochastically distributed.

2.1 CLASSICAL STATISTICAL MECHANICS AND COMPUTER SIMULATIONS

A system with a constant number of particles N and a fixed volume V for a given temperature T is called CANONICAL ENSEMBLE. The energy of the system is determined by the temperature T, which is an intensive variable. The temperature is kept constant by coupling the system to a much bigger system, the so-called HEAT BATH and by allowing energy exchange between both systems. The canonical ensemble average of any property f(of the particle coordinates and momenta) is given by

$$\langle f \rangle = \frac{1}{h^{3N} N!} \int \mathrm{d}\mathbf{\Gamma}\, f(\mathbf{\Gamma}) P(\mathbf{\Gamma}) \quad , \tag{2.1}$$

where $P(\mathbf{\Gamma})$ is the probability to find the system in state $\mathbf{\Gamma}$. The phase space contains all possible states of all particles in a specific system and $\mathbf{\Gamma}$ indicates one point in phase space. For mechanical systems the phase space consists of all possible values of position $\mathbf{x}_i$ and momentum variables $\mathbf{p}_i$ of the particles i. In general, a complete microstate is defined by the values for all degrees of freedom of all particles and is represented by one point in the phase space. The probability to find the system in a particular state $\mathbf{\Gamma}$ is given by

$$P(\mathbf{\Gamma}) = \frac{1}{Z(N,V,T)} e^{-\beta \mathcal{H}(\mathbf{\Gamma})} \quad , \tag{2.2}$$

where the inverse temperature β is defined as $1/k_B T$ and $e^{-\beta\mathcal{H}}$ is the so-called Boltzmann factor. $\mathcal{H}(\mathbf{\Gamma})$ is the Hamiltonian of the system and $Z(N,V,T)$ is the partition function. $Z(N,V,T)$ plays the role of a normalization, ensuring that the probabilities for all states $\mathbf{\Gamma}$ sum up to $\sum P(\mathbf{\Gamma}) = 1$. Therefore, in classical mechanics $Z(N,V,T)$ is given by

$$Z(N,V,T) = \sum_{\text{all states}} e^{-\beta \mathcal{H}(\mathbf{\Gamma})} \quad . \tag{2.3}$$

The partition function contains all information about the system. An appropriate thermodynamic function is the Helmholtz free energy F of the system, which is given by

$$F = -k_B T \ln Z(N, V, T) \quad . \tag{2.4}$$

Equilibrium properties of the system can be calculated from the Helmholtz free energy, for example

$$\text{Pressure } p = -\left.\frac{\delta F}{\delta V}\right|_{N,T} \quad , \tag{2.5}$$

$$\text{Chemcial potential } \mu = \left.\frac{\delta F}{\delta N}\right|_{V,T} \quad , \text{ and} \tag{2.6}$$

$$\text{Entropy } S = -\left.\frac{\delta F}{\delta T}\right|_{N,V} \quad . \tag{2.7}$$

Therefore, it is desirable to know Z and calculate F and related quantities, as shown above. The partition function for the NVT-ensemble in Monte Carlo simulations of particles with interaction potential $U(\mathbf{s}^N, L)$ in a cubic box $V = L^3$ is given by

$$Z(N, V, T) = \frac{V^N}{\Lambda^{3N} N!} \int e^{-\beta U(\mathbf{s}^N, L)} \mathrm{d}\mathbf{s}^N \quad , \tag{2.8}$$

where $\Lambda = \sqrt{\frac{\beta h^2}{2\pi m}}$ is the thermal de Broglie wavelength of the particles. h is Planck's constant, m is the mass of one particle. The factor $N!$ takes into account, that the particles are identical. The particle coordinates $\mathbf{s}^N = \mathbf{s}_1, \mathbf{s}_2, \ldots, \mathbf{s}_N$ can be written in terms of the box length L

$$\mathbf{x}_i = L\mathbf{s}_i \quad \text{for} \quad i = 1, 2, \ldots, N \quad . \tag{2.9}$$

The interaction potential U is a function of real particle coordinates $\mathbf{x}_i$ and depends on $\mathbf{s}_i$ and hence on the box dimensions L as well. It is straightforward to extend these expressions to non cubic boxes. As derived in [15], the Helmholtz free energy F can be split into two contributions, the ideal gas part and the excess part. Also, the energy in a classical system can be expressed as a sum of a kinetic and a potential part.

$$F(N, T, V) = F_{\text{id}}(N, V, T) + F_{\text{ex}}(N, V, T) \quad , \tag{2.10}$$

where $F_{\mathrm{id}}(N,V,T)$ and $F_{\mathrm{ex}}(N,V,T)$ are given by

$$F_{\mathrm{id}}(N,V,T) = -k_B T \ln \frac{V^N}{\Lambda^{3N} N!} \quad \text{and} \tag{2.11}$$

$$F_{\mathrm{ex}}(N,V,T) = k_B T \ln \int e^{-\beta U(\mathbf{s}^N, L)} \mathrm{d}\mathbf{s}^N \quad . \tag{2.12}$$

Therefore, all thermodynamic quantities derived from the Helmholtz free energy can be expressed as a sum of kinetic (ideal) and configurational (excess) parts.

However, the partition function $Z(N,V,T)$ often cannot be calculated exactly, since the sum has to be taken over all possible states. The amount of states, e. g. the phase space size, depends on the dimensions of the system and the degrees of freedom for each particle. In general this will yield a very large number of states and is therefore not feasible for exact calculations. The aim of statistical physics is to compute mean values by calculating averages as seen in equation (2.1).

Computer simulations are based on the idea to approximate the exact equation (2.3) and replace the sum or the integral by a summation over a characteristic subset of the phase space. To generate this subset, Monte Carlo methods rely on drawing random numbers and sampling the system randomly. For the averages $\langle f \rangle$ in equations (2.1) and (2.8), one chooses randomly distributed points ν inside the integration area. From an arbitrarily chosen initial configuration a sequence of configurations is created by random variation of the configuration. Then the average $\langle f \rangle$ can be calculated by

$$\langle f \rangle \simeq \frac{1}{Z} \sum_{\nu=1}^{R} f(\mathbf{x}_\nu) e^{-\beta \mathcal{H}(\mathbf{x}_\nu)} \quad \text{with} \quad Z \simeq \sum_{\nu=1}^{R} e^{-\beta \mathcal{H}(\mathbf{x}_\nu)} \, , \tag{2.13}$$

where R is the number of sampling points. If the random points are distributed uniformly the method is called SIMPLE RANDOM SAMPLING [16].

Very unlikely configurations have almost no, or a very small contribution to these sums. In a more efficient Monte Carlo calculation these configurations should be suppressed. This can be achieved by a method known as IMPORTANCE SAMPLING. Details will be shown in the next section as well as the METROPOLIS method. The basic idea is not to accept all random configurations. The decision whether to accept or reject a particular configuration is made in such a way, that the equilibrium state is reached asymptotically. Even though different sequences of random numbers will give different results, the asymptotic averages will agree within the associated statistical error due to random sampling. Improvements can be obtained by extending the simulation time for a more precise estimate. The accuracy obtained by a Monte Carlo simulation depends on the number of samples. Hence, it is essential that the phase space

is covered sufficiently. More details can be found in the book by LANDAU and BINDER [15].

2.1.1 *Importance sampling and the Metropolis method*

Importance sampling methods generate configurations in such a way that configurations with a large contribution to these sums are sampled more frequently and configurations with smaller contributions are sampled less often. The random points for the calculation of averages $\langle f \rangle$ are chosen according to a probability function $P(\mathbf{\Gamma})$, which is not uniformly distributed. A reasonable choice for $P(\mathbf{\Gamma})$ is the probability density function of the canonical ensemble. The challenge is to generate configurations according to $P(\mathbf{\Gamma})$.

The METROPOLIS algorithm [17] is a MARKOV CHAIN Monte Carlo method to obtain a sequence of random samples from a probability distribution. Configurations are generated successively from the previous state. Future configurations depend only on the current state and not on the previous sequence of configurations. This type of stochastic process is called Markov chain. A Markov chain is a stochastic movement in phase space.

The basic concept of the Metropolis method is generic and can be applied to different applications. A common example is a simple particle displacement move in the canonical ensemble. Consider two states of the system of interest S_i and S_j in phase space, with different particle positions. One can define two flows,

$$\Phi_{\text{out}} = \sum_j P_i(n) W_{i \to j} \qquad \text{the flow out of state } S_i, \tag{2.14}$$

$$\Phi_{\text{in}} = \sum_j P_j(n) W_{j \to i} \qquad \text{and the flow into state } S_i, \tag{2.15}$$

where $W_{i \to j}$ is the transition rate from state S_i to state S_j. $P_i(n)$ is the probability of the system being in state S_i. In equilibrium these two flows must be equal,

$$\sum_j P_i(n) W_{i \to j} = \sum_j P_j(n) W_{j \to i} \ , \quad \text{obeyed by e. g. ,} \tag{2.16}$$

$$P_i(n) W_{i \to j} = P_j(n) W_{j \to i} \ . \tag{2.17}$$

The second, stricter equation (2.17) is known as DETAILED BALANCE. If detailed balance is fulfilled, the flows are equal. For a Monte Carlo move, the transition rate $W_{i\to j}$ can be expressed as

$$W_{i\to j} = \min\left[1, \frac{P_j(n)}{P_i(n)}\right] \tag{2.18}$$

which fulfils detailed balance (2.17). In a classical system the probability of occurrence of a state is given by

$$P_i(n) = \frac{1}{Z} e^{-\beta E_i}\,, \tag{2.19}$$

where Z is the partition function and E_i its energy. This probability often cannot be calculated exactly, since the denominator Z is hard to obtain. Here, the advantage of using a Markov chain becomes clear. After inserting equation (2.19), the transition rate simplifies to

$$W_{i\to j} = \min\left[1, e^{-\beta\Delta E}\right]\,, \tag{2.20}$$

and the partition function cancels out. As a consequence, only the energy difference $\Delta E = E_j - E_i$ between the states S_j and S_i is needed for calculating the relative probability between the two states. The local displacement follows these steps:

1. Choose an initial state S_0 and calculate its energy E_0
2. Pick a second state S_i by displacing a particle randomly
3. Calculate the energy change $\Delta E = E_0 - E_i$
   a) If $\Delta E < 0$, then change to state S_i
   b) If $\Delta E > 0$, generate a random number ν between 0 and 1
      If $\nu < e^{-\beta\Delta E}$ change to state S_i, otherwise stay in state S_0
4. Use the current state as initial state and repeat step (2)-(4)

For this algorithm the random number ν has to be chosen uniformly distributed in the range of $[0, 1]$. Note that a state is a point in phase space γ_i and choosing a new state means for instance to pick a random particle and calculate a trial position change for this particle, $\mathbf{x}_i + \Delta$.

The efficiency of the simulation depends on the acceptance rate of moves, or equally, on the average displacement of a particle Δ in a trial move. As stated in [18], optimal values for acceptance rates are between 20% and 50%. This window determines the average displacement for the random particle displacement moves. In practice, the displacement typically is adjusted during the

simulation between MC cycles to achieve an efficient simulation and to reach suitable acceptance rates.

2.1.2 *Pressure in simulations via the virial theorem*

Consider a system of volume V containing N particles, with an average density of $\rho = N/V$. The particles interact with each other according to the pair potential $U(\mathbf{r})$, which depends on the distance $\mathbf{r}$ of two particles. The pressure in statistical mechanics is defined by equation (2.5).

A method to determine the pressure in the liquid during a Monte Carlo simulation is to use the virial theorem. In three dimensions, this leads to

$$p = k_B T\rho + \frac{1}{3V}\Big\langle \sum_i \sum_{i<j} (\mathbf{r}_i - \mathbf{r}_j)\cdot \mathbf{f}_{ij}\Big\rangle \quad , \tag{2.21}$$

where $\mathbf{r}_i - \mathbf{r}_j$ is the distance between particles i and j. The force between the particles is given by $\mathbf{f}_i = \mathbf{f}(\mathbf{x}_i) = -\partial U/\partial \mathbf{x_i}$ and Newton's third law holds $\mathbf{f}_{ij} = -\mathbf{f}_{ji}$. The summation limits are taking into account that the distance between particles is symmetric.

In inhomogeneous systems, however, the pressure in general depends on the spatial direction and on the position r, where it is determined. In this case the pressure is a tensor. The virial theorem is not useful for measuring pressure in spatially inhomogeneous systems. Additionally, the virial expression is only applicable, if the particle interactions are pair wise and differentiable. This assumption is needed in the virial expression for the calculation of forces between the particles. For potentials with hard core interactions other methods are available as for example described in [19].

2.1.3 *Widom particle insertion method*

The chemical potential in computer simulations can be calculated with the WIDOM PARTICLE INSERTION METHOD [20, 21]. The chemical potential is defined as the change in free energy for the addition of one particle from $N-1$ to N, see equation (2.6)

$$\mu = \left.\frac{\delta F}{\delta N}\right|_{V,T} = -k_B T \ln \frac{Z(N,V,T)}{Z(N-1,V,T)} \tag{2.22}$$

for large number of particles N. It can be split in a similar way as the free energy for the canonical ensemble, leading to

$$\mu = \mu_{\text{id}} + \mu_{\text{ex}} \quad \text{with} \tag{2.23}$$

$$\mu_{\text{id}} = -k_B T \ln \frac{V}{(N+1)\Lambda^3} \qquad \text{and} \tag{2.24}$$

$$\mu_{\text{ex}} = -k_B T \ln \frac{\int e^{-\beta U(\mathbf{s}^N, L)} \mathrm{d}\mathbf{s}^N}{\int e^{-\beta U(\mathbf{s}^{N-1}, L)} \mathrm{d}\mathbf{s}^{N-1}} \quad , \tag{2.25}$$

where μ_{id} is the ideal gas part contribution and μ_{ex} denotes the excess chemical potential. The $\mathbf{s}^N$ are scaled particle coordinates. It is useful to define the so-called "virtual" energy, $\Delta U = U(\mathbf{s}^N, L) - U(\mathbf{s}^{N-1}, L)$ the energy change in the potential energy by changing the particle number in the system from $N-1$ to N. Hence, the quotient in μ_{ex} is given by an ensemble average over the coordinate of the N-th particle

$$\mu_{\text{ex}} = -k_B T \ln \langle e^{-\beta \Delta U} \rangle_N^{-1} \tag{2.26}$$

To sample this ensemble average, the Widom method inserts a "ghost" particle randomly into the system and calculates the energy ΔU of its interaction with the particles of the system. After the calculation of ΔU the "ghost" particle has to be removed. Thus, a NVT-ensemble simulation with normal particle displacement moves is performed and every n^{th} step a randomly generated $N+1$-th "ghost" particle is inserted, ΔU is calculated, and the "ghost" particle is removed. For the obtained values for ΔU the ensemble average over $e^{-\beta \Delta U}$ can be sampled

$$\langle e^{-\beta \Delta U} \rangle_N^{-1} = \frac{1}{M} \sum_{\nu=1}^{M} e^{-\beta \Delta U(\nu)} \tag{2.27}$$

with M insertions of "ghost" particles. Inserting equation (2.27) into (2.26) results in

$$\mu = -k_B T \ln \frac{V}{(N+1)\Lambda^3} - k_B T \ln \frac{1}{M} \sum_{\nu=1}^{M} e^{-\beta \Delta U(\nu)} \quad , \tag{2.28}$$

which provides a value for the chemical potential in computer simulations. At the same time, the virial theorem can be used to determine the pressure during the simulation. Combining the Widom particle insertion method and the virial theorem, the equation of state can be determined in the (η, μ) and (η, p)-plane directly without any additional simulations. However, the Widom particle insertion method allows the computation of μ only in the liquid phase and not in the solid.

2.1.4 *Boundary conditions*

Monte Carlo simulations are always performed in systems of finite size due to limited computational resources. One important question is, how to treat the "edges" of the simulation box. If particles at the box edges do not interact with the edge, particles are affected by the box edge and effects like layering can occur. If for instance the bulk behaviour is studied, boundary effects might lead to wrong results.

The boundaries of the simulation box can be effectively eliminated by wrapping opposite borders in each direction together, resulting in periodic boundary conditions. A particle leaving system on the right will reappear on the left. This can be thought of as having identical simulation boxes surrounding the system in every direction. In computer simulations, periodic boundary conditions are implemented in such a way, that if a particle leaves the box, it needs to re-enter at the corresponding point on the other side of the box. Distances between particles need to be calculated by the minimum possible distance in order to take care of the periodic boundary conditions.

If the chosen box dimensions are too small in comparison to particle size and interaction range, a particle can interact with its own image. Hence, the size of the simulation box in each spatial direction must be large enough to prevent periodic artefacts due to the non-physical topology. Because of the periodic nature of the system, it is not possible to see fluctuations bigger than the length L of the system. The correlation length is limited to a maximum value of $L/2$ and resultant properties of the system differ from those of the corresponding infinite system.

For simulations of crystals periodic boundary conditions need to be chosen to be compatible with the equilibrium lattice spacing in each spatial direction. Otherwise, the crystal exhibits a strain field, since it is deformed. This deformation can lead to systematic errors of unknown size in the calculations.

Effects which arise due to the finite system size are called FINITE SIZE EFFECTS. One simple way to check for finite size effects is to simulate with different volumes and search for systematic changes in the results. For details on this topic refer to LANDAU and BINDER [15].

2.2 PHASES AND PHASE TRANSITIONS IN FINITE SYSTEMS

A phase is a homogeneous region of the system, with no spatial variation in the average density ρ, energy, composition or other macroscopic properties. Additionally, phases can differ due to their structure, for example different crystallographic structures. A phase can be considered as a distinct part of the system, with boundaries that are interfaces to surrounding phases. Equilibrium of phases means, that there is more than one phase in the system present, which can exchange energy, volume and particles. Nevertheless, on average no phase should melt or grow in equilibrium. In this case, the chemical potential is at the coexistence value μ_{coex} in all phases. The relation between thermodynamic parameters for a system in equilibrium is known as the equation of state. For the variables pressure p, density ρ and temperature T, the equation of state f is given by

$$f(p, \rho, T) \equiv 0 \quad . \tag{2.29}$$

For these systems a pair of variables is enough to describe the macroscopic state of the system completely. Usually the equation of state is given in the (ρ, p)-plane. In a canonical ensemble the equilibrium state is the minimum value of the Helmholtz free energy.

A solid phase is characterized by the arrangement of its constituents. In this thesis, only crystalline solids are considered. That means the constituents are arranged in a periodic order. A crystal can have two-, three-, four- or sixfold symmetry. The lattice structure of a crystal is described by a Bravais lattice, which is a discrete set of all points having the form

$$\mathbf{R}_{i,j,k} = i\mathbf{a}_1 + j\mathbf{a}_2 + k\mathbf{a}_3 \quad , \tag{2.30}$$

where $\mathbf{a}_1, \mathbf{a}_2$ and $\mathbf{a}_3$ are the primitive vectors of the lattice and i, j, k are integers. Since the choice of primitive vectors is not unique, a lattice can also be described by a unit cell. If the unit cell is translated by all possible $\mathbf{R}_{i,j,k}$ it would fill the three dimensional space without vacancies or overlaps. In this work, the face centered cubic lattice (fcc) is most important, which has a sixfold symmetry. The unit cell is shown in the top row of figure 2.1. This special lattice has the highest coordination number possible, and therefore the highest packing fraction η one can achieve with identical hard spheres and no overlaps is given by $\eta = \sqrt{2}\pi/6 \approx 0.74$. In computer simulations, the crystal structure can be aligned to the vectors of the simulation box, as shown in the bottom row of figure 2.1. Denoted as (100)-orientation is the case where the (100) planes are perpendicular to the z-direction of the box, similar for (110) and (111) orientation. The liquid state of matter has no long range ordering and no fixed shape for fixed volume.

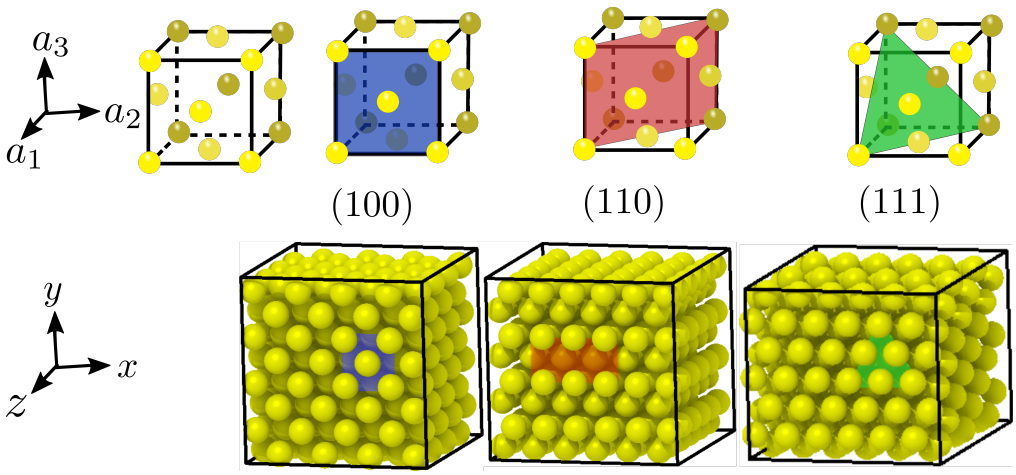

Figure 2.1: Top row: Unit cell with primitive vectors $\mathbf{a}_1, \mathbf{a}_2$ and $\mathbf{a}_3$ of the face centered cubic lattice. Particles are shown in yellow and are scaled for visibility. The (100), (110) and (111) planes are sketched and coloured. **Bottom row:** Examples for simulation boxes containing scaled particles. Here the (100), (110) and (111) directions are perpendicular to the z-direction. The planes are coloured corresponding to the top row.

As stated in section 2.1.4, the volume in a computer simulation is finite. Even though the edges of the volume are treated with periodic boundary conditions typically ,this leads to finite-size effects. One consequence of these finite-size effects is that intensive variables such as the chemical potential μ or the pressure p, exhibit "loops". In the thermodynamic limit of infinite large boxes, they must show a horizontal plateau throughout the two-phase coexistence region. The exact shape of the loop depends on the size of the simulation box and the periodic boundary conditions. Figure 2.2 gives a schematic sketch of such a "loop" for the chemical potential in a (very large) $L \times L \times L$ system with periodic boundary conditions. At phase coexistence, the system chooses a geometry, where the interface between the two phases is minimal. This behaviour gives rise to topological different configurations, depending on the volume fraction of the phases.

The following configurations are, as described by MacDowell et al. [22] for the related case of vapour-liquid coexistence:

$\rho < \rho_f$: The stable phase is a undersaturated liquid at these densities.

$\rho_f < \rho < \rho_1$: In a finite system of size L, the liquid is stable, up to a density of ρ_1, where it becomes metastable, the chemical potential is larger than the corresponding coexistence value, $\mu' > \mu_{\text{coex}}$.

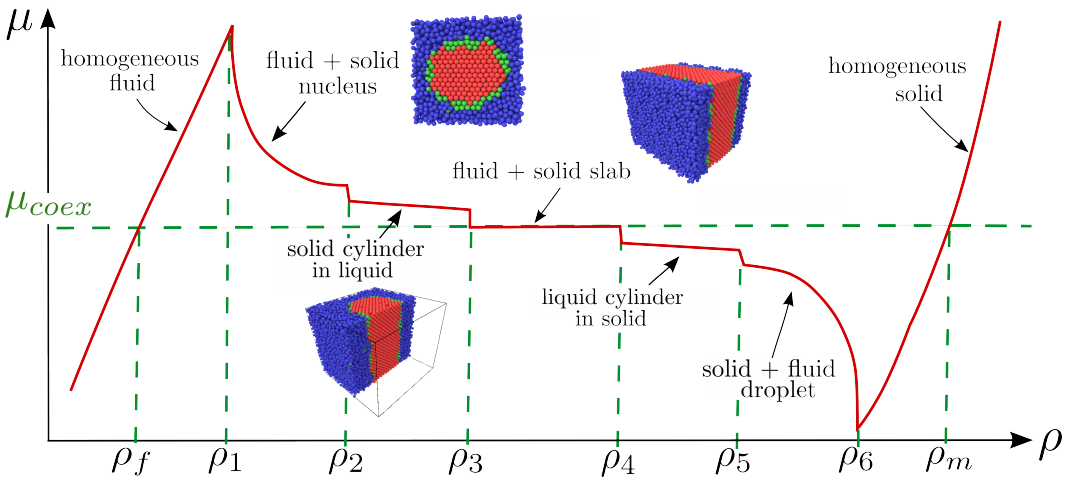

Figure 2.2: Schematic description of the loop in the chemical potential μ versus the packing fraction η. A liquid to solid transition in a finite but very large simulation box is shown. Snapshots show corresponding configurations, where liquid particles are coloured blue, solid particles are red and interface particles are green. Adapted from DEB et al. [19].

$\rho_1 < \rho < \rho_2$: A stable nucleus coexists with surrounding fluid of packing fraction η' and pressure p'. From densities ρ_1 to ρ_2 a single solid nucleus is formed.

$\rho_2 < \rho < \rho_3$: With increasing density, the droplet grows and eventually connects to itself over one periodic boundary. Due to this reason, the stable configuration between ρ_2 and ρ_3 is a cylindrically shaped solid phase surrounded by liquid.

$\rho_3 < \rho < \rho_4$: When the density is increased even further, both phases connect over two periodic boundaries and two planar interfaces are formed. This topological configuration is called a slab. Since the interface area does not change with density there is a large region of constant free energy in the range of $\rho_3 < \rho < \rho_4$, corresponding to the slab-like configuration. The pressure and the chemical potential are constant at their coexistence values p_{coex}, μ_{coex} throughout the system.

$\rho_4 < \rho < \rho_5$: For the solid side the same configurations occur but with exchanged roles of the phases due to symmetry. In this region, a liquid cylinder in a surrounding solid phase is the stable configuration.

$\rho_5 < \rho < \rho_6$: A liquid bubble in surrounding solid is formed.

$\rho < \rho_6$: For high enough densities, the stable phase is the solid phase and in the thermodynamic limit, melting starts at a density of ρ_m.

In contrast to infinitely large systems, in finite systems with periodic boundary conditions all of these states described above are thermodynamically stable. In the thermodynamic limit $L \to \infty$, the liquid is undersaturated for $\rho < \rho_f$, saturated for $\rho = \rho_f$, and supersaturated for $\rho_f < \rho < \rho_1$. The value ρ_f would be the onset density of crystallization. The same applies to the solid phase, but with exchanged densities, where ρ_m is the melting density.

Note, however, that the transitions between the various regions are not sharp but rounded. Finite size effects lead to smooth and shifted transitions due to the combined effects of boundaries and finite size [23, 24].

2.3 CHEMICAL POTENTIAL IN THE SOLID

In section 2.1.3 a method to determine the chemical potential in a liquid, a disordered state of matter, is shown. However, it is strictly true that in equilibrium μ is constant throughout the system, even if the system is not homogeneous. This can be used to calculate the chemical potential in the solid phase without determining it directly by simulations. The Maxwell relation is given by

$$\left.\frac{\partial \mu}{\partial p}\right|_{T,n} = \left.\frac{\partial V}{\partial n}\right|_{T,p} = v \quad , \tag{2.31}$$

where ν is the specific volume or volume per particle. Therefore, the chemical potential as a function of pressure is a linear function throughout one phase near coexistence, as shown in figure 2.3. Each phase has its own specific volume v_c and v_l, resulting in different slopes. In the liquid phase the density is lower, hence, the corresponding slope is larger than in the solid phase. The specific volumes are given by the corresponding packing fractions , $v_\mathrm{c} = \frac{\pi}{6}\eta_\mathrm{c}$ and $v_\mathrm{f} = \frac{\pi}{6}\eta_\mathrm{f}$. At coexistence, the pressure and the chemical potentials are the same, so the lines cross at $p_\mathrm{coex}, \mu_\mathrm{coex}$.

To find the chemical potential $\mu_\mathrm{c}(p_\mathrm{c})$ in the crystal phase, a thermodynamic integration of equation (2.31) is performed and the specific volume v_c is replaced with the packing fraction η_c, which results in

$$\mu_\mathrm{c}(p_\mathrm{c}) = \mu_\mathrm{coex} + \int_{p_\mathrm{coex}}^{p} v_\mathrm{c}\,\mathrm{d}p' = \mu_\mathrm{coex} + \int_{p_\mathrm{coex}}^{p} \frac{6\,\mathrm{d}p'}{\pi\,\eta_\mathrm{c}(p')} \quad . \tag{2.32}$$

For this integration $\mu_\mathrm{c}(p_\mathrm{coex}) = \mu_\mathrm{f}(p_\mathrm{coex})$ is used as starting point, since this value can be easily determined. The function $\eta_\mathrm{c}(p_\mathrm{c})$, which is needed to determine the integral (2.32), can be obtained in NVT-ensemble simulations of

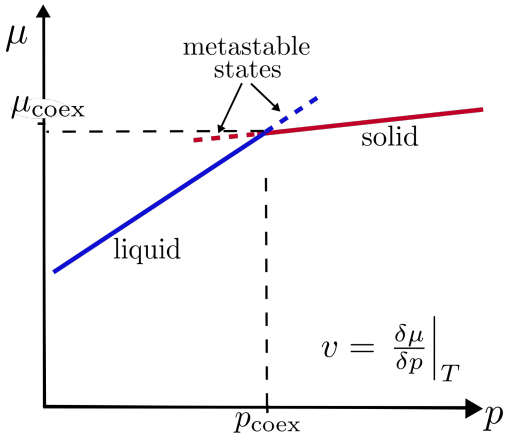

Figure 2.3: Sketch of the chemical potential μ as a function of pressure p close to the coexistence value in the NVT-ensemble. The slopes of the chemical potential are given by the specific volume v of the corresponding phase. The solid is shown in red and the liquid in blue. The lines cross at coexistence, at the values p_{coex} and μ_{coex} as indicated. The dashed parts indicate the metastable liquid and solid states.

a pure bulk solid phase. With this branch of the equation of state, $\mu_{\mathrm{c}}(\eta_{\mathrm{c}}(p_{\mathrm{c}}))$ can be calculated. The expansions

$$\mu_{\mathrm{c}}(p_{\mathrm{c}}) \approx \mu_{\mathrm{coex}} + v_{\mathrm{m}}(p_{\mathrm{c}} - p_{\mathrm{coex}}) \,, \tag{2.33}$$

$$\mu_{\mathrm{f}}(p_{\mathrm{f}}) \approx \mu_{\mathrm{coex}} + v_{\mathrm{f}}\,(p_{\mathrm{f}} - p_{\mathrm{coex}}) \,, \tag{2.34}$$

can be used to describe the chemical potential in both phases near the transition pressure p_{coex}.

2.4 THE ISOBARIC-ISOTHERMAL ENSEMBLE IN MONTE CARLO SIMULATIONS

The isobaric-isothermal NpT-ensemble can be seen as a system in thermal contact with a large reservoir. The system is coupled to the reservoir in such a way, that the volume can change in order to keep the pressure p at the same value as the reservoir. Therefore, the reservoir acts as a barostat. Energy exchange between the system and the reservoir is allowed fixing the temperature at a given value T. Particle exchange is not allowed, so that the number of particles N stays constant. To derive acceptance rules for volume fluctuations, the arguments given by FRENKEL and SMIT [18] are followed. As in equation (2.8) stated, the partition function of the canonical ensemble is given by

$$Z(N,V,T) = \frac{V^N}{\Lambda^{3N} N!} \int e^{-\beta U(\mathbf{s}^N, L)} \mathrm{d}\mathbf{s}^N \quad , \tag{2.35}$$

where $\mathbf{s}^N$ are the particle positions relative to the box size, analogous to equation (2.9). To change it to the NpT-ensemble, a canonical system is split into two subsystems according to the description of the NpT-ensemble given above.

The first is the subsystem of interest, the second system is the reservoir, a much larger ideal gas like system of volume V_0. Together they build a normal canonical ensemble. The total number of particles M is split between both subsystems, where $(M-N) \gg N$ particles are in the reservoir and N in the subsystem of volume V. The partition function of the total system is then given by the product of the two subsystems,

$$Z = \frac{V^N (V_0 - V)^{M-N}}{N!(M-N)!\Lambda^{3M}} \iint e^{-\beta U(\mathbf{s}^N, L)} \mathrm{d}\mathbf{s}^N \mathrm{d}\mathbf{s}'^{M-N} \quad , \tag{2.36}$$

where the ideal gas part interaction is zero, such that the corresponding integral leads to one. To calculate the contribution of the subsystem of interest, the partition function of the ideal gas reservoir needs to be isolated. The limit of a very large reservoir with fixed density ρ is useful, in which $V_0 \to \infty$, $M \to \infty$ and $(M-N)/V_0 = \rho$. This results in an approximation for

$$(V_0 - V)^{M-N} = V_0^{M-N} \left(1 - \frac{V}{V_0}\right)^{M-N} \approx V_0^{M-N} e^{-\frac{V}{V_0}(M-N)} \tag{2.37}$$

$$= V_0^{M-N} e^{-\rho V} = V_0^{M-N} e^{-\beta p V}, \tag{2.38}$$

using the ideal gas law $\rho V = \beta p V$. Equation (2.36) is integrated over the volume V and the ideal gas partition function,

$$Z_{\mathrm{id}}(M-N, V_0, T) = \frac{V_0^{M-N}}{(M-N)!\Lambda^{3(M-N)}} \quad , \tag{2.39}$$

is eliminated. Thus, the remaining part of equation (2.36) is the partition function of the NpT-ensemble. It reads as

$$Z(N, p, T) = \frac{\beta p}{\Lambda^{3N} N!} \int V^N e^{-\beta p V} e^{-\beta U(\mathbf{s}^N, L)} \mathrm{d}\mathbf{s}^N \mathrm{d}V \quad . \tag{2.40}$$

From this, it can be derived, that the probability to find a N particle system of volume V is proportional to

$$P(V) \sim V^N e^{-\beta p V} e^{-\beta U(\mathbf{s}^N, L)} \tag{2.41}$$

$$\sim e^{-\beta(-N k_B T \ln V + pV + U(\mathbf{s}^N, L))} \quad . \tag{2.42}$$

This probability $P(V)$ replaces the Boltzmann factor in the normal Monte Carlo particle displacement moves in section 2.1.1, if the Hamiltonian is considered to be a function not only of the particle coordinates $\mathbf{s}^N$, but also of the volume V or the box length L. Hence, one can modify the METROPOLIS METHOD to include volume changes which must satisfy the same rules as the particle displacement moves.

A Monte Carlo simulation in the NpT-ensemble follows this general algorithm:

1. Choose an initial state S_0 and perform normal Monte Carlo particle displacement moves at the initial volume V
2. Choose a new volume $V' = V + \Delta V$
3. Calculate the change of the Hamiltonian:
   $\Delta\mathcal{H} = U(\mathbf{s}^N, L) - U(\mathbf{s}^N, L') + p(V' - V) - k_B T N \ln(V'/V)$
   a) If $\Delta\mathcal{H} < 0$, then change to volume V'
   b) If $\Delta\mathcal{H} > 0$, generate a uniformly distributed random number ν between 0 and 1
      If $\nu < e^{-\beta\Delta\mathcal{H}}$ change to volume V', otherwise keep the old volume
4. Perform Monte Carlo particle displacement moves at the current volume
5. Use the current state as initial state S_0 and repeat step (1)-(4)

To choose a suitable new volume the system's details need to be considered. For an isotropic system, the box is usually cubic with volume $V = L^3$. The change ΔV in the volume can be picked from an uniformly distributed random number in the interval $[-\Delta V_{\max}, \Delta V_{\max}]$ such, that $V' = L'^3$. For anisotropic systems, the volume move needs to be anisotropic as well. The linear dimensions of the box $V = L_x \times L_y \times L_z$ can be considered to be independent and a volume move may change them separately. For simulations of slab like configurations (see figure 2.2 for densities between ρ_3 and ρ_4) a modification of the NpT-ensemble can be used. The system contains a liquid and a solid phase at the same time, where the solid spans over two periodic boundary directions, x and y. To avoid strains in the crystalline solid, these two spatial directions are kept fixed and are not allowed to fluctuate during the simulation. The remaining linear dimension L_z is changed by volume moves. This particular ensemble is called Np_zT-ensemble.

The ratio of normal Monte Carlo particle displacement moves to volume moves depends on the efficiency of the moves and on the particular application. A volume move in general requires that all interactions of all particles are recomputed, hence they scale with number of particles N. Therefore, we perform one attempt to change volume per N canonical moves in one Monte Carlo cycle.

3 MODEL SYSTEM

When studying complex physical systems, either in theory or by computer simulations, it is typically not possible to take all details (of the physical system) into account. So some simplifications are necessary. Therefore, we need a model system, which allows us to focus on specific effects, in which we are interested in. Effects occurring in experiments such as polydispersity, impurities or particle shape anisotropy, can be excluded or considered separately in computer simulations. Here, we only consider colloidal suspensions, which contain perfectly spherical particles of uniform size. Hence we need a coarse-grained model for colloidal particles in a non-absorbing polymer solvent. The main input to computer simulations are particle interactions, therefore the correct choice of the interaction potential is crucial. Colloid-polymer model systems are well-suited for computer simulations since the interaction between particles are short ranged.

Although the colloid-polymer model used in this thesis is quite simple, it is able to reproduce the phase behaviour of experimental colloid-polymer mixtures [25, 26]. In addition, this model was extensively investigated over the last years [27–29] and many properties are well known and understood. The existing publications provide a detailed check of code implementations and simulations. In the following we use a model for colloid-polymer mixtures, e. g. the Asakura-Oosawa model and extensions, which will be explained in the next section.

3.1 ASAKURA-OOSAWA MODEL

A simple model for colloid-polymer mixtures is the well known Asakura-Oosawa (AO) model [30, 31], which was proposed independently later by Vrij [32]. The AO model belongs to the 3D Ising universality class. Colloids are spheres with diameter σ_c, which interact with each other like hard spheres. The non-absorbing polymers are represented by spheres, which are allowed to overlap with each other with no energy costs, as illustrated in figure 3.1 (a) and (b). The diameter of a polymer σ_p is usually given by $2R_g$, where R_g is the radius of gyration of the polymer chain. The colloid-polymer interaction is then again hard sphere like.

According to these interactions, the energy of a valid configuration of particles is always zero and the temperature T is not a control parameter in this model. This choice of interactions causes an effective, purely entropy driven, depletion attraction between the colloid particles, although the pairwise colloid-colloid as well as the colloid-polymer interaction is purely repulsive. Based on the hard core interaction, a polymer center of mass cannot get closer to a colloid

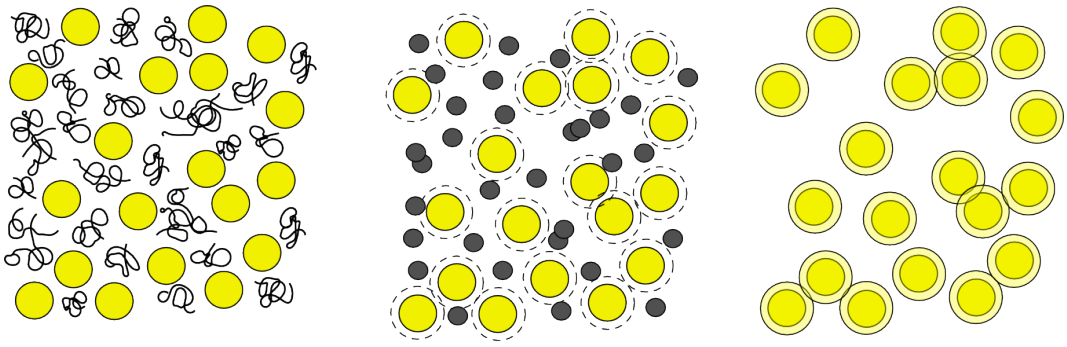

Figure 3.1: Schematic sketch of the AO model of a colloid-polymer mixture: **(a)** Large circles depict colloidal particles, polymers in the suspension are shown as black strings. **(b)** Polymers are replaced by soft spheres, which can overlap with each other but not with the colloids. The excluded zones, dotted curves, occur at a radius of $(\sigma_c + \sigma_p)/2$. **(c)** Plot indicates the effective pair potential between the colloids according to equation (3.4) that results, when the polymers are integrated out.

as $\sigma_c + \sigma_p$. Therefore, each colloid exhibits a zone without polymer centers of mass. This zone is called depletion zone and is indicated by dotted line around each colloid in figure 3.1 (b). The volume of the depletion zone in three dimensions is given by $V_\delta = \frac{4\pi}{3}(r_c + r_p)^3$. The free volume accessibly for a polymer is now reduced by V_δ for each colloid [32], if the depletion zones of the colloids are not overlapping each other. If the colloids are close to each other, their depletion zones are overlapping and the free volume available for a polymer increases and thereby the entropy of the polymers grows. Depending on the other parameters of the system the gain of entropy is sufficient to drive demixing.

The size ratio $q = \sigma_p/\sigma_c$ between colloids and polymers determines the range of the effective attraction, and the polymer concentration its strength. If the system is coupled to a polymer reservoir, the fugacity z_p of the polymers can be regarded as the equivalent of inverse temperature in a molecular system. The fugacity would be the polymer density in the reservoir for ideal polymers and is given by

$$z_p = \Lambda_p^{-3} e^{\beta\mu_p} \tag{3.1}$$

and the polymer reservoir packing fraction by

$$\eta_p^r = \frac{\pi}{6}\sigma_p^3 z_p \quad . \tag{3.2}$$

The thermodynamic properties of the system are controlled by the size ratio q and the colloid packing fraction

$$\eta_c = \frac{\pi \sigma_c^3}{6} \frac{N_c}{V} \quad , \tag{3.3}$$

completely, where N_c denotes the total number of colloid particles in the simulation volume V.

While the AO model can be used to describe colloid-polymer mixtures of arbitrary size ratios $q = \sigma_p/\sigma_c$, the focus of this work is on colloid-polymers mixtures, where the polymers are much smaller than the colloids. For a size ratio $q > 0.25$, there occurs a demixing in a vapour-like phase (poor in colloids) and a liquid like phase (rich in colloids) on a mean field level, if the volume fractions η_c and η_p are large enough, as shown by Aarts and Lekkekerker [33, 34]. For all values of q and all polymer concentrations the system shows a transition from fluid phase to a face-centred cubic (fcc) crystal at large colloid densities. In the limiting case when no polymers are present, the model reduces to the well known hard sphere system.

The AO model belongs to the class of asymmetric binary mixtures, which are in general difficult to simulate, especially if the size ratio is very small. The equilibration of such a highly asymmetric mixture is very slow, since there are a large number of polymers per colloid. We therefore use an effective AO model. The basic idea is, to replace the polymers completely by an attractive interaction of the colloids, as illustrated in figure 3.1(c).

3.2 EXTENSIONS TO THE ASAKURA-OOSAWA MODEL

3.2.1 *Effective Asakura-Oosawa model*

In the limit of a highly asymmetric mixture with very small polymers, the physical effect of the polymers can be replaced by an effective and attractive interaction between the colloids [35, 36]. This Hamiltonian is obtained by integrating out the polymers' degrees of freedom. This results in a one component system of colloidal particles, which reduces the computational effort substantially, since only one particle species has to be simulated. For a size ratio of $q >= 2/3^{1/2} - 1 \approx 0.1547$, this effective interaction is a sum of many-body interactions. For smaller size ratios there is no triple overlap of excluded volume

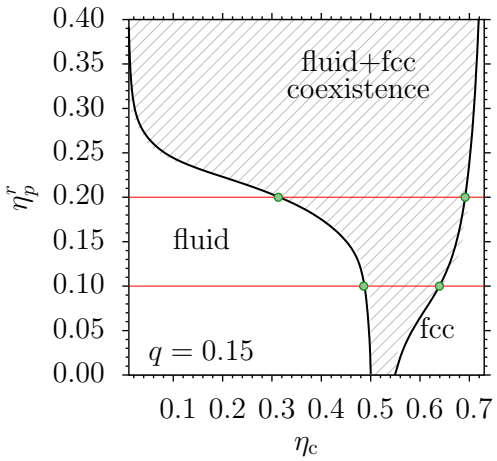

Figure 3.2: Schematic sketch of the phase diagram of an EffAO model in the (η_p^r,η_c)-plane for a colloid-polymer size ratio of $q = 0.15$, adapted from [34]. The used values for η_p^r are indicated with red lines and the green dots represent the corresponding η_m melting and η_f freezing packing fractions. The case of $\eta_p^r \equiv 0$ is exactly the limit of hard spheres without polymers.

regions [37, 38]. Therefore the bulk binary colloid-polymer mixture reduces to an interaction pair potential given by an polynomial in r/σ_c:

$$U_{\mathrm{EffAO}}(r) = \begin{cases} \infty & \text{for} \quad r \leq \sigma_c \\ -\eta_p^r \left(\frac{1+q}{q}\right)^3 \left[1 - \frac{3r}{2\sigma_c(1+q)} + \frac{r^3}{2\sigma_c^3(1+q)^3}\right] & \text{for} \quad \sigma_c < r < \sigma_c + \sigma_p \\ 0 & \text{for} \quad r \geq \sigma_c + \sigma_p \end{cases} , \tag{3.4}$$

where $r = |\mathbf{r}_i - \mathbf{r}_j|$ denotes the distance between the two colloids i and j. Figure 3.3 shows the potential. The strength of the potential can be controlled via the polymer reservoir packing fraction η_p^r. The interaction range on the other hand can be modified by the size ratio q. In experiments, this can be achieved by varying the concentration of polymers in the suspension and by choosing different molecular weights for the polymers [25, 39]. The potential strengths are in units of the thermal energy k_BT. The cutoff distance is given by $1 + q$. In this work, all lengths are measured in units of σ_c.

In figure 3.2, a phase diagram of the effective AO model (EffAO) in the (η_p^r, η_c)-plane is sketched. For $q = 0$ the hard sphere model is recovered. The two used values for $\eta_p^r = 0.1$ and 0.2 are marked with red horizontal lines. An increase of the polymer reservoir packing fraction broadens the region of two phase coexistence, which is useful for further analysis, since we perform simulations in the two phase coexistence region. The melting packing fraction η_m is moved to higher values and the freezing packing fraction η_f is shifted to lower values when η_p^r increases.

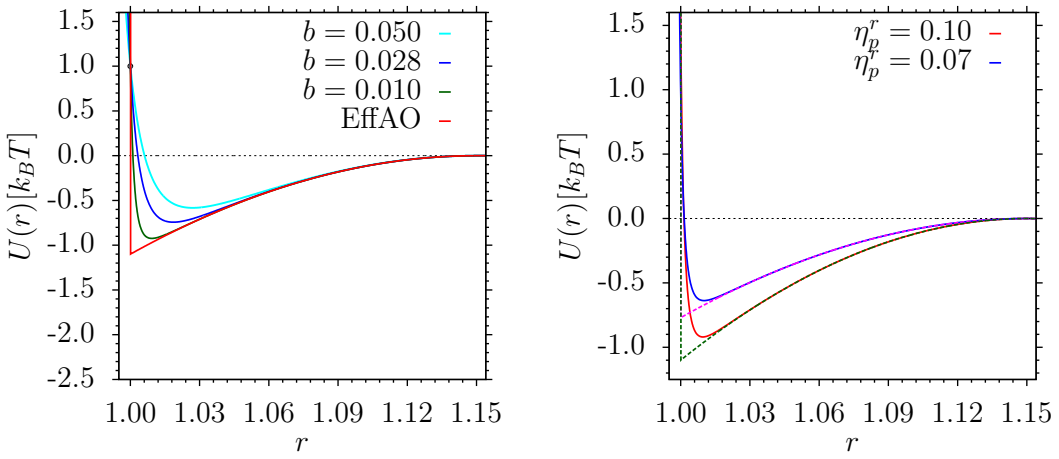

Figure 3.3: (a) Shapes of the EffAO model and the softEffAO model with $\eta_p^r = 0.1$ for different values for the parameter b and e. The parameter e is chosen in such way, that the value of the potential is 1 for $r = \sigma_c$. **(b)** The EffAO model (dashed lines) and its soft extension (full lines) for two choices of η_p^r as indicated. Corresponding values for e and b are $b = 0.01$ and $e = 0.988571$ for $\eta_p^r = 0.1$ and $b = 0.01$ and $e = 0.989200$ for $\eta_p^r = 0.2$.

3.2.2 *Soft effective Asakura-Oosawa model*

The EffAO model, as described above, has one big disadvantage, namely the hard sphere like interaction part, which makes the calculation of pressure difficult. Real colloidal particles are not strictly hard spheres [40, 41] and therefore there is no need to stick to the hard sphere interaction. Hence, we have developed a soft effective AO model (softEffAO), where the hard core interaction is replaced by a smooth function $U_{\text{rep}}(r)$, which is fitted to the EffAO model by two parameters. Another advantage of the purely soft potential is, that we can perform molecular dynamics simulations with the same potential, if necessary. We use the EffAO model with $q = 0.15$ and polymer reservoir packing fraction $\eta_p^r = 0.1$ for comparison, as shown in figure 3.3.

The new potential $U_{\text{softEffAO}}(r)$ consists of two parts, an attractive interaction,

$$U_{\text{attr}}(r) = -\eta_p^r \left(\frac{1+q}{q}\right)^3 \left[1 - \frac{3r}{2\sigma_c(1+q)} + \frac{r^3}{2\sigma_c^3(1+q)^3}\right] \tag{3.5}$$

which is identical to the EffAO model in the range of $\sigma_c < r < \sigma_c + \sigma_p$. The repulsive interaction U_{rep} replaces the hard core like interaction by

$$U_{rep}(r) = 4\left(\left[\frac{b\sigma}{r - e\sigma}\right]^{12} + \left[\frac{b\sigma}{r - e\sigma}\right]^{6} - \left[\frac{b\sigma}{\sigma + q - e\sigma}\right]^{12} - \left[\frac{b\sigma}{\sigma + q - e\sigma}\right]^{6} \right) \quad , \tag{3.6}$$

where $\sigma \equiv \sigma_c$ denotes the colloid diameter. The parameters b and e are controlling the strength and the zero crossing point of the repulsive part. We choose them in such way, that $U(r = \sigma_c) = 1$. Therefore, they depend on each other and we have selected $b = 0.01$ and $e = 0.988571$ for a polymer reservoir packing fraction of $\eta_p^r = 0.1$. The potential is shown for different sets of e and b in figure 3.3 (b). A small value for b results in a potential, which is closer to the the original effective AO model. Since we aim for a comparison between both models, a low value for b is preferred.

The complete colloid-colloid interaction potential is now given by

$$U_{\text{softEffAO}}(r) = \begin{cases} U_{rep}(r) + U_{attr}(r) & \text{for } r < \sigma_c + \sigma_p \\ 0 & \text{for } r \geq \sigma_c + \sigma_p \end{cases} \tag{3.7}$$

and is differentiable twice and has a cutoff of $1 + q$. For a polymer reservoir packing fraction of $\eta_p^r = 0$ this soft effective potential changes to a purely repulsive interaction potential. In the following, the softEffAO model is used mainly with two different values for η_p^r, the softEffAO1 model denotes the model with a polymer reservoir packing fraction of $\eta_p^r = 0.1$ and the softEffAO2 model has a value of $\eta_p^r = 0.2$. These two names label the same soft effective AO model with different parameter sets.

3.3 BULK PROPERTIES

As already mentioned, all models described above show phase separation in a liquid and a fcc solid phase due to entropic effects. At sufficiently high packing fractions a colloid in a ordered neighbourhood has more local free volume to move as in a disordered state at the same packing fraction. This value is the freezing packing fraction η_f. The onset of melting occurs at the melting packing fraction η_m.

In order to investigate the bulk phase behaviour, we perform simulations in the NpT-ensemble. The volume V is allowed to fluctuate. To obtain both branches of the equation of state pure homogeneous liquid and solid systems were simulated independently by NpT-simulations, where each system contained $N = 4000$ colloids. For the simulations of the liquid systems, volume moves were performed in all spatial directions simultaneously. The directions of the simulation box are allowed to fluctuate independently for systems con-

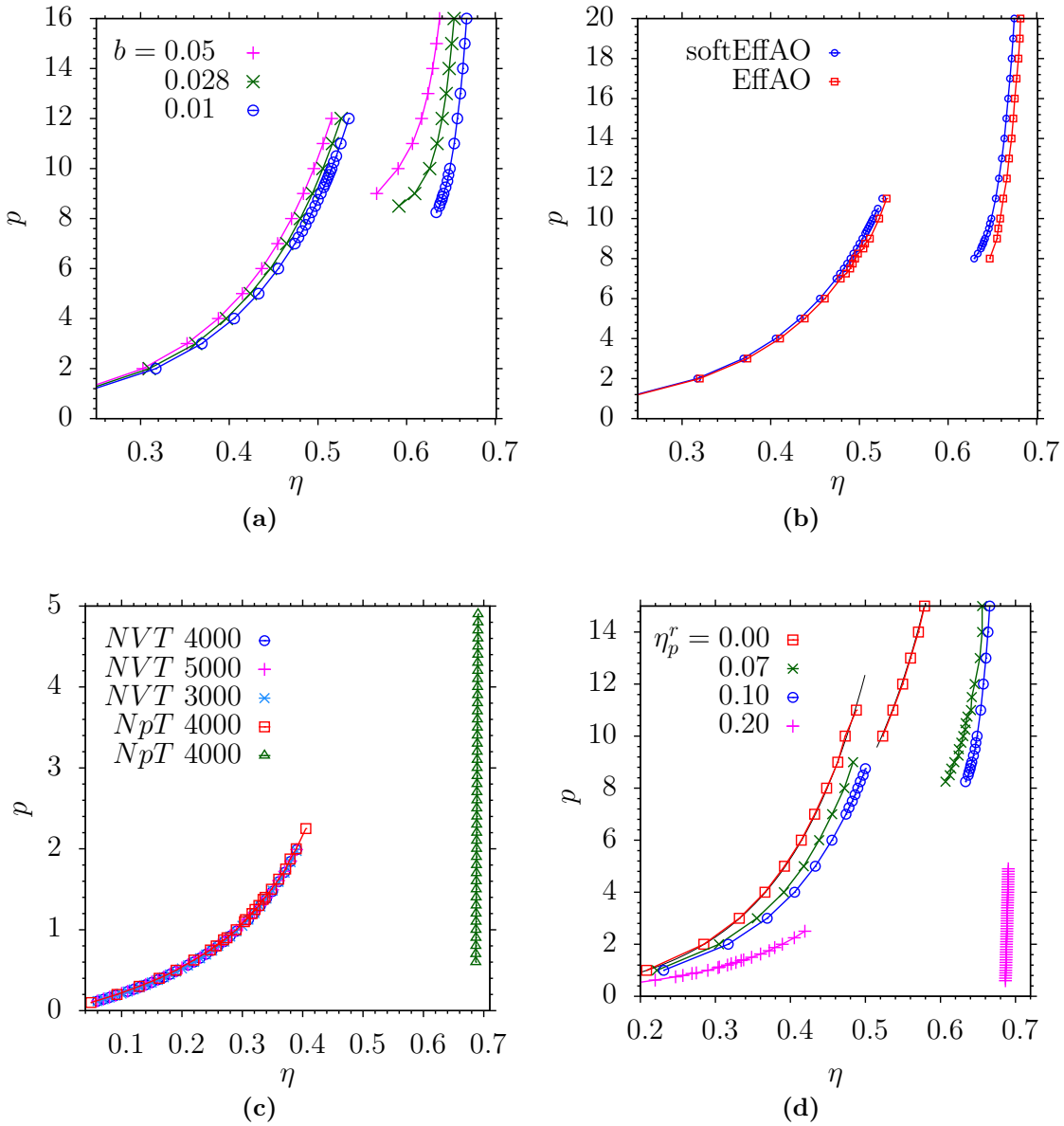

Figure 3.4: **(a)** Pressure p as a function of colloid packing fraction η for the softEffAO1 defined by equation (3.6) with pairs ($b = 0.01$, $e = 0.988571$), ($b = 0.028$, $e = 0.967118$) and ($b = 0.05$, $e = 0.941283$). **(b)** Equation of state for the EffAO and the softEffAO1 model with $b = 0.01$, $e = 0.988571$ and fixed $\eta_p^r = 0.1$. **(c)** Equation of state for the softEffAO2 model with $b = 0.01$ and $e = 0.989200$, determined in different ensembles as indicated. **(d)** Equation of state for the softEffAO model as a function of η_p^r as indicated and fixed $b = 0.01$ and corresponding values for e .

taining solid phases as discussed in section 2.4. The fcc lattice plane (111) was aligned parallel to z-direction of the system and the initial configuration was prepared with periodic boundary conditions, which match the lattice distances of the crystal.

In case of NVT-ensemble simulations, the virial theorem was used to determine a Gaussian distribution of the pressure and calculate the average pressure. The unit for pressure is k_BT/σ^3, which equals to 1 since σ is chosen as unit of length.

The equation of state for the softEffAO model and the EffAO model are calculated for several different sets of parameters and compared, as shown in figure 3.4. For each equation of state, there are two branches visible, the liquid branch η_l for lower values of η, and the crystal fcc branch η_c for higher packing fractions.

Equation (3.6) contains two parameters b and e, which influence the equation of state. For the simulations, b and e need to be fixed. Therefore, the behaviour of the softEffAO model is calculated for several choices and in figure 3.4 (a) a comparison can be seen. The simulations were performed in a NpT-ensemble with $N = 4000$ colloids for each system. The value of $\eta_p^r = 0.1$ was fixed for all models shown in figure 3.4 (a) in order to compare the phase behaviour. Increasing b has the effect of displacing the liquid branch slightly and almost uniformly to lower packing fractions. The change of the solid branch is much more noticeable and it is shifted to lower packing fractions by a much larger extent. Therefore, the width of the liquid-solid coexistence region decreases with increasing parameter b. For studying systems containing both phases in one simulation volume, it is useful to have a larger coexistence region, which corresponds to a wider gap between the branches. Hence, we have chosen $b = 0.01$.

As shown in figure 3.4 (b), the phase behaviour for the softEffAO model with $b = 0.01$ and the EffAO model are very similar and the softness of the potential shifts both branches to slightly lower packing fractions. Both models were investigated in NpT-simulations of $N = 4000$ colloids.

While determining the phase behaviour of the softEffAO model at a polymer reservoir packing fraction of $\eta_p^r = 0.2$ (softEffAO2 model), the implementation of the virial theorem to measure pressure was tested as shown in figure 3.4 (c). Therefore, simulations in the NVT-ensemble of a bulk liquid for three different total numbers of colloids $N = 3000, 4000, 5000$ were performed. In the case of NVT-ensemble simulations, the virial theorem was used to record a Gaussian distribution of the pressure and calculate the average pressure from this. The solid branch was only measured via simulations in the NpT-ensemble. As shown, there are no finite size effects for homogeneous bulk systems at these box volumes and particle numbers, as well as no differences between the two ensembles. Additionally, NpT simulations with $N = 4000$ particles for the liquid are carried out for comparison. Therefore, the system sizes corresponding to 4000 colloids are large enough to determine the bulk phase behaviour.

The equation of state for the softEffAO model for different values of the polymer reservoir packing fraction η_p^r are shown in figure 3.4 (d). In general, both the pressure of the liquid as well as of the solid lowers significantly for increasing values of η_p^r. At the same time, the liquid branch is shifted to lower packing fractions, whereas the solid branch is moved to higher packing fractions as shown in figure 3.4 (d). This illustrates the rapid broadening of the phase coexistence region as shown in figure 3.2. In addition, the solid fcc branch is much steeper for higher values for η_p^r and for the softEffAO2 model all solid pressures have a very similar packing fraction close to $\eta_c \approx 0.7$.

However, all simulations described above are not suitable to obtain a value p_{coex} for the coexistence pressure in thermal equilibrium, since in finite systems the pressure shows a loop analogous to the chemical potential as described in section 2.2. There is an extended region of hysteresis, where either the supersaturated liquid with $p > p_{\text{coex}}$ or the crystal with $p < p_{\text{coex}}$ is stable in the simulation. Hence an accurate estimation of p_{coex} is a non trivial problem. The coexistence pressure is reached only for systems with periodic boundary conditions, containing both liquid and solid with two flat interfaces in between the phases. For these systems, the chemical potentials $\mu_l(p)$ and $\mu_c(p)$ of the two phases are equal. In chapter 5, a method to calculate the coexistence pressure, the so-called INTERFACE VELOCITY METHOD [42] is described, and results for our models are presented.

3.4 STRUCTURAL INVARIANTS

Studying the phase coexistence, we need to be able to distinguish between the particles belonging to one phase or the other phase via an order parameter. Ideally, such an order parameter should local. In our case, we want to investigate the liquid-solid coexistence, and therefore neither the local density nor the number of nearest neighbours are suited to serve as an order parameter as it would be in a vapour-liquid phase coexistence. This is because the distribution of local densities in both phases strongly overlap. We aim to investigate nuclei, which are completely surrounded by liquid and are potentially rotated, since their lattice planes are not fixed due to interactions via periodic boundary conditions. Therefore, the order parameter should not depend on a comparison to an ideal reference lattice.

The object of interest is a cluster of colloids, which consists of a colloid in the center and its nearest neighbours. A possible set of local bond order parameters are the so-called STEINHARDT BOND ORIENTAL ORDER PARAMETERS [43], which are based on spherical harmonics $Y_{lm}(\mathbf{r})$ and are defined as

$$q_l(i) = \sqrt{\frac{4\pi}{2l+1} \sum_{m=-l}^{l} |q_{lm}(i)|^2} \qquad \text{with} \tag{3.8}$$

$$q_{lm}(i) = \frac{1}{N(i)} \sum_{j=1}^{N(i)} Y_{lm}(\mathbf{r}_{ij}) \quad , \tag{3.9}$$

where $N(i)$ is the number of nearest neighbours of colloid i. A colloid j is called nearest neighbour of i, if the length of the distance vector $|\mathbf{r}_{ij}|$ between the two colloids is smaller than a cutoff radius r_{cutoff}. We use a cutoff value of $r_{\text{cutoff}} = 1.3\ \sigma$ for the definition of nearest neighbours as shown in figure 3.5. This value

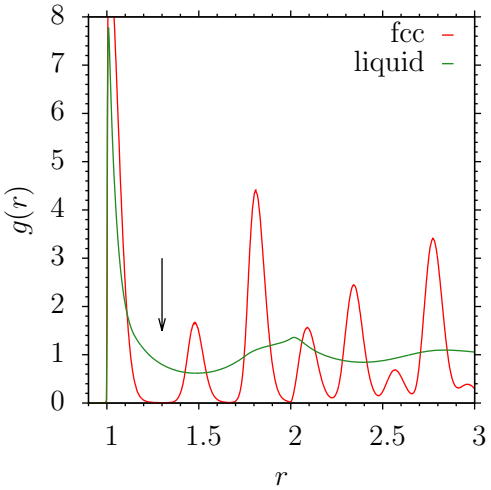

Figure 3.5: Pair correlation functions $g(r)$ measured in a pure fcc phase at packing fraction $\eta = 0.6359$ and a pure liquid phase at $\eta = 0.4964$. The arrow indicates the cutoff $r_{\text{cutoff}} = 1.3\ \sigma$ value for the definition of nearest neighbours.

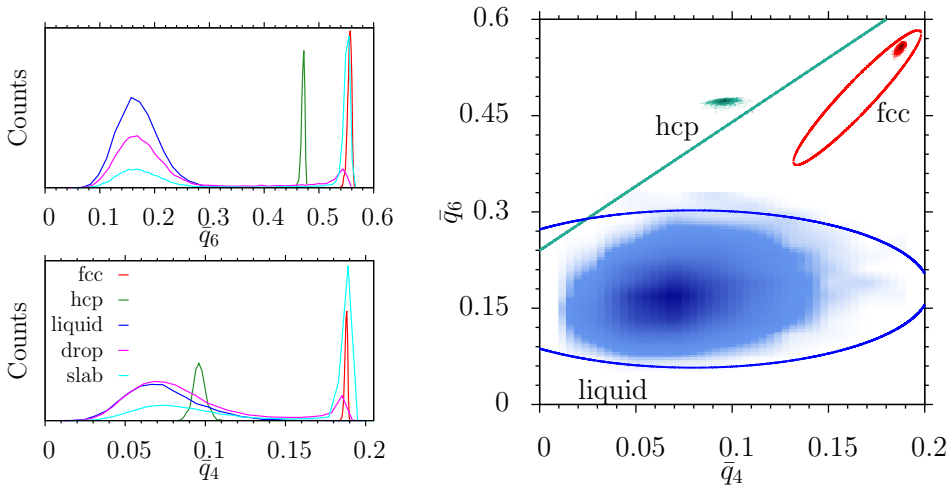

(a) **(b)**

Figure 3.6: **(a)** Histograms for $\bar{q}_4$ (bottom) $\bar{q}_6$ (top) for different configurations as indicated. **(b)** The 2D bond order parameter distributions for pure liquid with $\eta = 0.485$ (blue), fcc (red) and hcp (turquoise) phases are shown with $\eta = 0.65$. Darker values correspond to higher counts. The solid lines indicate the regions for the cutoff values as described in equation (3.12)–(3.14).

was determined by the first minimum of the radial distribution function $g(r)$ measured in a dense liquid phase at $\eta = 0.4964$, which corresponds to an average pressure of $p = 8.5$. The pair correlation function of the crystal bulk phase was measured at a packing fraction of $\eta = 0.6359$, corresponding to the same average pressure value. The second peak in the fcc crystal occurs roughly at $\approx 1.5\ \sigma$ and therefore it is ensured, that the same cutoff value is appropriate in the solid phase.

By averaging the bond order parameters over the nearest neighbours, we can take the second shell of neighbours into account and improve the order parameter further as shown by LECHNER et al. [44]

$$\bar{q}_l(i) = \sqrt{\frac{4\pi}{2l+1} \sum_{m=-l}^{l} |\bar{q}_{lm}(i)|^2} \qquad \text{with} \tag{3.10}$$

$$\bar{q}_{lm}(i) = \frac{1}{N(i)} \sum_{k=0}^{N(i)} q_{lm}(k) \quad . \tag{3.11}$$

Note, that the sum over all nearest neighbours of colloid i includes the colloid itself. Since the spherical harmonics $Y_{lm}(\mathbf{r}) \equiv Y_{lm}(\theta, \varphi)$ only depend on the angles θ and φ between the connecting vectors $\mathbf{r}$ to the nearest neighbours, this set of bond order parameters is independent from a fixed reference lattice.

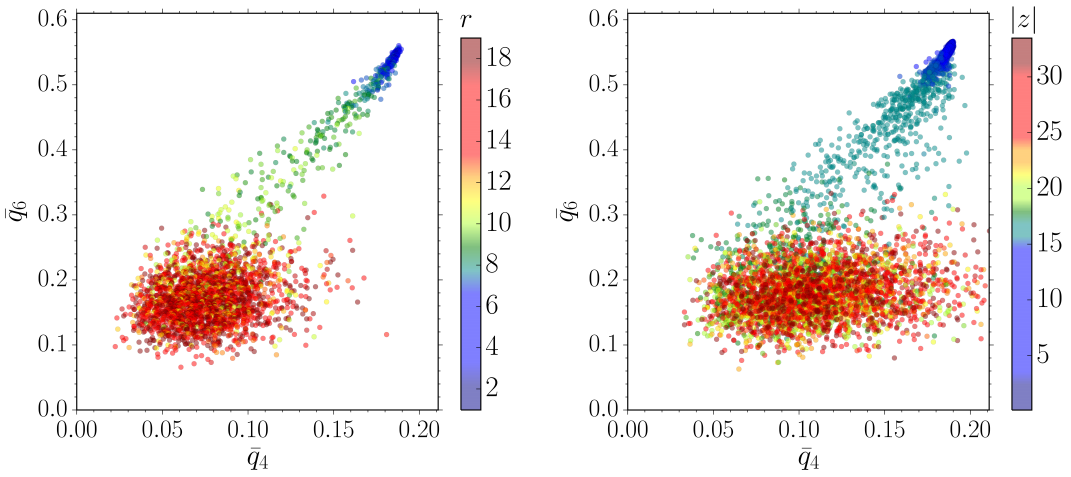

Figure 3.7: (a) The 2D bond order parameter values of each colloid for a system containing a nucleus at the center of mass is shown. The distance r to the center of mass for each point is indicated by the colour. Data for the softEffAO1 model at $\eta = 0.5255$ and $N = 6000$. **(b)** Values for $\bar{q}_4$ and $\bar{q}_6$ of colloids in a slab configuration with $N = 13000$ at $\eta = 0.55$. The absolute value of the z-coordinate is coloured.

For ordered configurations, the components in equation (3.9) are adding up in a coherent manner, depending on their symmetry. The resulting $\bar{q}_l(i)$ has a non zero value that is characteristic for the specific configuration. In contrast to this, the value of $\bar{q}_l(i)$ is closer zero for a disordered phase. The choice of l determines the sensitivity to different crystal structures. We use $l \equiv 4$ and $l \equiv 6$, since $\bar{q}_4(i)$ and $\bar{q}_6(i)$ are sensitive to cubic, hexagonal and other symmetries. Therefore, we are able to distinguish not only liquid-like from solid-like particles, but also fcc from non fcc structures.

In the presence of fluctuations of the colloid positions, a cluster is not characterized by a single set of values for $\bar{q}_4$ and $\bar{q}_6$ but rather by probability density functions as shown in figure 3.6 (a). Here, the distributions of order parameters for simulations of pure bulk phases are shown as well as system containing solid and liquid. Showing the averaged bond order parameters $\bar{q}_4$ and $\bar{q}_6$ in a 2D graph, the different phases separate more clearly as shown in figure 3.6 (b). If fluctuations are not too large, we can clearly distinguish the different phases. Otherwise distributions of $\bar{q}_4$ and $\bar{q}_6$ might overlap. The liquid probability density function is much broader for both $\bar{q}_4$ and $\bar{q}_6$. Nevertheless, as shown in figure 3.6 (b), the different phases are well separated in the $(\bar{q}_4,\bar{q}_6)$-plane. Therefore, the liquid can be clearly distinguished from an ordered solid phases. Due to the combination of $\bar{q}_4$ and $\bar{q}_6$ fcc can be distinguished from a hexagonal close packed (hcp) phase as well.

For distinguishing different phases, the following rules are applied

$$\text{solid fcc:} \qquad \bar{q}_6 < \pm\sqrt{b_0 - (a_0 - \bar{q}_4)^2} + c_0 + e_0\bar{q}_4 \ , \tag{3.12}$$

$$\text{liquid:} \qquad \bar{q}_6 < \pm\sqrt{b_1 - (a_1 - \bar{q}_4)^2} + c_1 \ , \tag{3.13}$$

$$\text{solid hcp:} \qquad \bar{q}_6 > a_2\bar{q}_4 + b_2 \ , \tag{3.14}$$

with constants

$$\text{solid fcc: } a_0 = 0.165, \quad b_0 = 0.0011, c_0 = -0.017 \quad \text{and } e_0 = 3.00 \quad , \tag{3.15}$$

$$\text{liquid: } b_1 = 0.015, c_1 = 0.180 \quad \text{and } a_1 = 0.08 \quad , \tag{3.16}$$

$$\text{solid hcp: } a_2 = 2.000 \quad \text{and } b_2 = 0.24 \quad . \tag{3.17}$$

Values for constants are chosen empirically and are the 2D equivalent to cutoff distances. For the liquid phase this results in an elliptical region where the main axis is parallel to the $\bar{q}_4$ axis. The region defining the fcc is a slanted elliptical. Everything above a straight line is considered to be hcp. The edges of the regions are indicated in figure 3.6 (b) as coloured lines, red for fcc, blue for liquid and turquoise for hcp.

In figure 3.7 (a) values of $\bar{q}_4$ and $\bar{q}_6$ for a configuration containing a solid nucleus surrounded by liquid are shown. The colours of points indicates the averaged distance for each bin of the histogram to the center of mass. The center of mass is located at 0 (dark blue) and the edges of the simulation box ≈ 18 are coloured red. Two broad regions at the $\bar{q}_4$ and $\bar{q}_6$ values for the pure liquid phase and solid phase are shown. In addition, there are particles with intermediate values for $\bar{q}_4$ and $\bar{q}_6$. These particles are clearly belonging to the interface region, since they are coloured green. There is no indication for hcp, which competing with fcc in general. The same picture for a slab configuration with a solid region in the middle at $z = 0$ is shown in figure 3.7 (b). Here, the absolute value of the z-coordinate of each colloid is coloured. Two broad regions for the pure phases and a intermediate region are visible and the particles with intermediate values of $\bar{q}_4$ and $\bar{q}_6$ are again belonging to the interface.

In figure 3.8(a) the phases were distinguished by $\bar{q}_4$ values solely, whereas in figure 3.8(b) $\bar{q}_6$ is used. In figure 3.8(c) a combination of $\bar{q}_4$ and $\bar{q}_6$ according to equation (3.12)-(3.13) is applied. The bulk liquid and solid phases are identified correctly in each case, but the interface particles, which are shown in green, differ. For $\bar{q}_4$ a rather large interface is identified and many particles from the liquid are miscounted as interface particles. This effect is reduced when $\bar{q}_6$ is used instead, since the bulk probability density function for liquid and fcc are more separated using this choice of the bond order parameter. Combining both variables leads to a further improvement and the interface now consists of a few layers of colloids, allowing a clear separation between different phases.

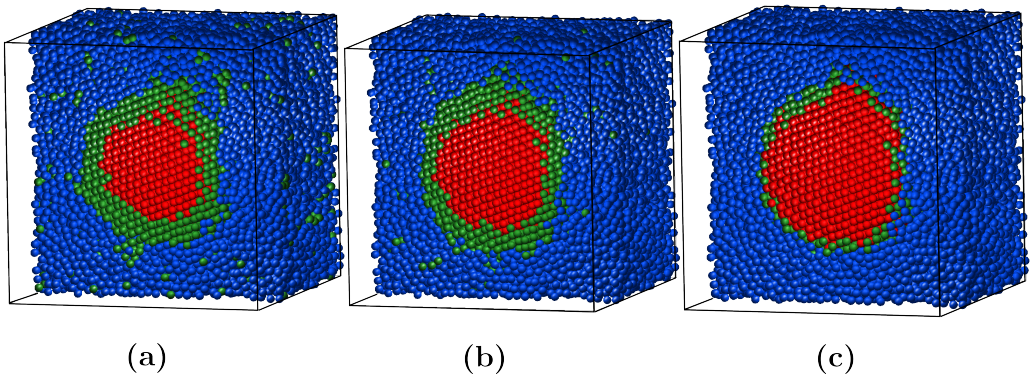

Figure 3.8: Snapshots of a system containing a nucleus, for details on these simulations see section 7.1. The front part is cut out to allow a view inside the nucleus. For all snapshots, the liquid is shown in blue, the solid fcc phase in red and interface particles are coloured green. In **(a)** the colouring criterion is the value of the bond order parameter $\bar{q}_4$. **(b)** The same configuration as in (a) is shown, but coloured according to $\bar{q}_6$. Using both bond order parameter values according to equation (3.12)-(3.14) results in **(c)**.

As shown in section 2.2, phase coexistence between solid and liquid can occur in various geometries and the shape of the interface can differ. We have tested our definition of solid-like and liquid-like colloids, as shown in figure 3.9. In the first column, a representative snapshot of the system is shown. Histograms of both bond order parameters $\bar{q}_4$ (red) and $\bar{q}_6$ (green) as function of either r or z are displayed in the second column. The third column shows 2D probability density functions for the corresponding system. It is clear, that we are able to distinguish the different phases for all shown cases.

A disadvantage of the averaged bond order parameters as defined above, is, that small changes in colloid positions can lead to discontinuous changes in the values for $\bar{q}_4(i)$ and $\bar{q}_6(i)$. Assuming a small change δx in the position of colloid i, the resulting connecting vector $\mathbf{r}_{ij}$ change might be large enough so that the colloid j is not counted as nearest neighbour for i. Hence, the summation changes and the local bond order parameters are not independent from the choice of the neighbourhood criterion and not a continuous function of the colloid positions as shown by Mickel [45]. This behaviour may be even larger than the influence of a relevant physical parameter.

In this thesis, order parameters are solely used to distinguish between liquid and solid phases in systems containing both phases at a certain total packing fraction η. The absolute value of $\bar{q}_4(i)$ and $\bar{q}_6(i)$ change with the packing fraction η, as shown in figure 3.10. To investigate whether this change is influencing the ability to distinguish liquid from solid colloids, a slab geometry in a elongated box $L \times L \times 5L$ with $L \approx 13.39$ was studied. The volume was filled half by a liquid and half by a solid. The average bond order parameter value in a NVT-ensemble simulation for each phase was determined separately

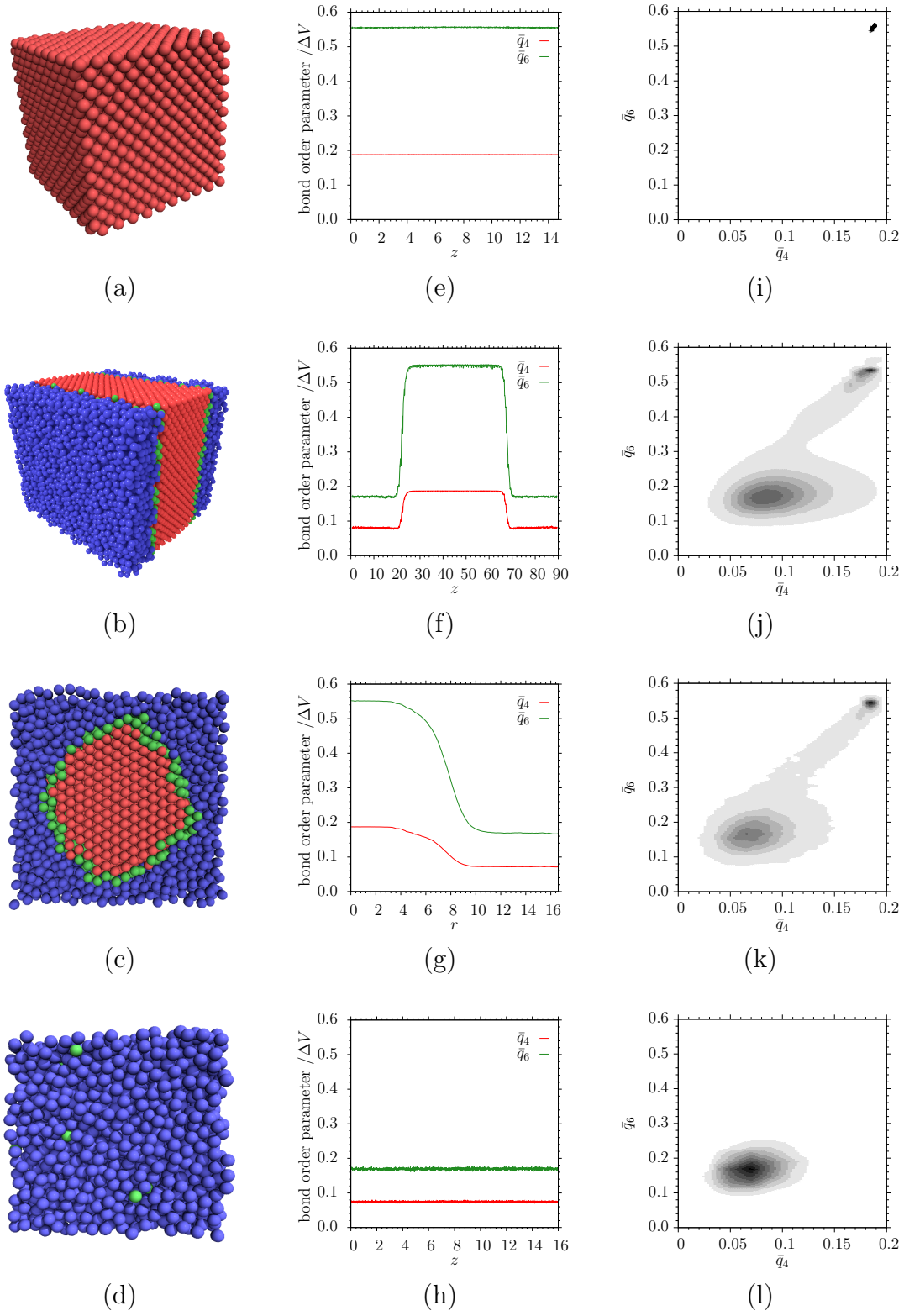

Figure 3.9: (a)-(d) Typical configurations for the systems, liquid-like colloids are shown in blue, solid-like colloids in red and interface colloids in green. **(e)-(h)** Spatial bond order histograms as a function of radius r (droplet) or z (pure phases and slab). **(i)-(l)** Distribution in the ($\bar{q}_4$-$\bar{q}_6$)-plane, dark areas denote high counts and light areas low counts.

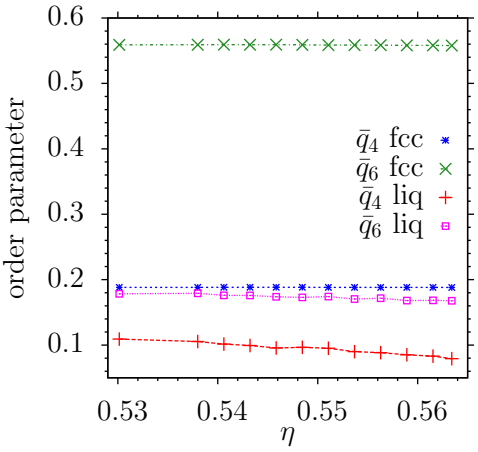

Figure 3.10: The averaged bond order parameters in a liquid and in a solid phase as a function of total packing fraction η. The total number of particles was between 12160 and 12923, depending on η. A clear dependency of $\bar{q}_4$ and $\bar{q}_6$ on the packing fraction is only visible for the liquid.

for each part of the system. We focussed on regions which contain the bulk phases and not the interface. The box size ensures large enough bulk like regions. Particularly the averaged values for the liquid phases change with the packing fraction η. However, the liquid value $\bar{q}_{4,\mathrm{liq}} \approx 0.1$ and the corresponding solid value $\bar{q}_{4,\mathrm{fcc}} \approx 0.19$ are sufficiently separated. The same applies for $\bar{q}_6$ with $\bar{q}_{6,\mathrm{liq}} \approx 0.18$ and $q_{6,\mathrm{fcc}} \approx 0.56$. Since we are solely interested in distinguishing solid-like colloids from liquid-like colloids and the analysis of absolute values or trends of the bond order parameters are not relevant here.

4 CLASSICAL NUCLEATION THEORY

Depending on conditions, a system can undergo phase transitions between different thermodynamically stable phases, for example from liquid to solid. Due to spontaneous thermal fluctuations in the liquid, the density exceeds the liquid density at fluid-solid coexistence and thereby nanoscopic nuclei of the solid are formed.

This formation process is called nucleation. In the next chapter the basic concepts connected to nucleation theory and their limitations are presented. In general one needs to distinguish HOMOGENEOUS and HETEROGENEOUS nucleation, where heterogeneous nucleation is a much more common phenomenon. Heterogeneous nucleation occurs at surfaces and seeds, whereas homogeneous nucleation occurs by spontaneous fluctuations in the bulk [1, 2, 4]. In this thesis we are only considering homogeneous nucleation.

Nucleation can be seen as a first order phase transition, connected to a discontinuous derivative of the free energy. Since nucleation events are based on spontaneous thermal fluctuations, they are rare and therefore difficult to observe directly either in experiment or in simulation. The free energy barrier needs to be overcome in each event of nucleation due to the surface excess free energy cost caused by the crystal-fluid interface [4]. This energy barrier is typically on the order of 10 k_BT [10, 12] and the nuclei contain a few hundred particles. This results in extremely small and strongly fluctuating nuclei, for which the classical way of describing the nucleation as a competition between bulk and surface free energies [1, 2, 4, 46] fails [10, 47]. Furthermore, the local identification of nuclei is difficult, since interfaces are broad and fluctuating objects [48, 49].

Experimental tests were performed for the nucleation of droplets from supersaturated vapour [50–52] as well as for the formation of crystal nuclei [53–60]. In experiments nucleation rates are often determined indirectly by observing the growth of the solid [1, 4, 5, 61, 46, 62–68]. This procedure necessarily involves assumptions. The detailed properties of the nuclei that are formed are non-universal and depend upon the particular system.

Classical Nucleation Theory (CNT) is a very simple and elegant way of describing nucleation in general. For this approach, the basic assumption is, that macroscopic properties of the system can be applied to describe microscopic droplets. It is not known to which extend this assumption is reliable and it is not completely understood on a quantitative level.

The free energy of a droplet, containing the new thermodynamically stable phase, is given by two main contributions, the energy gain due to the formation of the new phase and the energy loss caused by the interface between the two phases, as shown in figure 4.1. The energy gain is proportional to the volume

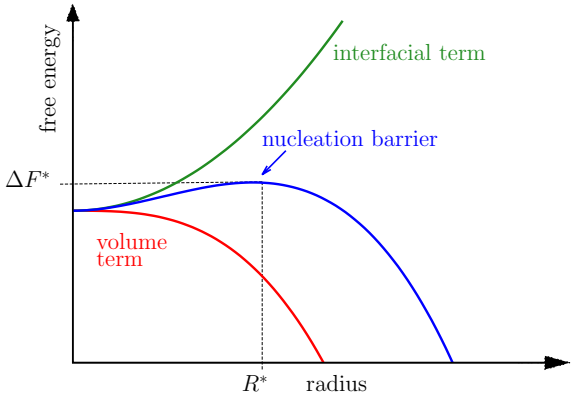

Figure 4.1: Contributions to the classical nucleation theory. The volume term is proportional to r^3 (red), and the interfacial term is proportional to r^2 (green). The blue curve is the resulting total free energy as a function of droplet radius. The height ΔF^* of the total free energy at the critical radius R^* is the nucleation barrier.

of the droplet, hence r^3. The energy costs are proportional to the formed interface area, and therefore scale with r^2. The combination of both forms the total free energy and has an maximum at the critical radius R^*, the so-called NUCLEATION BARRIER.

In the classical nucleation theory [4], the free energy of a (crystal) nucleus formation can be written as combination of volume and surface term as

$$\Delta F = -(p_\mathrm{c} - p_\mathrm{f})V + F_\mathrm{surf}(V) \quad . \tag{4.1}$$

Here p_c is the pressure in the crystal nucleus and p_f in the (metastable) fluid phase surrounding it. For crystals the term $F_\mathrm{surf}(V)$ is given by a complicated integral,

$$F_\mathrm{surf}(V) = V^{2/3} \int_{A_w} \gamma(\mathbf{n}) d\mathbf{s} \equiv A_w \bar{\gamma} V^{2/3} \quad . \tag{4.2}$$

The crystal-fluid interface tension $\gamma(\mathbf{n})$ depends on the orientation of the interface normal vector $\mathbf{n}$ relative to the crystal lattice axes [69, 64]. A_w is the surface area of a unit volume, whose shape is derivable from $\gamma(\mathbf{n})$ via the Wulff construction, as described in section 4.2. The average interface tension $\bar{\gamma}$ is defined as

$$\bar{\gamma} = A_w^{-1} \int \gamma(\mathbf{n}) d\mathbf{s} \quad , \tag{4.3}$$

which can be considered to be independent of the cluster size, if one assumes large enough nucleus volumes for which $F_\mathrm{surf}(V) \propto V^{2/3}$ already holds. Note that this proportionality may fail for small V due to curvature corrections. In the thermodynamic limit, the configuration with one nucleus on top of the free energy barrier is a saddle point in configuration space. The condition for an (unstable) equilibrium is given by

$$\frac{\partial \Delta F}{\partial V} = 0 \rightarrow -(p_\mathrm{c} - p_\mathrm{f}) + \frac{\partial F_\mathrm{surf}}{\partial V} = 0 \quad , \tag{4.4}$$

which results in the critical nucleus volume V^* and barrier ΔF^* by

$$p_\mathrm{c} - p_\mathrm{f} = \frac{2A_w\bar{\gamma}}{3}V^{*-1/3} \tag{4.5}$$

$$\rightarrow V^* = \left(\frac{2A_w\bar{\gamma}}{3\delta p}\right)^3 \tag{4.6}$$

$$\rightarrow \Delta F^* = \frac{1}{3}A_w\bar{\gamma}V^{*2/3} = \frac{1}{2}(p_\mathrm{c} - p_\mathrm{f})V^* \quad . \tag{4.7}$$

Even if V^* is large enough, so that corrections to equation (4.1) can be neglected, equation (4.7) is difficult to apply due to the lack of knowledge on A_w and $\bar{\gamma}$. The pressure difference, $\delta p = p_\mathrm{c} - p_\mathrm{f}$, is called LAPLACE PRESSURE.

The chemical potential in the fluid $\mu_\mathrm{f}(p_\mathrm{f})$ is equal to value inside crystal nucleus $\mu_\mathrm{c}(p_\mathrm{c})$, since they are in equilibrium. Knowing that $\mu_\mathrm{c}(p_\mathrm{coex}) = \mu_\mathrm{f}(p_\mathrm{coex}) = \mu_\mathrm{coex}$, we can use the expansions equation (2.33) and (2.34) around coexistence

$$\mu_\mathrm{c}(p_\mathrm{c}) \approx \mu_\mathrm{coex} + v_\mathrm{m}(p_\mathrm{c} - p_\mathrm{coex}) \ , \tag{4.8}$$

$$\mu_\mathrm{f}(p_\mathrm{f}) \approx \mu_\mathrm{coex} + v_\mathrm{f}(p_\mathrm{f} - p_\mathrm{coex}) \ , \tag{4.9}$$

as described in section 2.3. Combining both expansions we conclude that

$$(p_\mathrm{c} - p_\mathrm{coex})\eta_\mathrm{f} = (p_\mathrm{f} - p_\mathrm{coex})\eta_\mathrm{m} \quad . \tag{4.10}$$

Therefore, the pressure p_c in the crystal is given by

$$p_\mathrm{c} = \frac{\eta_\mathrm{m}}{\eta_\mathrm{f}}(p_\mathrm{f} - p_\mathrm{coex}) + p_\mathrm{coex} \quad . \tag{4.11}$$

Combining equation (4.5) and (4.11) yields to

$$\delta p_\mathrm{f} = p_\mathrm{f} - p_\mathrm{coex} = v_\mathrm{f}(\mu_\mathrm{f} - \mu_\mathrm{coex}) = \frac{2}{3}A_w\bar{\gamma}V^{*-1/3}\frac{1}{\frac{\eta_\mathrm{m}}{\eta_\mathrm{f}} - 1} \quad . \tag{4.12}$$

This result provides a test of CNT in Monte Carlo simulations, since it relates the measurable pressure difference or chemical potential to the interfacial tension, the critical nucleus volume and packing fractions. These values can be obtained directly in simulations. The only unknown is the crystal shape, which is determining A_w. It is important to note, however, that one needs to check that nonlinear corrections to equations (4.8) and (4.9) are actually still completely negligible. If they are not negligible, one can still obtain $p_\mathrm{c} - p_\mathrm{f}$, knowing that $\mu_\mathrm{c}(p_\mathrm{c}) = \mu_\mathrm{f}(p_\mathrm{f}) \equiv \mu$, and integrating the equation of state (crystal branch) from μ_coex to μ.

4.1 SPHERICAL DROPLET

A very common assumption for classical nucleation theory is that the average shape of the nuclei is spherical. For example, the nucleus of a liquid from supersaturated vapour is clearly shaped as a sphere. The interface excess free energy is isotropic, hence $\gamma(\mathbf{n}) \equiv \gamma$. The surface area per unit volume for a sphere of radius R is given by

$$V = \frac{4}{3}\pi R^3 \text{ and} \tag{4.13}$$

$$A_w = (36\pi)^{1/3} \tag{4.14}$$

and the surface excess free energy for a spherical nucleus results in

$$F_{\text{surf}} = \gamma 4\pi R^2 \quad . \tag{4.15}$$

Combining this result with equation (4.12) yields to [19]

$$p_{\text{f}} - p_{\text{coex}} = \frac{2\gamma}{R^*} \frac{\eta_{\text{f}}}{\eta_{\text{c}} - n_{\text{f}}} \quad , \tag{4.16}$$

and equation (4.1) and (4.6) simplify to

$$\Delta F = -\frac{4}{3}\pi R^3 \delta p + 4\pi R^2 \gamma \quad , \tag{4.17}$$

$$\text{and} \qquad R^* = \frac{2\gamma}{\delta p} \quad . \tag{4.18}$$

These equations can be used to compare results from computer simulations of nuclei without assumptions for the shape in classical nucleation theory with spherical nuclei.

4.2 WULFF CONSTRUCTION

In this thesis we consider crystal droplets in the liquid. As shown in section 2.2, a crystal has a long range ordering, and is therefore anisotropic. Hence, different spatial directions can have different interfacial tensions. The interfacial excess free energy per unit area $\gamma(\mathbf{n})$ depends on the orientation of the unit vector along the interface normal $\mathbf{n}$ relative to a lattice direction. The surface free energy ΔF_{surf} of an arbitrary shaped cluster is an integral of the form given by equation (4.3). The dependence determines the shape of the nucleus in equilibrium, since the crystal in liquid tries to minimize its energy. Assuming

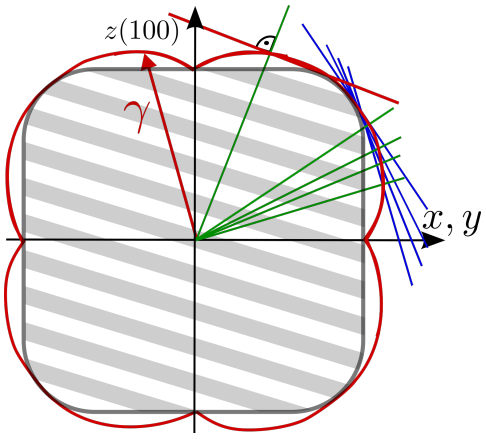

Figure 4.2: 2D example of the Wulff construction, where the interfacial tension for (100) and (010) is lower than for the normals in between. The function $\gamma(\mathbf{n})$ is shown in red. The blue lines indicate the tangents, perpendicular to the normal vectors shown in green. The inner envelope results in a rectangular shape with rounded corners, shaded in grey.

a finite number of surface elements, the integral is given by the sum of the area of the surface parts A_i times the interfacial tension γ_i of the corresponding face,

$$\sum_i \gamma_i \cdot A_i \quad . \tag{4.19}$$

The so-called WULFF CONSTRUCTION [70–75] provides a way to construct the shape with the smallest free energy ΔG of the surface, while the volume remains constant. In order to calculate this shape, one needs the interfacial excess free energy $\gamma(\mathbf{n})$ for each choice of $\mathbf{n}$. A polar plot of $\gamma(\mathbf{n})$ is sketched in figure 4.2. For each point in the polar plot a tangent line is constructed, where the distance to the origin is given by the value of $\gamma(\mathbf{n})$ at this point. This takes into account, that the surface energy of a crystal face is proportional to its surface energy. The tangent line is perpendicular to the surface normal $\mathbf{n}$. The crystal shape without thermal fluctuations is then given by the inner envelope of all these tangent lines. In 3 dimensions the tangent lines are planes and the shape of the crystal is given by the inner volume of all these planes. If the interfacial excess free energy is given by a constant $\gamma(\mathbf{n}) = \gamma_0$ for all choices of $\mathbf{n}$, the inner envelope of the tangent planes is a sphere with radius γ_0.

This construction can be considered as a graphical way of performing a Legendre transformation between the free energy surface of the crystal and the shape of the crystal. It is not straightforward to carry out this construction in practice, since in general $\gamma(\mathbf{n})$ is not known for all choices of $\mathbf{n}$.

If one assumes that $\gamma(\mathbf{n})$ has only three components in the (111), (100), and (110) orientation and ignores all other crystal faces, it is possible to calculate 3D shapes for this approximate case. Each orientation is represented by a set of planes, where the distance to the origin is given by the value of the interfacial tension in this direction. The plane intersections are calculated and the inner hull yields to the crystal shape as shown for some examples in figure 4.3. These shapes are approximations since fluctuations are ignored and no possible other orientations are taken into account.

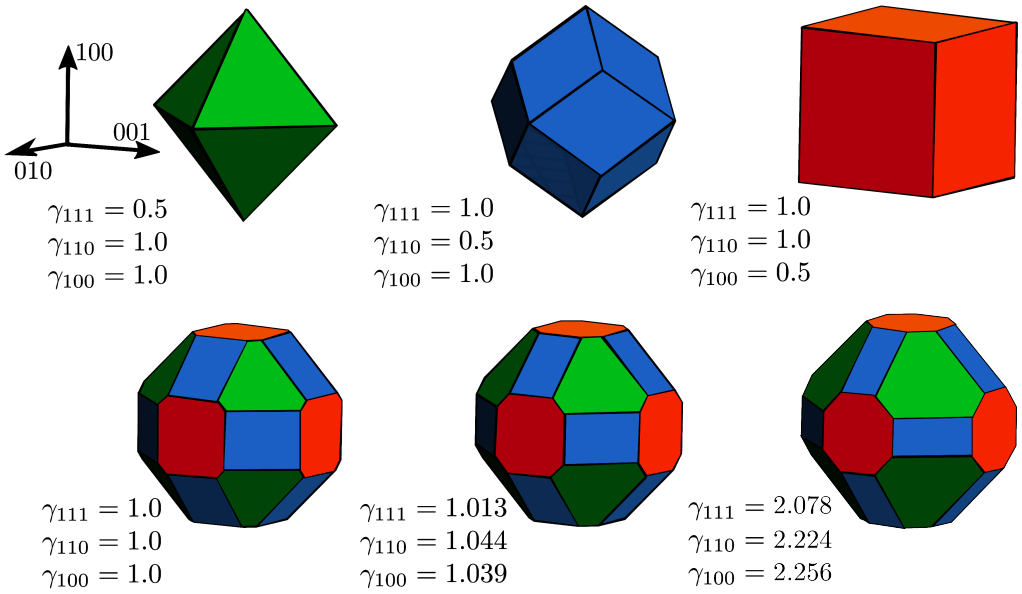

Figure 4.3: 3D Wulff shapes of a fcc nucleus assuming only values for the three interfacial tensions in the (111), (100), (110) orientation and ignoring all other crystal faces. Top row shows shapes consisting of only one interface type (octahedron, rhombic dodecahedron and cube) and bottom row shows shapes with all three faces. Created with reference [76].

4.3 INTERFACIAL TENSION

A crucial ingredient in the investigation of the free energy barriers for homogeneous nucleation is the interfacial tension γ, since it appears in equation (4.2) and consequently in (4.7). As shown by BINDER in reference [77], the interfacial tension γ can be calculated in finite systems by

$$\gamma = \lim_{L\to\infty} \frac{\Delta F}{2L^2} \tag{4.20}$$

where $2L^2$ is the total area of the interfaces and ΔF is the free energy cost of the formation of two interfaces. Due to periodic boundary conditions there are always two interfaces, as sketched in figure 4.4(b). In practice, elongated simulation boxes with $L \times L \times n \cdot L$ where n is at least 2, are used to avoid interactions between the two interfaces via periodic boundaries. This geometry requires that the interfaces are always perpendicular to the z-direction, which is the long direction of the elongated box. For $n = 1$ the interfaces could also orient perpendicular to the x-direction or the y-direction. This additional degree of freedom would complicate the analysis of the simulations. Since the interfacial tension between a crystal and a fluid depends on which face of the

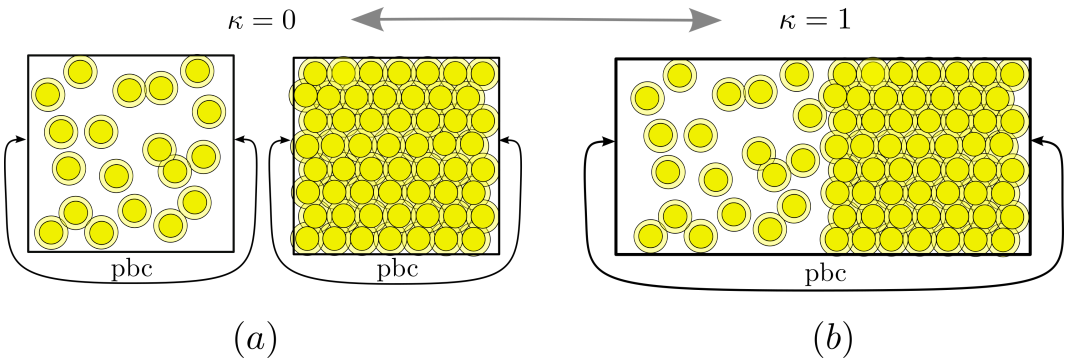

Figure 4.4: (a) Sketch of the initial state S_0 for the ensemble switch method, corresponding to $\kappa = 0$. Two separate boxes with periodic boundary conditions are shown. The first box is filled with liquid, the second with solid. **(b)** Final state S_1 for $\kappa = 1$. Both boxes are connected via periodic boundary conditions and two interfaces between the phases are formed. Adapted from [78].

crystal is exposed to the liquid, the interfacial tension has to be calculated for each orientation separately.

To determine the interface tension in Monte Carlo Simulations we use the so-called ENSEMBLE SWITCH METHOD [79, 80]. For the softEffAO1 model, results are obtained by SCHMITZ et al. [47, 78]. The free energy is difficult to obtain in computer simulations, since it depends on the accessible phase space of the system. To calculate the interfacial tension, the free energy difference ΔF is needed. ΔF is calculated between a initial state S_0 without any interfaces and a final state S_1 with interfaces at equilibrium between the phases. The state S_0 corresponds to two separate, non interacting boxes with $L_x = L_y = L$ and $L_z/2$ with the Hamiltonian $\mathcal{H}_0$. The first box is filled with liquid at a packing fraction η_f and pressure p_coex. The second box contains a solid at η_m and the same pressure p_coex. The second state S_1 has the volume of $L_x = L_y = L$ and L_z with the Hamiltonian $\mathcal{H}_1$. Here we have assumed, for simplicity, that the crystal structure is compatible with a square cross section perpendicular to the z-direction. In general this is not the case, and one needs to choose $L_x \neq L_y$, such that a unstrained crystal results. Both phases are in contact and equilibrium, which form two planar interfaces of size L^2 perpendicular to L_z, as shown in figure 4.4. The mixing between the two ensembles can be realized by a superposition of both Hamiltonians

$$\mathcal{H}(\kappa) = (1-\kappa)\mathcal{H}_0 + \kappa\mathcal{H}_1 \quad , \tag{4.21}$$

where $\kappa \in [0,1]$ indicates the current mixing percentage between both ensembles. In addition to the canonical moves, a new move is introduced, in which the value of κ is tried to be changed. For this purpose, all values of κ are divided into a finite number M of discrete values $\{\kappa_k\}$. The system is allowed to move from κ_i to κ_{i-1} or κ_{i+1} by a Metropolis step as described in section 2.1.1. A set of overlapping windows $\{[\kappa_0, \kappa_1], [\kappa_1, \kappa_2], \ldots, [\kappa_{M-1}, \kappa_M]\}$

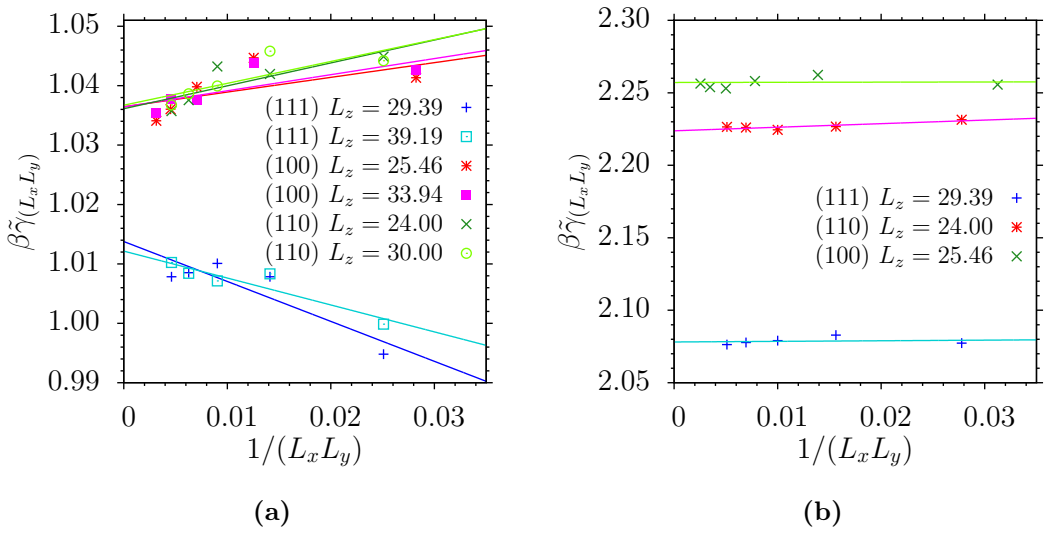

Figure 4.5: (a) Finite size scaling for the reduced interfacial tension of the softEffAO1 model as a function of the inverse interfacial area. The box dimension in z-direction is fixed. Data taken from reference [78]. **(b)** Same graph as in (a) for the softEffAO2 model.

is prepared and then Successive Umbrella Sampling can be used. For details of this method refer to [81]. A big advantage of using successive umbrella sampling is that detailed balance is fulfilled automatically. In addition, the windows can be simulated in parallel using this sampling technique. Using the resulting free energy $\beta F(\kappa)$ as a function of κ, we obtain

$$\beta\Delta F = \beta\left[F(0) - F(1)\right] \quad . \tag{4.22}$$

Note that the intermediate states with $0 < \kappa < 1$ have no physical meaning. Only the free energy at $\kappa = 0$ and at $\kappa = 1$ can be interpreted as physical appropriate states. Hence, the exact behaviour as a function of κ is not important as long as the beginning and the end are unchanged.

Finite size effects can be treated by this method, for details refer to the chapters 5 and 6 of the dissertation of Schmitz [78]. Summarizing the main result, the finite size scaling of the interfacial tension in 3 dimensions with the box size $V = L_x \times L_y \times L_z$ can be written as

$$\beta\gamma(L_x, L_y, L_z) = \beta\gamma_\infty - x_\perp \frac{\ln L_z}{L_xL_y} + x_\parallel \frac{\ln L_x}{L_xL_y} + \frac{C}{L_xL_y} \quad . \tag{4.23}$$

$x_\parallel$ and $x_\perp$ are two universal constants and C is a system dependent constant. For our models used in this work, they are given by $x_\parallel = 3/4$ and $x_\perp = 1/2$. One can define a reduced interfacial tension as

$$\beta\tilde{\gamma}(L_x, L_y, L_z) = \beta\gamma(L_x, L_y, L_z) + \frac{x_\perp \ln L_z - x_\parallel \ln L_x}{L_x L_y} \tag{4.24}$$

$$= \beta\gamma(L_x, L_y, L_z) + \frac{C}{L_x L_y} \quad . \tag{4.25}$$

Using a scaling of $\beta\tilde{\gamma}(L_x, L_y, L_z) \propto 1/(L_x L_y)$, the interfacial tensions of the softEffAO1 model can estimated as shown in figure 4.5 (a).

The values for the softEffAO1 model are taken from reference [78] while the values for the softEffAO2 model are obtained in the present work. The (110) and (100) orientation are almost identical and the (111) orientation is slightly favoured. Resulting values for $\beta\gamma_\infty$ can be found in table 4.1. For the softEffAO2 model, the calculated values are roughly twice as large and the anisotropy is more pronounced, as shown in figure 4.5 (b). Each system size was calculated in parallel using 1 CPU core per κ value.

Table 4.1: The interfacial tensions for the (111), (110) and (100) direction in units of $k_B T/\sigma^2$ for the softEffAO1 and softEffAO2 model

ORIENTATION	SOFTEFFAO1	SOFTEFFAO2
fcc (111)	1.013	2.078
fcc (110)	1.044	2.224
fcc (100)	1.039	2.256

5 COEXISTENCE PRESSURE

A very precise estimation of the coexistence pressure p_{coex} is needed to calculate the Laplace pressure δp in equation (4.12). The freezing η_{f} packing fraction and melting packing fraction η_{m} are required for calculating a prediction for CNT. In addition, these values are needed to stabilize a system containing a solid nucleus surrounded by a liquid.

The value for the coexistence cannot be read off from the equation of state, since there is a hysteresis in the bulk branches as in section 3.3 described. Both pure bulk phases extend substantially into the two phase coexistence region. In the following, the so-called INTERFACE VELOCITY METHOD, as proposed by ZYKOVA-TIMAN et al. in [42] is used to determine the coexistence pressure p_{coex}.

The interface velocity method relies on observing the growth or melting of a crystal slab in liquid. A typical configuration is shown in figure 5.1. The crystal slab is oriented such that it has (100) interfaces with the liquid. In this particular case one can choose $L_x = L_y \equiv L$ for the simulation volume with periodic boundary conditions. We perform Monte Carlo simulations of the inhomogeneous configurations in the isothermal-isobaric NpT-ensemble or the Np_zT-ensemble. The temperature T and the particle number N are fixed and the pressure p is kept constant, while the volume or the z-direction can fluctuate. The coexistence pressure of the softEffAO1 model is determined in the NpT-ensemble and for the softEffAO2 model the Np_zT-ensemble was used. If the lattice constants for the crystal are known precisely, the fluctuations in x- and y-directions can be suppressed and less statistics is needed. In the following, all given values for pressures are in units of k_BT/σ^3.

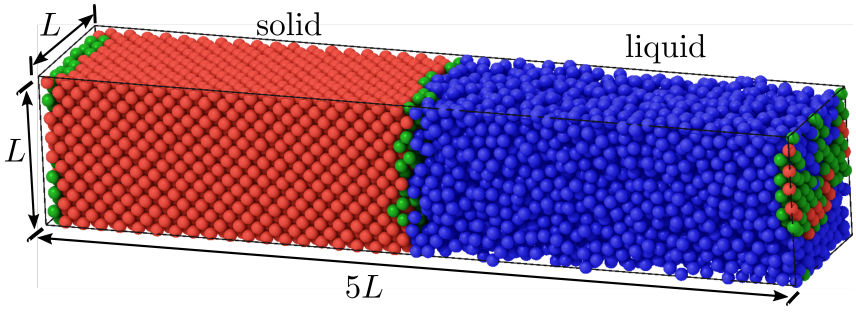

Figure 5.1: Snapshot of a configuration for the EffAO model. The system size is $V = L \times L \times L_z$ with $L_z = 5L$ and $L = 11.8512$. Periodic boundary conditions are implied. The crystal fcc slab is shown on the left side and the liquid on the right side, separated by two interfaces. Here $n = 8$ and $N = 9250$ were chosen with an appropriate size for $p = 7.875$. Colloids belonging to the liquid are shown in blue, particles belonging to the crystal are shown in red colour, while particles in the center of the interface are displayed in green.

The coexistence pressure is obtained by investigating an inhomogeneous system containing both liquid and solid. We record the volume of the system to monitor the growth or melting of the crystal phase. If the system is in equilibrium, both phases are stable and the total volume is neither growing nor shrinking. We apply the following algorithm to determine the coexistence pressure, utilizing the criterion of coexistence.

1. Perform bulk fcc phase simulations in the NpT-ensemble to determine the lattice distance at one fixed pressure value p_0
2. Prepare an inhomogeneous system of size $L \times L \times 5L$, compatible to the lattice distance at p_0, filled half with a liquid and half with a solid at a suitable total packing fraction in the middle of the two phase coexistence region.
3. Perform an equilibration run in the NVT-ensemble.
4. Switch to NpT or Np_zT-ensemble, choosing p_0 as pressure. Record the volume change ΔV as a function of MC cycles during the run.
5. Repeat from 1. for a different value of p_0 until the steady-state pressure value p_{coex} is found, where $\Delta V \equiv 0$.

Hence, we need to prepare systems containing a crystal fcc phase surrounded by a fluid phase, as shown in figure 5.1. The phases are separated by two planar interfaces due to periodic boundary conditions in all spatial directions. The volume is set up to be $L \times L \times 5L$ to avoid interactions between the two interfaces, as described in [42]. The (100) plane of the fcc lattice is aligned perpendicular to the z-direction for all simulations. To prepare such an inhomogeneous system, we need the corresponding packing fractions of the bulk phases $\eta_{\text{f}}(p)$ and $\eta_{\text{m}}(p)$. The values for a given pressure can be determined from the two branches in the equation of state. They are gained separately by MC Simulations in the NpT-ensemble of the pure phases as described in section 3.3. The lattice constant d for the crystal at pressure p is required, since the box length $L = n \cdot d$ in x- and y-direction has to match the lattice distance precisely at the given pressure to ensure that the inhomogeneous system is prepared without artificial strains in the crystalline region. Note, that the lattice constant d changes as a function of the pressure p, but can be determined easily during the simulation of the solid bulk phase.

After initialisation of the inhomogeneous systems simulations in the canonical ensemble with no volume moves are performed. These simulations are equilibrating the bulk phases and the two interfaces at a fixed value for the pressure p. We perform roughly 10^7 particle displacement moves per particle, depending on the system size to ensure a well equilibrated starting configuration. The

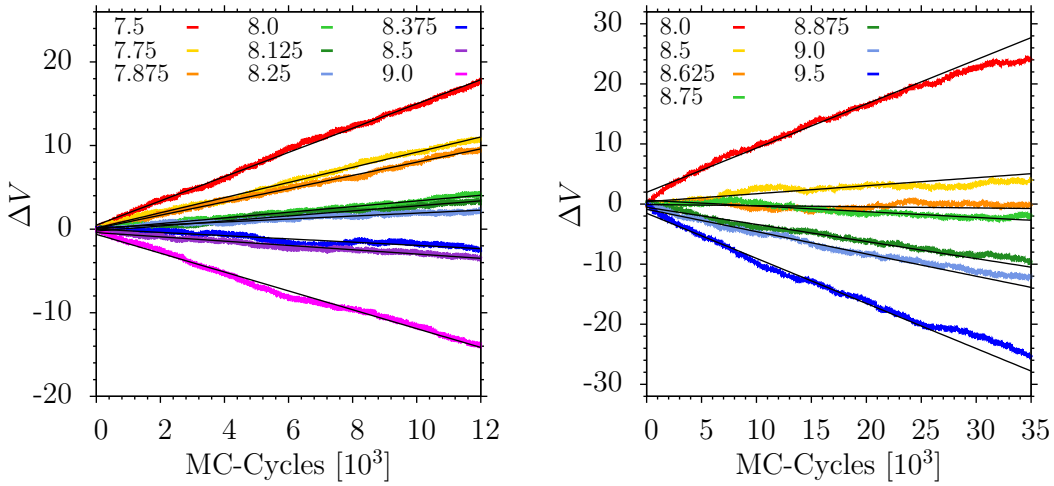

Figure 5.2: Volume change ΔV as a function of MC cycles for different pressures as indicated, for **(a)** the EffAO model and **(b)** the softEffAO1 model. The system contains 9250 colloids in each case, corresponding to $n = 8$ lattice planes in x- and y-direction. The solid lines are fits from which $\langle dV/dt \rangle$ is determined. Each curve is averaged over 100 independent runs.

relative volume fraction of the phases can change during this simulation and the packing fractions of both phases can adjust slightly, if the initial choices for $\eta_{\mathrm{f}}(p)$ and $\eta_{\mathrm{m}}(p)$ are not adequately chosen. The lattice constant in x- and y-direction, however, is fixed and cannot change.

To determine the coexistence pressure of the EffAO and the softEffAO1 model, the volume of the simulation box was allowed to fluctuate independent in each lateral dimension after equilibration. Note that the fluctuations in x- and y-directions are rather small, since the number n of fcc lattice planes in these directions cannot change in volume moves. The volume changes in the x- and y-directions ensure that the crystal is not artificially constrained. Because of these fluctuations we needed roughly ten times more statistics in comparison to [42], where the x- and y-directions are kept fixed. The simulations in the NpT-ensemble are short with around $30 \cdot 10^3$ MC cycles. N canonical MC moves with acceptance probabilities between 0.7 and 0.8 and one volume move with acceptance probabilities between roughly 0.3 and 0.5 in each step were performed. The volume change ΔV during the simulation run of the system is studied as a function of MC cycles as shown in figure 5.2. These simulations were performed for pressures between $p = 8.0$ and 9.5 for the softEffAO1 model and for $p = 7.5$ and 9.5 pressures for the EffAO model. All values can be found in figure 5.2, which shows that ΔV increases with time for low pressures and decreases for high pressures. This behaviour is expected, since the crystalline part of the system is melting for pressure values below p_{coex} and the liquid

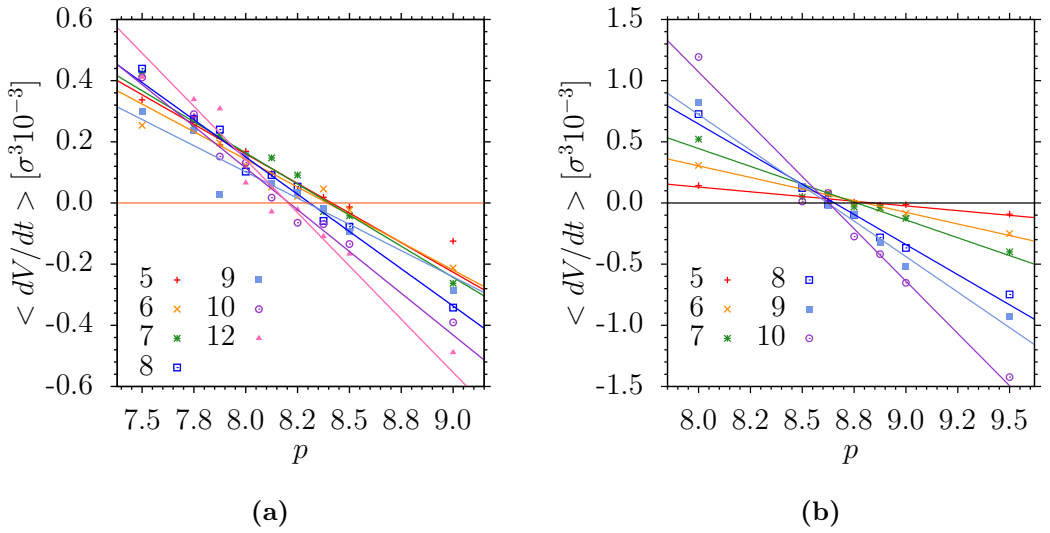

Figure 5.3: Fit values from figure 5.2 for the volume velocities $\langle dV/dt \rangle$ for the different system sizes, as indicated. Results for **(a)** the EffAO model and **(b)** the softEffAO1 model. The zero crossing point for each system size is determined.

requires more volume. The opposite behaviour is observed for high pressures, since the crystal is growing and reduces the overall volume. Clearly, these data in figure 5.2 (a) and (b) still are affected by statistical uncertainties.

When liquid and crystal phase are in equilibrium, the volume change $\langle dV/dt \rangle$, as a function of performed MC cycles t, is zero $\langle dV/dt \rangle \equiv 0$. If the volume as a function of MC cycles does not change, it means that both phases neither grow nor shrink. Therefore, the coexistence pressure p_{coex} can be identified as the pressure when $\langle dV(t)/dt \rangle \equiv 0$. The finite size effects need to be quantified to obtain reliable estimates for the coexistence pressure p_{coex}. In order We use 7 different system sizes for the softEffAO model and 6 for the EffAO model in order to test for finite size effects. The systems contain $N = 2230, 4000, 6100, 9250, 13300, 17800$ and 30540 particles, which corresponds to $n = 5, 6, 7, 8, 9, 10$ and 12 lattice planes in x- and y-direction.

We record the relative change of the colloidal packing fraction/volume at different pressures for all system sizes. The slopes were averaged over 100 independent runs and shown as a function of the pressure p in figure 5.3. In comparison to [42] the curves look quite similar. The values p_0 for which $\langle dV/dt \rangle \equiv 0$ are estimated using linear fits for every system size. Note that there is significant variation of the interface velocities with pressure, especially for the EffAO model. The limited amount of different values of pressures is a constraint for the accuracy of the obtained value for the coexistence pressure.

In addition, the finite size extrapolation represents another limitation, since the number of different system sizes is 7 and 6. The finite size scaling of the zero

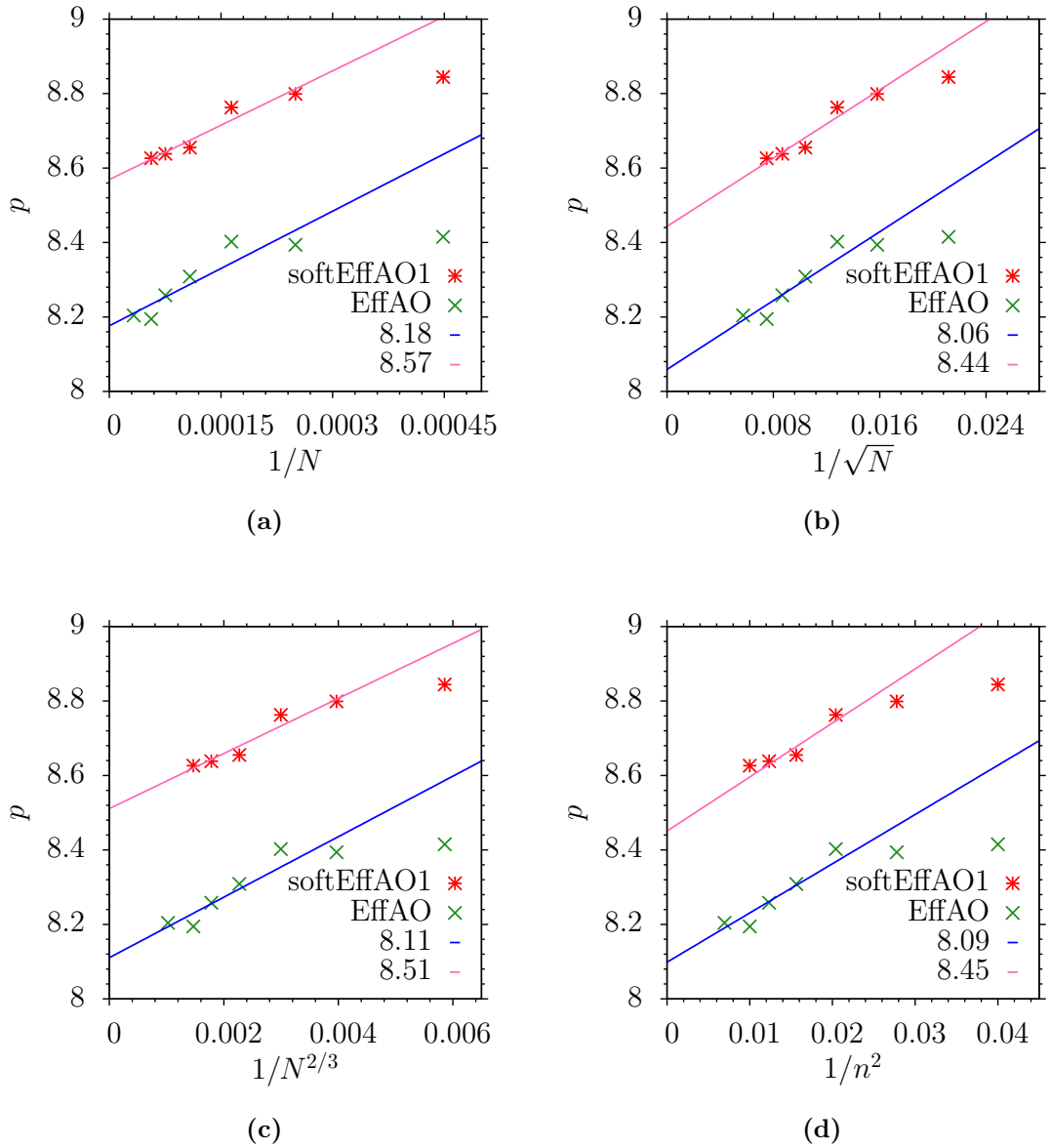

Figure 5.4: Finite size scaling for the pressure values p_0 from figure 5.3 for both models, as indicated. Note, that the smallest system size $N = 2230$ is not used to determine the values in the thermodynamic limit in each case. **(a)** Pressure as a function of $1/N$. Lines are fits to determine the limit $N \to \infty$. Resulting values for p_{coex} are given in the figure caption. Pressure as a function of **(b)** $1/\sqrt{N}$, function of **(c)** $1/N^{2/3}$ and of **(d)** $1/n^2$, where n denotes the number of lattice planes in the x- and y-direction.

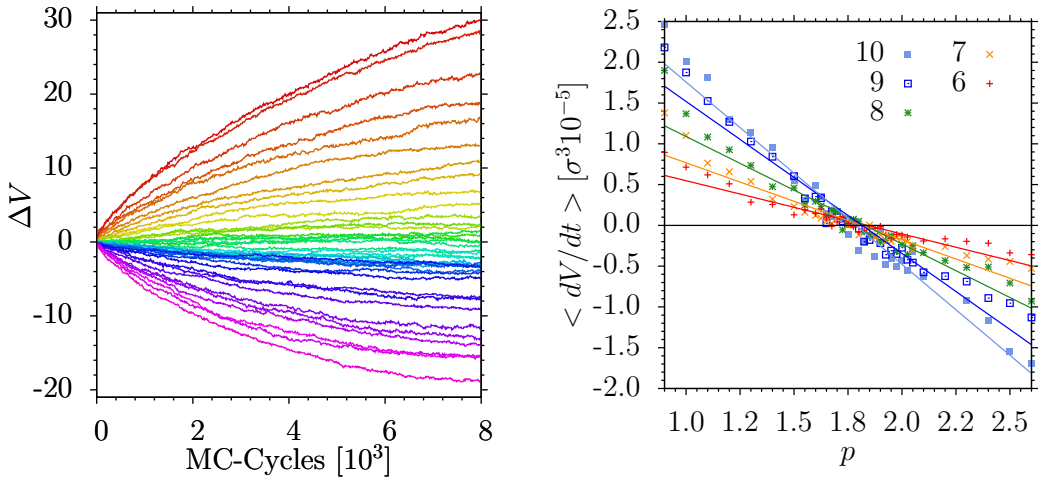

Figure 5.5: (a) Volume changes as a function of MC steps for $n = 10$ in the softEffAO2 model, colour indicates the value for the pressure, from $p = 0.6$ (red, top) to $p = 3.0$ (magenta, bottom). **(b)** Fit values from (a) for the volume velocities $\langle dV/dt \rangle$ for all different system sizes, as indicated. Only the values used in the fits are shown.

crossing p_0 for each system size is shown in figure 5.4. The smallest system size with $N = 2230$ was not included in the fits due to its rather large discrepancy to the linear behaviour. To estimate the coexistence value p_{coex}, different methods were tried. In the original work [42], an extrapolation of $1/N$ with N being the particle number, was used, as shown in figure 5.4 (a). However, they used a straight line for extrapolation and hence ignoring the finite size effects for the EffAO model completely. With this, they obtained a coexistence pressure of $p_{\text{coex}} = 8.00 \pm 0.03$. Our result, $p_{\text{coex}} = 8.18$ for the EffAO model, is not in agreement with the previously obtained result.

Using $1/\sqrt{N}$ as shown in figure 5.4 (b) gives a slightly better result. This result was reported in [82]. However, there is no physical reason for a scaling with $1/\sqrt{N}$. One would expect a scaling with the interface area, since this is the region where growing or melting is taking place, and hence determining the motion of the volume change. To include this behaviour, a scaling of $1/N^{2/3}$ was used, as shown in figure 5.4 (c). Unfortunately, the scaling is not as good as expected. There are several possible reasons for this: The volume should scale with the packing fraction, not with the number of particles. However, the total packing fractions as well as the packing fraction in the liquid and solid vary slightly for each system size in order to fulfil the requirements of correct lattice spacing and the constraint of $L_z \approx 5L$. The amount of liquid and solid volume can vary in each simulation, and therefore the total number of particles does not appear to be the correct scaling variable. Alternatively,

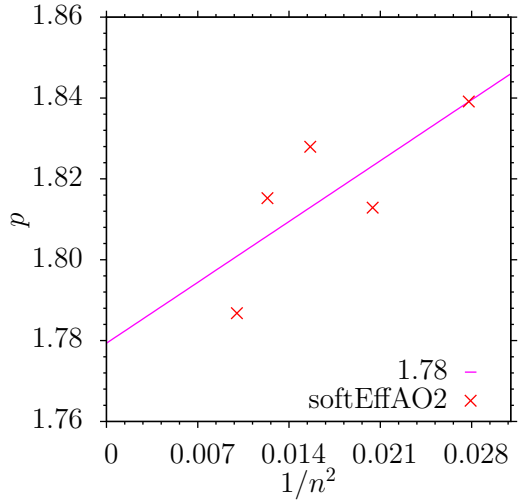

Figure 5.6: Zero crossing for the different system sizes of the softEffAO2 model as a function of $1/n^2$. The straight line shows the extrapolation to the thermodynamic limit, resulting in $p_{\text{coex}} = 1.78 \pm 0.02$ (all system sizes are used for the fit).

one can extrapolate the data as a function of the number of lattice planes in x- and z-direction for each system size, since this is a constant integer for each system size. The result is shown in figure 5.4 (d) and gives reasonable results for the coexistence pressure for both models. In [83] this finite size scaling was used. It yields to $p_{\text{coex}} = 8.45 \pm 0.04$ for the softEffAO1 model. Since the bulk phase behaviour is known, the freezing and melting packing fraction can be read off from the equation of state, $\eta_{\text{f}} = 0.494$ and $\eta_{\text{m}} = 0.696$.

For the softEffAO2 model, the same method was used but with fixed linear dimensions L_x and L_y. This allows a direct comparison and a check whether fluctuations in x- and y-directions are important for the interface velocity method. The solid branch of the softEffAO2 model is much steeper, as shown in figure 3.4 (c) and therefore the uncertainty in the lattice spacing for the crystal is smaller. To improve the accuracy of the extrapolation, more values for the pressure between $p = 0.6$ and $p = 3.0$ were used, as shown in figure 5.5 (a). Due to limited computational resources, we only simulated system sizes of $n = 6, 7, 8, 9$ and 10, with n being the number of lattice planes in x- and y-direction. These system sizes result in $N = 3600, 5300, 8000, 11500$ and 15500 particles respectively. For each pressure the volume development was averaged over 120 independent runs.

The slopes were obtained via linear fits of ΔV in the range of 0 to $6.5 \cdot 10^3$ MC steps. The functions ΔV are shown in figure 5.5 (a). They look similar to the volume curves for the softEffAO1 model, where all dimensions fluctuate, although they have a stronger curvature for very high and very low pressures. Note, that the range of simulated pressures is also larger. The zero crossing p_0 of the slopes $\langle \Delta V/dt \rangle$ are calculated with linear fits of the pressures between $p = 1.0$ and $p = 2.5$, as shown in figure 5.5 (b). In comparison to the softEffAO1 model, more values of the pressures near the zero crossing point have been used. From these values a finite size scaling is shown in figure 5.6 as a function of $1/n^2$. For the extrapolation all system sizes have been used and this results in

$p_{\mathrm{coex}} = 1.78 \pm 0.02$. Analogous to the softEffAO1 model, the freezing packing fraction $\eta_{\mathrm{f}} = 0.374$ and the melting packing fraction $\eta_{\mathrm{m}} = 0.688$ are calculated.

The difficulties of limited number of system sizes, as described above, unknown scaling behaviour and limited values for the pressure result in a serious limitation of the accuracy of the coexistence pressure in all models. Details of the fitting of the softEffAO2 model can be found in Appendix A. The overall quality of the obtained results is comparable to [42]. Therefore, the choice whether to fix L_x and L_y or not seems not to be crucial, provided, the crystal is in equilibrium without artificial stress.

6 CHEMICAL POTENTIAL

The determination of the chemical potential with the Widom particle insertion method as described in section 2.1.3 becomes more difficult for larger colloid packing fractions η. The reason is, that the space left for the "ghost" particle becomes smaller or the inserted particle has a very high interaction energy because of overlaps with the rest of the liquid colloids. As stated in [15], the insertion probability drops to $4 \cdot 10^{-5}$ for a dense hard sphere fluid with packing fraction $\eta = 0.4$.

To circumvent the problem of low insertion probabilities, we utilize that the chemical potential μ in a system in thermodynamic equilibrium is independent of the position in the system. This is also true for a system in which the density is inhomogeneous. Hence, the measurement of the chemical potential can be done in a low density region of an inhomogeneous system. A spatially inhomogeneous system can be created by introducing walls into the system. This idea is based on Powles et al. [84], although they are using external potentials instead of walls. The excess chemical potential μ_{ex} for a system including particle wall interactions is given by

$$\mu_{\text{ex}} = -k_B T \ln \langle e^{\beta(-\Delta U - \Phi)} \rangle_N^{-1} \tag{6.1}$$

analogous to equations (2.23) and (2.26). Φ is the interaction energy created by the walls. The chemical potential is given in units of $k_B T$. The value of μ is independent of the position within the system. Hence, the part $\langle e^{-\beta \Delta U} \rangle_N$ can

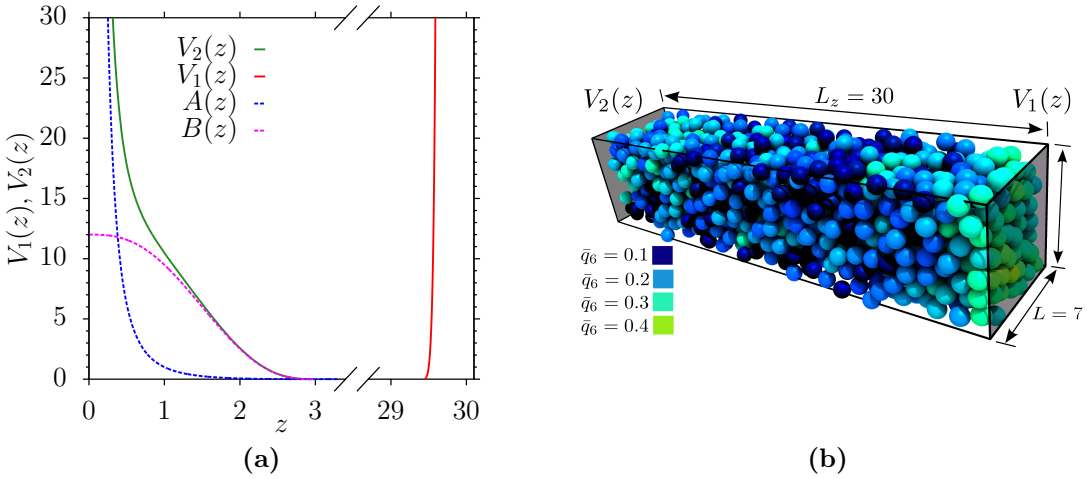

Figure 6.1: (a) Wall potentials for both walls as given by equation (6.2) and equation (6.3). The cutoff for the potentials is $z = 3.3$. **(b)** Typical configuration of the softEffAO1 model with walls. The box size is $7 \times 7 \times 30$ and contains $N = 1370$ colloids, resulting in $\eta_b = 0.5149$. The particles are coloured by their value of the bond order parameter $\bar{q}_6$, from blue $\bar{q}_6 = 0.1$ to green $\bar{q}_6 = 0.4$.

be measured with the Widom test particle insertion method near $z = 0$. For this method, the density distribution $\rho(z)$ is required, which can be measured at the same time during the simulation run.

We use a $L \times L \times D_w$ geometry, where the two walls are at distance D_w from each other. The x- and y-dimensions still obey periodic boundary conditions. The wall potentials and a typical configuration are shown in figure 6.1. The right/upper wall at D_w is implemented as a Weeks-Chandler-Andersen potential [85]

$$V_1(z') = 4\epsilon_{w1}\left[\left(\frac{\sigma_{w1}}{z'}\right)^{12} - \left(\frac{\sigma_{w1}}{z'}\right)^{6} + \frac{1}{4}\right] \qquad \text{for} \qquad 0 \le z' \le \sigma_{w1}2^{1/6} \quad , \tag{6.2}$$

where z' denotes the distance to the wall, $z' = D_w - z$. The strength of the wall is given by ϵ_{w1} and σ_{w1} sets its interaction range. We use $\epsilon_{w1} = 1$ and $\sigma_{w1} = \sigma_c/2$. The left/lower wall at $z = 0$ is a soft, repulsive wall

$$V_2(z) = \epsilon_{w2}\left[A(z) + B(z)\right] S(z) \quad , \tag{6.3}$$

where $B(z)$ creates a smooth repulsive hill and $A(z)$ is strongly repulsive:

$$B(z) = 16\left[1 - 10\left(\frac{z-\epsilon_{w2}}{z_c-\epsilon_{w2}}\right)^3 + 15\left(\frac{z-\epsilon_{w2}}{z_c-\epsilon_{w2}}\right)^4 - 6\left(\frac{z-\epsilon_{w2}}{z_c-\epsilon_{w2}}\right)^5\right], \tag{6.4}$$

$$A(z) = \left(\frac{\sigma_{w2}}{z-\epsilon'_{w2}}\right)^2 - \frac{\sigma_{w2}}{z-\epsilon'_{w2}} + \frac{1}{4} \quad . \tag{6.5}$$

We have chosen constants $\epsilon_{w2} = 0.8$, $\epsilon'_{w2} = 0.1$, and $\sigma_{w2} = 1.5$. The potential $V_2(z)$ is zero for $z > z_c = 2.2\sigma_{w2}$. The potentials $V_2(z), V_1(z)$ and the parts $A(z), B(z)$ are shown in figure 6.1 (a). The function $S(z)$ is a smoothing function applied [86] at the cutoff value and can be written as

$$S(z) = \frac{(z-z_c)^4}{h^4 + (z-z_c)^4} \quad , \tag{6.6}$$

where h is a constant chosen as $h = 10^{-2}$. Note that neither $V_1(z)$ nor $V_2(z)$ exhibit a discontinuity at their cutoff. The force is also continuous. The layering of the packing fraction $\eta(z)$ quickly reaches a horizontal plateau, due to the large range of σ_{w2} and the rather smooth variation of $V_1(z)$.

With some experimentation of using different choices for the wall potentials, $A(z)$ and $B(z)$ in equation (6.4)-(6.5) were found suitable, providing a reasonably broad regime of z near the wall where particle insertion works. Of course, a systematic investigation of other possible potential choices has not been done. We chose two different wall types to allow the simultaneous invest-

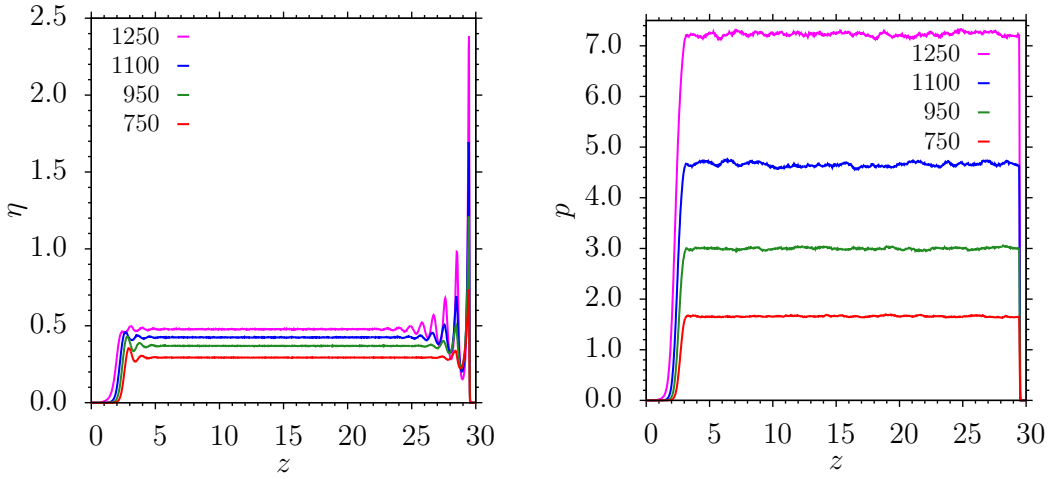

Figure 6.2: Illustration of the method to compute the chemical potential, for the case $L = 7$ and $D_w = 30$. Four choices of particle numbers for the softEffAO1 model are shown, as indicated. **(a)** Density profile $\eta(z)$ of the system. The bulk packing fraction is calculated as an average over the region where $\eta(z)$ is constant ($10 \leq z \leq 20$ in this example). **(b)** The pressure histogram $p(z)$ for the same systems as displayed in (a). Similar to the packing fraction, the bulk liquid pressure can be obtained in the region where it is constant.

igation of heterogeneous nucleation at the other wall. Note, however, that the here presented method does not require two different wall types.

The lateral dimensions of the simulation box as well as D_w need to be large enough to ensure that there is a constant packing fraction η_b in the middle of the box and that layering effects can be neglected there. Note that there is significant layering at the right wall [87], as indicated by larger order parameter values in figure 6.1 (b). A crystal would result in $\bar{q}_6 \approx 0.6$. Therefore, the calculated chemical potential μ corresponds to the bulk packing fraction η_b in the middle of the box. The bulk packing fraction η_b is larger than the total packing fraction $\bar{\eta}$ due to an excess density that occurs near the hard wall, where a pronounced layering is observed, and to the depletion of particles near the soft wall. At the lower wall only very small density oscillations are visible. The total packing fraction $\bar{\eta}$ differs from the bulk value η_b by

$$\bar{\eta} = \eta_\mathrm{b} + \frac{1}{D_w}\eta_{w1} + \frac{1}{D_w}\eta_{w2} \,, \tag{6.7}$$

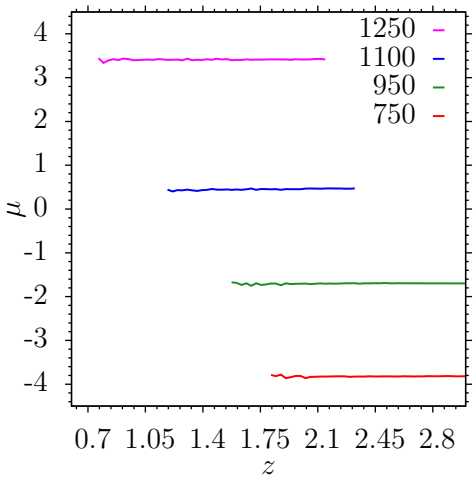

Figure 6.3: The chemical potential, for the softEffAO1 model, close to the left wall is shown for various choices of N in a box of size $7 \times 7 \times 30$. The chemical potential histogram is flat and proves that $\mu(z)$ is independent of z in this region as expected. We chose $0.03 < \eta(z) < 0.4$ for calculating μ. This choice translates into the ranges of z where μ is measured, as shown later. The bin size is $\delta z = 0.03$.

with wall excess corrections

$$\eta_{w1} = \int_0^{D_w/2} (\eta(z) - \eta_\mathrm{b}) dz \quad \text{and} \quad \eta_{w2} = \int_{D_w/2}^{D_w} (\eta(z) - \eta_\mathrm{b}) dz. \tag{6.8}$$

We adjust the total number of colloids in the system, corresponding to the value of the surface excess packing fraction to vary the value η_b. As figure 6.2 (a) shows, there is a extended region of constant η_b for various total packing fractions.

Additionally, the pressure $p(z)$ as a function of z is constant as seen in figure 6.2 (b). The total number of particles N in the system is indicated in figure 6.2. These choices of N result in $\bar{\eta} \approx 0.2671, 0.3384, 0.3918$ and 0.4452 (from bottom to top) for the softEffAO1 model. The corresponding estimates for η_b are $\eta_\mathrm{b} = 0.2933, 0.3690, 0.4241$ and 0.4777, respectively. The spatial resolution of the chemical potential is 1000 for all box sizes, the system was divided into 1000 bins in z-direction, which turned out to be sufficient. Since the system exhibits a large bulk region, the measurement of μ as a function of bulk packing fraction η_b and bulk pressure p_b is justified.

Near the left wall a broad slab of size $\Delta z \geq 1$ is formed, where the packing fraction $\eta(z)$ is small enough to use the Widom particle insertion method for an accurate sampling of the chemical potential as a function of z. In figure 6.3 the values of the chemical potential μ for each bin near the lower wall can be seen. The local packing fraction is roughly between $0.03 < \eta < 0.4$, which is suitable for measuring μ. A constant value of μ can be found even for strongly varying $\eta(z)$ in the region of z where the sampling of μ is done. This constant variation of μ, independent of z, is exactly what must occur in equilibrium and the small fluctuations around these constant values as seen in figure 6.3 give an idea of the magnitude of the statistical errors.

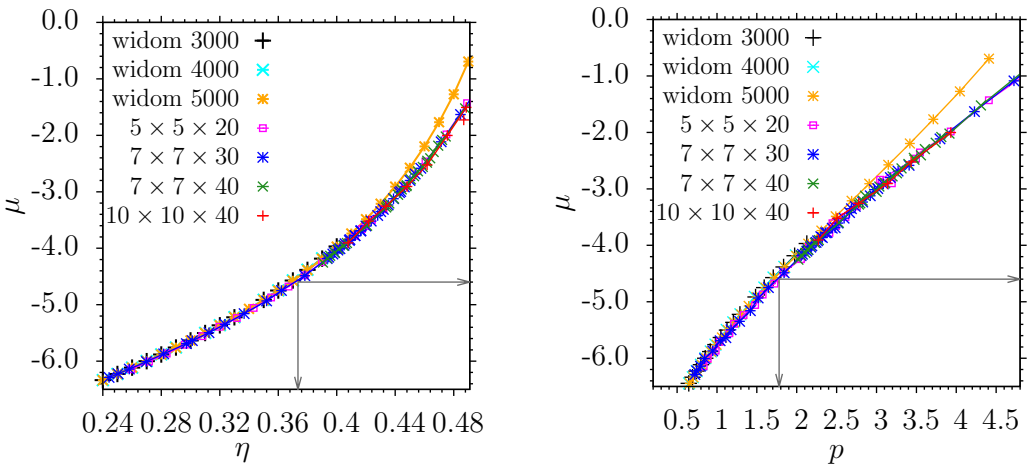

Figure 6.4: (a) Chemical potential for a liquid bulk phase of the softEffAO2 model. Points for lower packing fractions are determined by the Widom particle insertion method in a box $V = L \times L \times L$ with $N = 3000, 4000$ and 5000 particles. Four different system sizes with walls $D_w = 20, 30, 40$ and $L = 5, 7, 10$ are simulated. Arrows on abscissa and ordinate indicate η_f and μ_coex. **(b)** Chemical potential as a function of pressure for the same system as in (a). The arrows indicate p_coex and μ_coex.

The statistical fluctuations are too small to be clearly visible in figure 6.3. A satisfying accuracy of the function $\mu(\eta_b)$ in the fluid phase is reached, although the data is obtained only in a small fraction $\Delta z/D_w$ of the total volume.

The layering at the hard wall sets an upper limit for the usable packing fractions. For very large supersaturations the liquid will form a new crystal at the right wall and the bulk packing fraction η_b will drop accordingly. This process leads to an upper bound of accessible packing fractions. The layering does not influence the accuracy of the obtained data, as long as there is a bulk region in the middle of the simulation box. The measured bulk packing fraction and the chemical potential still correspond to each other in this case. If necessary, the right wall can be replaced by a soft potential to suppress layering and increase the region for the calculation of the chemical potential by a factor of 2. Note that the wall distance D_w needs to be increased to ensure a bulk-like subsystem in the middle of the simulation box. Alternatively, one can study heterogeneous nucleation at the hard wall and measure the chemical potential at the same time.

Simulations were performed for several different packing fractions below and slightly above η_f for the softEffAO1 and softEffAO2 model. Results are shown in figure 6.4 (a) for the softEffAO2 model in and figure 6.6 (a) for the softEf-

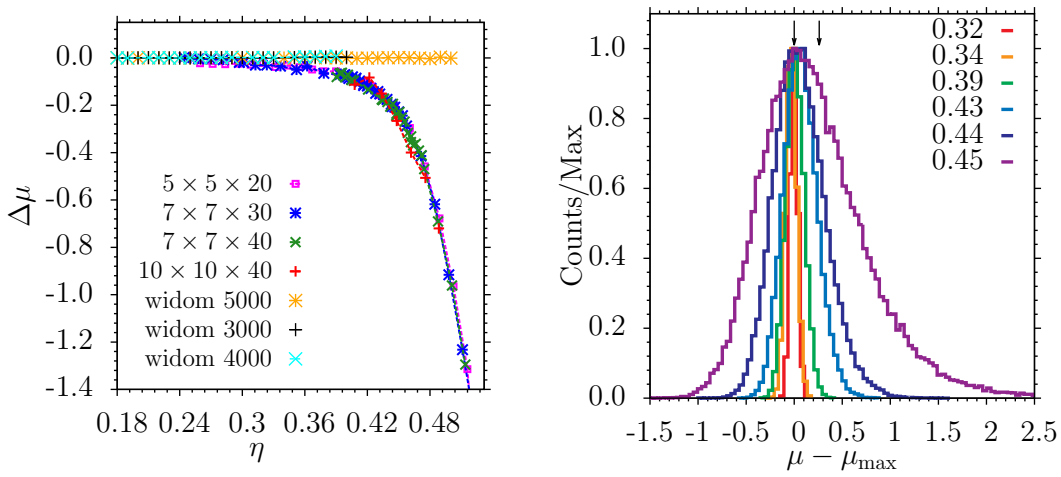

(a) **(b)**

Figure 6.5: (a) The difference $\Delta\mu$ as a function of the packing fraction η between the standard Widom method and the chemical potential determined in a system with walls. The data is obtained for the softEffAO2 model in different system sizes as indicated. The systems for the standard Widom method contained $N = 3000, 4000$ and 5000 colloids. **(b)** Histograms of μ for $N = 5000$ for different packing fractions η as labelled. Arrows indicate the position of the maximum and the mean for $\eta = 0.45$.

fAO1 model. In both cases, the fluid branch of the isotherm was simulated, including the metastable part. The homogeneous pressure $p(\eta_b)$ in the center of the box can be determined by the virial theorem and used to check that the system is truly representing a bulk liquid.

For the softEffAO2 model the liquid branch of the equation of state is at lower densities η. The freezing packing fraction is at $\eta_f = 0.374$, and therefore, the standard Widom particle insertion method is sufficient to obtain values for the chemical potential throughout most of the liquid branch. Standard Widom insertion method simulations were performed in a cubic system of size $V = L \times L \times L$ with variable size in order to change the packing fraction. The number of particles $N = 3000, 4000$ and 5000 were kept constant to check for finite size effects. As shown in figure 6.4 (a), there are no finite size effects for the chemical potential as a function of packing fraction. All system sizes are in agreement with each other. For slightly larger values of η, we use systems with walls to obtain the chemical potential. To analyse the finite size effects, we use four different box sizes. Both the wall distance D_w and box length L were varied to check for systematic errors. Apart from statistical fluctuations, no differences between the different box sizes are visible.

In figure 6.4 (b) the chemical potential as a function of pressure is shown for the same system sizes as in figure 6.4 (a). Again, there are no finite size effects

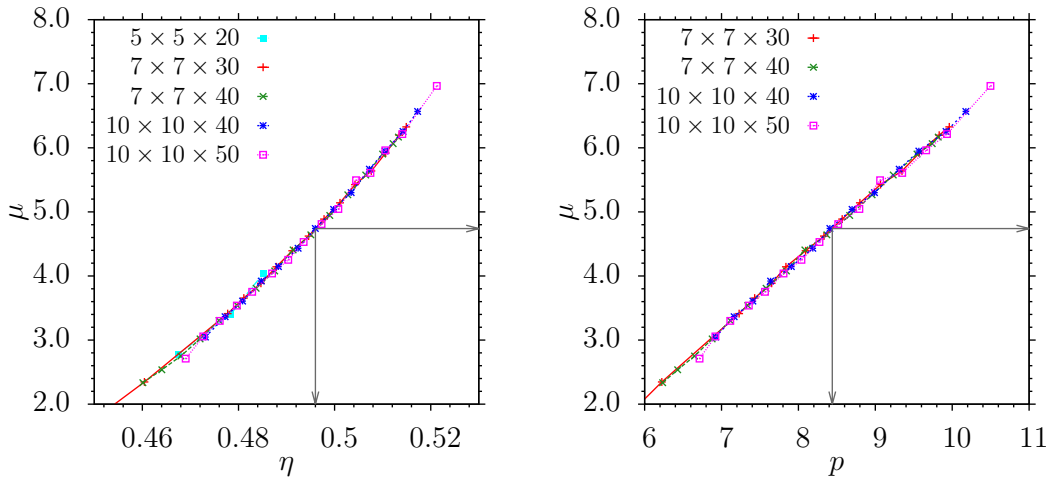

Figure 6.6: (a) The chemical potential μ plotted against packing fraction η for the softEffAO1 model. Different choices of L and D_w were used, as indicated. The coexistence values η_f and μ_coex are indicated by arrows. **(b)** The chemical potential μ plotted against pressure p, using the same data as in part (a). Arrows indicate the coexistence pressure p_coex and μ_coex.

as a function of system size for both methods of determining the chemical potential. While the data for the standard Widom method shows no difference as a function of system size, for higher packing fractions a substantial difference to the chemical potential measured by introducing walls to the system can be seen. The standard Widom method yields systematically higher results for μ. In figure 6.5 (a) the difference in chemical potential $\Delta\mu$ between both methods is shown as a function of the bulk packing fraction η. The obtained data match very well up to a packing fraction of approximately $\eta = 0.36$ and diverge above for the softEffAO2 model. As shown in figure 6.5 (b), the distributions of μ as a function of η become increasingly slanted for larger packing fractions. Therefore, the sampling of the tail of higher values of μ is an increasing problem in simulations for higher packing fractions. For low packing fractions the histograms have approximately a Gaussian shape. For the last shown histogram with $\eta = 0.45$, the position of the maximum and the mean is indicated by arrows.

In figure 6.6 (a) the chemical potential for the softEffAO1 model in the liquid is shown as a function of packing fraction, and in figure 6.6 (b) as a function of pressure. The freezing packing fraction for the softEffAO1 model is $\eta_\mathrm{f} = 0.494$ and therefore, the standard Widom insertion method cannot be used near η_f. Analogous to the softEffAO2 model different system sizes were used to check for systematic trends. As shown, there are no differences in the bulk liquid

packing fraction, chemical potential and bulk pressure for the used system sizes.

Since the described method relies on the same basic principle as the standard Widom insertion method, the chemical potential in crystals is not accessible with this method. For obtaining the solid branch we use thermodynamic integration as described in section 2.3. The bulk phase behaviour is known and therefore, we can determine the coexistence chemical potential μ_{coex} for both models by measuring the value at the freezing packing fraction. Using this value as starting point, the chemical potential in the solid can be calculated. The results are shown in figure 6.7 (b) and 6.7 (d) for the softEffAO1 and softEffAO2 model, respectively.

As shown in figure 6.7 (a) and 6.7 (c) the chemical potential as a function of pressure $\mu(p)$ is very accurately represented by a straight line near the coexistence point. A fit with a straight line is drawn in blue to illustrate equation (2.33). The expansions in section 2.3 are therefore validated and they introduce only negligible errors. All obtained coexistence bulk values can be found in table 6.1.

Table 6.1: Coexistence values for pressure p_{coex} and chemical potential μ_{coex}. Melting and freezing packing fractions η_{m} and η_{f} for all used models.

MODEL	η_{F}	η_{M}	p_{COEX}	μ_{COEX}
EffAO	0.494(2)	0.639(1)	8.09(4)	–
softEffAO1	0.494(2)	0.636(1)	8.45(4)	4.74(4)
softEffAO2	0.374(2)	0.688(1)	1.78(2)	-4.60(4)

In conclusion, the presented method provides a reliable and fast way of calculating the chemical potential in dense liquids. It is easy and straightforward to implement and offers several methods to check the results. The computational effort is modest, even if roughly 90% of the system is not used for the calculation of the chemical potential. The average CPU usage for the measurement of the chemical potential in a system containing walls was $4 \cdot 7200$ CPU hours whereas the standard Widom particle method needed $20 \cdot 7200$ CPU hours for comparable packing fractions and yields systematically wrong results. The possibility of changing the second wall can be used to study heterogeneous crystallization or bulk-like crystal phases at the second wall, provided the system size is large enough.

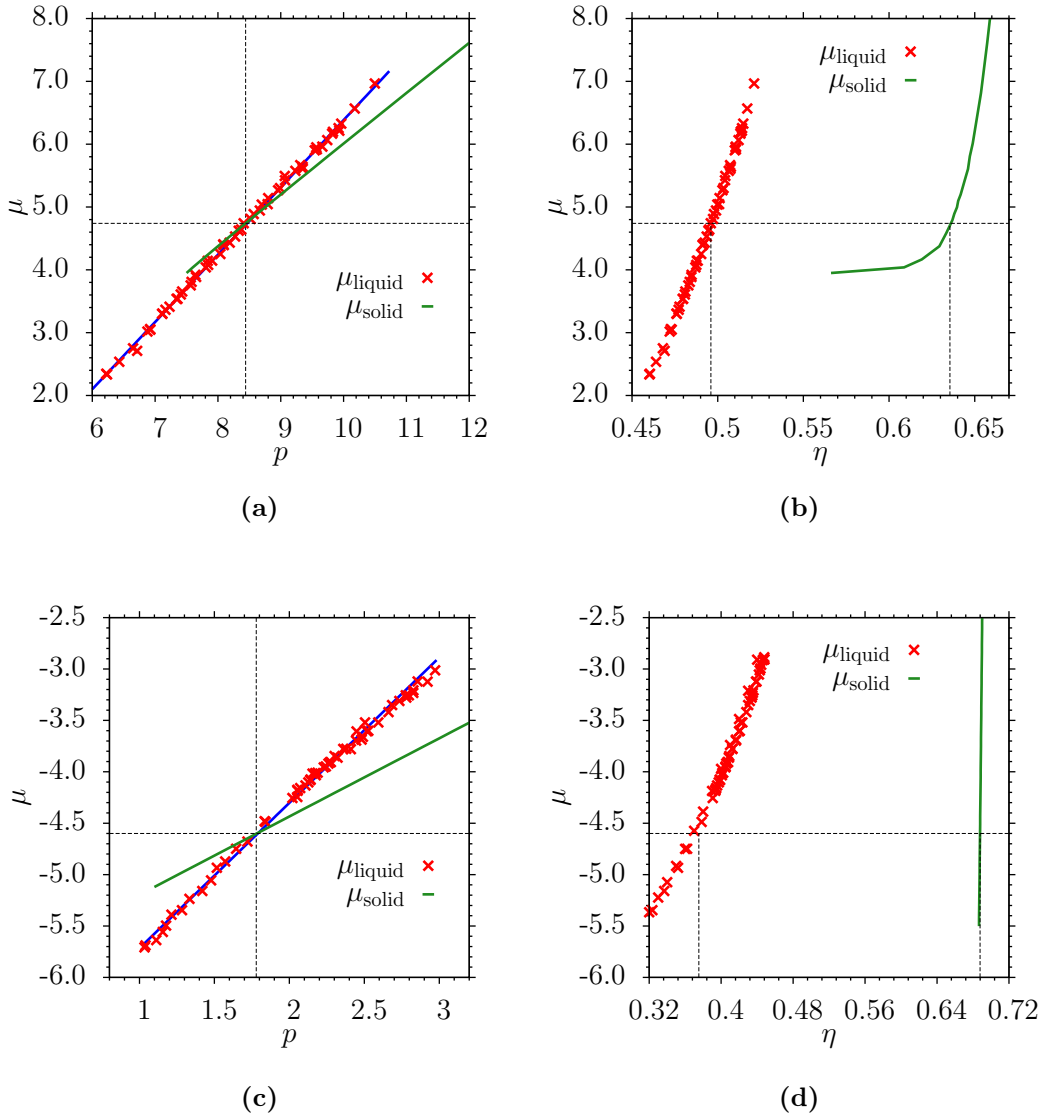

Figure 6.7: **(a)** Chemical potential as a function of the pressure of the softEffAO1 model. The liquid phase is shown in red, and a linear fit in blue. The green line shows the chemical potential in the solid. **(b)** Chemical potential as a function of the packing fraction for both phases of the softEffAO1. **(c)** Same plot as (a) but for the softEffAO2 model. **(d)** Analogous results as shown in (b) for the softEffAO2 model.

7 SIMULATION OF A CRYSTAL NUCLEUS IN LIQUID

7.1 PREPARATION OF AN INHOMOGENEOUS SYSTEM

To investigate the two-phase equilibrium of a crystalline nucleus surrounded by fluid a very careful preparation of the system is needed. The total packing fraction η needs to be chosen in the regime of (meta)stable nuclei, according to figure 2.2 on page 17. Unfortunately, the region of stable nuclei is dependent on the size of the simulation volume. If η, is chosen too low, the nucleus will dissolve and the box then contains a homogeneous liquid (that would be supersaturated in the thermodynamic limit and hence could not be stable, but represents the stable equilibrium in a finite simulation box). On the other hand, if η is too high, the stable configuration is a cylinder spanning over one of the three periodic boundaries of the system, or even a slab spanning over two of the periodic boundaries.

The range of packing fractions, which allows a stable nucleus is rather small. Therefore, at these low packing fractions (which turn out to be $0.5255 \leq \eta \leq 0.53$ for the softEffAO1 model and $0.466 \leq \eta \leq 0.49$ for the softEffAO2 model), we need to prepare the initial configurations for the simulations in such a way, that they contain a crystal nucleus seed. The inserted nucleus is chosen to have coexistence properties, including the lattice spacing at the coexistence pressure, since the pressure inside of the nucleus is not known a priori. The lattice spacing of the coexistence pressure ensures a stable crystal and is supposed to be close enough to the preferred lattice spacing at the solid pressure to allow equilibration without dissolving the crystal phase completely. So in this equilibration period, both the density in the crystal and the density of the surrounding fluid adjust to their proper equilibrium values at the resulting chemical potential, which is not known in beforehand.

As discussed in section 4.2, the shape of the crystal nuclei does not have to be spherical, therefore the volume and the shape of the crystalline phase is not known. Different shapes of the inserted nucleus seed are tested for the softEffAO2 model. A nucleus in form of a cube, a sphere, a octahedron, and a truncated octahedron were inserted into the simulation box as shown in the first column of figure 7.1. In all cases, the (111) orientation was placed parallel to the z-direction. The simulation box volume was $V_{\text{box}} = L \times L \times L$ with $L = 22.1778$ in this case, resulting in a packing fraction of $\eta = 0.48$. After insertion of the nucleus of size N_{fcc}, the remaining box volume is filled with the $N - N_{\text{fcc}}$ liquid colloids in a random manner, ensuring no overlaps between all particles.

For equilibration runs, that are long enough, e. g. roughly 10^{10} MC cycles, where each cycle consists of $N = 10000$ particle displacement attempts, all

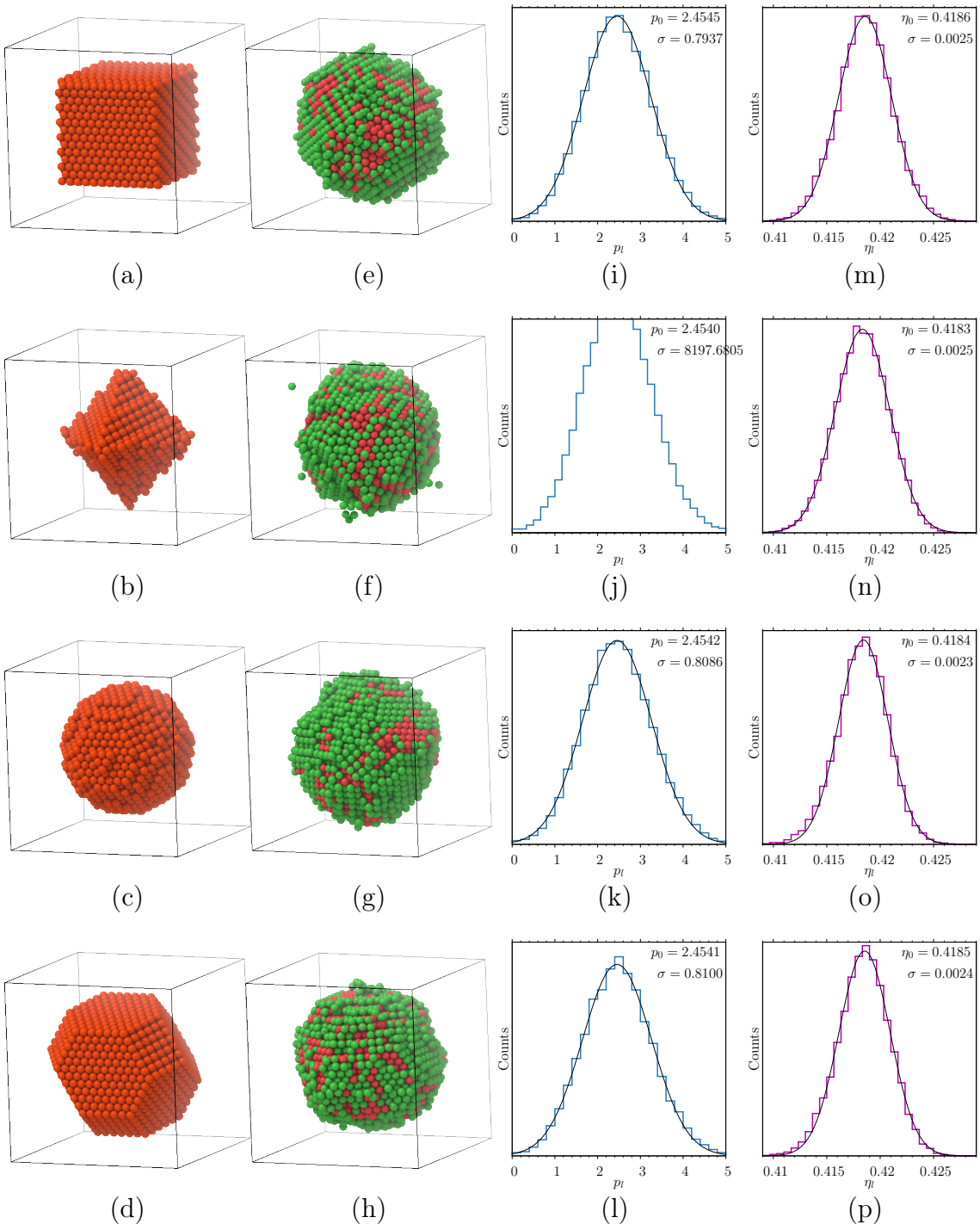

Figure 7.1: (a)-(d) Different crystalline seeds for the initialisation of the softEffAO2 model for $\eta = 0.48$ and $N = 10000$. The rest of the box is filled with liquid particles, not shown for clarity. **(e)-(h)** The nucleus shape after $\approx 5{\cdot}10^{10}$ MC cycles is displayed. Only solid particles (red) and interface particles (green) are shown. **(i)-(l)** Histogram of the pressure p_l in the liquid sub part of the system for each starting configuration. **(m)-(p)** Histogram of the average liquid packing fraction η_l. The histograms are obtained in a short run of $\approx 1 \cdot 10^6$ MC cycles.

nuclei shapes are leading to the same rather spherical equilibrium shape, shown in the second column of figure 7.1. During these equilibration runs, the lattice constant in the bulk crystal part of the system adjusts itself towards the value corresponding to the pressure in the solid part. The packing fractions η_c and η_l of the two phases are changed to the appropriate values by melting or growing of the nucleus seed. For testing purposes, the average packing fraction and the pressure in the liquid part of the system are measured in a short simulation of $\approx 1 \cdot 10^6$ MC cycles. Results are shown in figure 7.1(i)-(p). All nuclei seeds lead to the same Gaussian histograms and the mean values p_0, η_0 and widths σ are agreeing within statistical fluctuations. Nevertheless, we use henceforth a spherical nucleus as seed for all simulations of crystal nuclei to avoid any possible risk of introducing artificial effects from the initial seed shape.

We studied crystal nuclei for three different system sizes, keeping the number of colloids in the simulation box fixed at $N = 6000, 8000$, and 10000, respectively. For different packing fractions we varied L, changing $V_{\text{box}} = L \times L \times L$ and hence $\eta = N/V_{\text{box}}$.

7.2 VOLUME OF A CRYSTAL NUCLEUS

In section 3.4, we defined order parameters, which allow to distinguish between solid, liquid and interfacial parts of the system. For calculation of the nucleation barrier via equation (4.7)

$$\Delta F^* = \frac{1}{2}(p_c - p_f)V^* \quad , \tag{7.1}$$

one needs the average volume V^* of the crystal nucleus in the simulation box, as well as the pressure in the solid p_c and the fluid p_f. In the simulation, a crystal undergoes thermal fluctuations and is therefore not exactly given by the Wulff construction, even if one would be able to construct the shape according to this construction. There are many options to define the volume of a crystal nucleus in surrounding liquid. In the following, several different methods to estimate the volume are compared.

The first, most straightforward definition is to use the number of solid particles N_{fcc} identified by the order parameter values $\bar{q}_4$ and $\bar{q}_6$. This corresponds to the assumption, that all interface particles belong to the liquid phase. In order to calculate an average volume from this number, the specific volume ν_c of the solid is needed. We use the fact that the chemical potential μ is constant in the whole system, as stated before in chapter 6, to obtain an estimate for the solid packing fraction η_c. In the η, μ-plane, this corresponds to a horizontal line, and the crossing points of this horizontal line with both branches of $\mu_{\text{liq}}(\eta)$ and $\mu_{\text{fcc}}(\eta)$ in figure 6.6 can be used to extract the packing fraction of the solid, if

the packing fraction of the liquid η_l is known. The liquid packing fraction η_l can be easily measured during the simulations of the inhomogeneous system, only using the liquid part of the system. As shown in figure 7.2 (a) the volume calculated using the number of solid particles is rather low and does not match the visual impression from the snapshots, for example figure 7.1.

The exact location and width of the interface is not known, since this strongly depends on the choice of the order parameter as well as on the cutoff values for the order parameters. Hence, one can add half of the interface particles $\frac{1}{2}N_{\text{int}}$ to the crystal particles and calculate the volume using this particle number, corresponding to set the interface location at half of the width of the interface. The resulting volume shown in figure 7.2 (b) is obviously larger than figure 7.2 (a). However, there is no justification for adding exactly half of the interfacial particles, even if this seems to be a natural choice. Using particle numbers to define the volume of the nucleus suffers from several ambiguities[88–90, 42] and therefore should be not used to calculate nucleation barriers.

One rough estimate for the crystal nucleus radius is to use the half height width of the $\bar{q}_4$ and $\bar{q}_6$ histograms as shown in figure 7.3. A fit of a function with the shape

$$f(r) = \frac{\bar{q}_c - \bar{q}_l}{2} \tanh\left(\frac{r-R}{w}\right) + \frac{\bar{q}_l + \bar{q}_c}{2} \tag{7.2}$$

was used to obtain the radius R. The values $\bar{q}_c$ and $\bar{q}_c$ are the order parameter values in the bulk parts of the inhomogeneous system. As shown from figure 7.3 they can be treated as constants, since for both order parameters the histogram exhibits a plateau for small values of the distance to the center of mass $r < 3$ and large values $r > 10$. The remaining parameters for the fit are the width w of the interface and its location. The radius is then calculated as full width at half maximum height of both histograms. With this radius R a volume is calculated via $V(R) = 4/3\pi R^3$. The results for the softEffAO1 model are shown in figure 7.2 (c) and for the softEffAO2 model in figure 7.2 (e). The nuclei for the latter model are stable at lower packing fractions while being roughly twice as large. Of course, determining the volume via the radius ignores the possibility of anisotropic shapes completely. Due to the fact, that an average over many configurations is used, the result is still comparable to the other methods discussed in this thesis. For the estimation of effects caused by a non spherical shape, this method is not suitable.

A better method to determine the volume is to use a finite-size variant of the lever rule [91–93] while not using the particle numbers. For a nucleus in a large enough simulation box, the system can regarded as two independent subsystems, one containing the solid phase with N_{fcc} particles, and the other system the liquid particles N_{liq}. Therefore, the assumption of a equimolar dividing surface between the two phases is made, which states that the two phases can

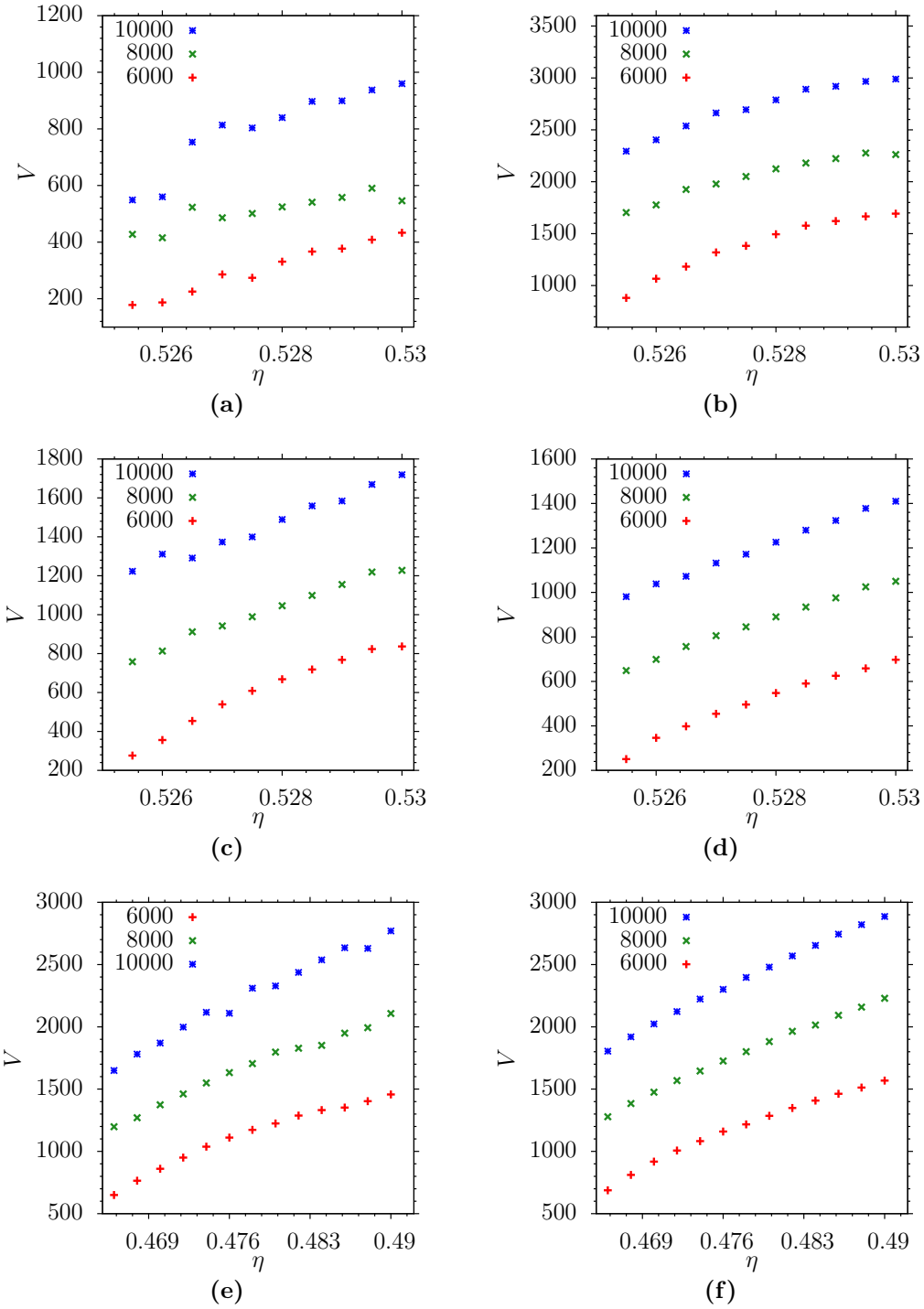

Figure 7.2: Nuclei volumes for the softEffAO1 model as a function of the total packing fraction η for all system sizes. Volume determined **(a)** by the number of colloids in the solid phase N_{fcc}, **(b)** by the number of colloids in the solid phase and half of the interface particles $N_{\text{fcc}} + \frac{1}{2}N_{\text{int}}$ **(c)** by radius determination via fits of $\bar{q}_4$ and $\bar{q}_6$ histograms as shown in figure 7.3 and **(d)** by the lever rule defined in equation (7.6). Volume of the nuclei for the softEffAO2 model determined **(e)** by radius determination via fits of $\bar{q}_4$ and $\bar{q}_6$ histograms and **(f)** by the lever rule.

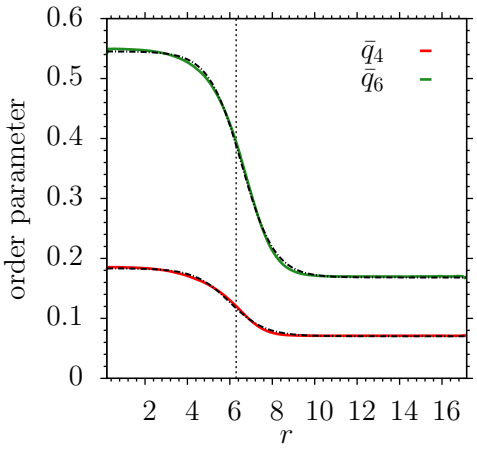

Figure 7.3: Example for the determination of the nucleus radius for the softEffAO1 model. The $\bar{q}_4$ and $\bar{q}_6$ histograms are shown. Fits according to the function (7.2) are shown in black and a radius of $R = 6.297$ is obtained, as indicated by the vertical line. The number of colloids given by $N = 8000$ and the total packing fraction is $\eta = 0.528$.

be separated by an infinitely thin interface [88], and hence no particles are counted as interface particles. The total number of colloids then is given by

$$N = N_{\text{liq}} + N_{\text{fcc}} \tag{7.3}$$

$$V_{\text{box}}\eta = V_{\text{liq}}\eta_l + V_{\text{fcc}}\eta_c \tag{7.4}$$

$$V_{\text{box}}\eta = (V_{\text{box}} - V_{\text{fcc}})\eta_l + V_{\text{fcc}}\eta_c \tag{7.5}$$

$$\rightarrow V_{\text{fcc}} = V_{\text{box}}\frac{\eta - \eta_l}{\eta_c - \eta_l} \tag{7.6}$$

Therefore, we need the colloid packing fractions η_l and η_c in the liquid and solid part of the system. Analogous to above, the fact that the chemical potential μ is constant, can be used to obtain these values. The total volume V_{box} and total packing fraction η are known. The results are shown in figure 7.2 (d) and figure 7.2 (f) for the softEffAO1 and softEffAO2 model, respectively. The volumes obtained with this method are comparable to those determined by the $\bar{q}_4, \bar{q}_6$ histograms.

In conclusion, we used the last method to determine the volume of the crystal droplet, since this method does not require to identify the interface on the level of particles and does not require any assumption on the nucleus shape. Therefore, the details of the bond order parameter analysis, for example the cutoff value, are not influencing the volume. In contrast to using the radius from the $\bar{q}_4, \bar{q}_6$ histograms, no assumptions about the shape of the droplet are needed. Hence, the volumes shown in figure 7.2 (d) and figure 7.2 (f) are used in the following section 7.3 to calculate nucleation barriers ΔF^*.

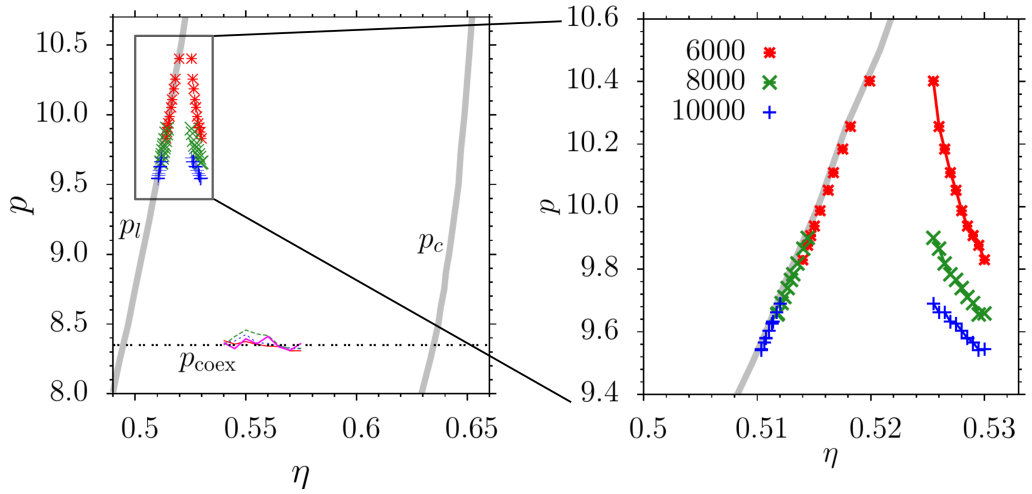

Figure 7.4: Pressure p_l in the liquid surrounding a solid droplet as a function of the total packing fraction η for the softEffAO1 model. Three choices of total particle number N are included and the grey lines indicate the bulk phase diagram. Data for $0.54 < \eta < 0.575$ are obtained in a slab configuration to confirm that the pressure agrees (apart from fluctuations) with p_{coex}. The region of interest is shown on the right with strongly magnified scales. Values for η_{f} are included and lie on top of the bulk equation of state for the liquid branch.

7.3 PRESSURE IN THE LIQUID SURROUNDING A DROPLET

For measuring the pressure in the liquid part of the system, one needs to exclude all crystal parts from the analysis. Since the nucleus is free to move in the whole simulation box, the complete system is shifted every $1 \cdot 10^5$ MC steps in such a way, that the center of mass of all crystal colloids is located in the middle of the box. The identification of crystal-like colloids was done by $\bar{q}_4$ and $\bar{q}_6$ values and equation (3.12). This step is not performed every MC cycle to enhance the efficiency, since the movement of the crystal cluster is rather slow in comparison to single particle movements. There is no need to identify the exact location of the interface, as shown in section 7.2. Hence, it is sufficient to disregard a spherical volume of radius R_{cutoff} inside the box for the calculations. In order to obtain an appropriate cutoff radius, the order parameters $\bar{q}_4$ and $\bar{q}_6$ for all colloids are calculated. Afterwards, the largest distance of an solid colloid $r_{\max}$ to the box center, which is the center of mass of the nucleus at the same time, is determined. The cutoff then is chosen to be $R_{\text{cutoff}} = r_{\max} + 2\sigma$, with σ being the colloid diameter, to ensure that the interface particles are not used for pressure calculations as well. The 2σ is constant for all simulations and is estimated by typical widths of the radial histograms of $\bar{q}_4$ and $\bar{q}_6$. However, there is a certain arbitrariness for the choice of the additional 2σ. A larger cutoff value would reduce the number of particles used for the pressure calculation even further and would result in poor statistics. Too small cutoff values lead

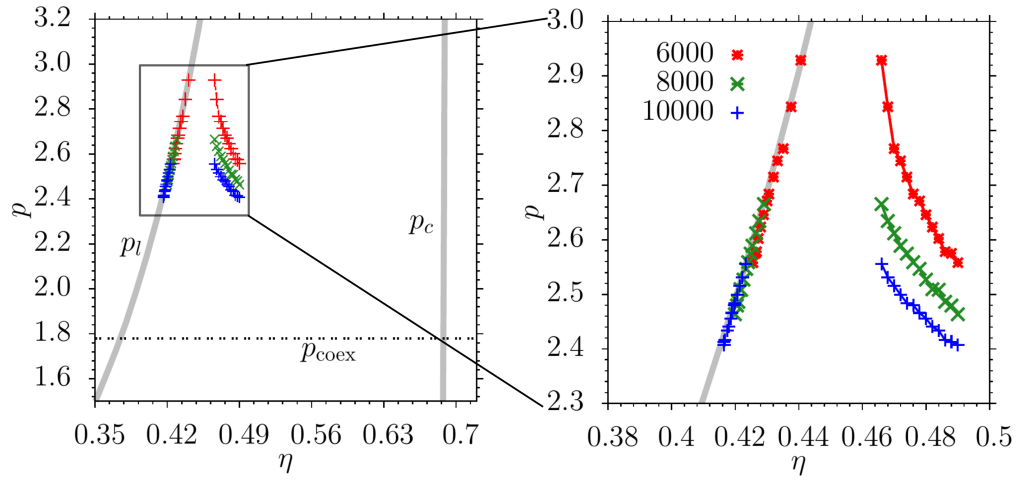

Figure 7.5: Pressure p_l in the liquid surrounding a solid droplet as function of the total packing fraction η for the softEffAO2 model. Grey lines indicate the bulk phase diagram. The region of interest is shown on the right with strongly magnified scales. Values for the packing fraction of the fluid η_{f} are included and lie on top of the bulk equation of state for the liquid branch.

to systematically wrong results, since it is possible that parts of the crystal or the interface are used to calculate the pressure. Therefore, it is desirable to choose a small but sufficient cutoff. The remaining particles in the liquid subsystem of volume V' are used to calculate the pressure p_l via the virial theorem. The virial theorem contains a sum over all forces between particles and hence there are surface effects occurring, when a part of the system is cut out, since neighbours of colloids near the nucleus are missing. In order to reduce these surface effects, the virial theorem in the following form

$$p_l = k_B T \rho_l + \frac{1}{6V'} \Big\langle \sum_{i \in V'} \sum_{j \neq i} (\mathbf{r}_i - \mathbf{r}_j) \cdot \frac{\partial U}{\partial r} (\mathbf{r}_i - \mathbf{r}_j) \Big\rangle \tag{7.7}$$

was used. The summation over $j \neq i$ takes colloids j into account, which may be located inside of the cutoff region to reduce surface effects due to missing neighbours. In the same simulation, the packing fraction η_{f} of the bulk liquid surrounding the nucleus was measured.

The results for all three different system sizes can be seen in figure 7.4 for the softEffAO1 and in figure 7.5 for the softEffAO2 model. The chosen total packing fractions are rather close to the liquid branch for both models, where the nucleus is stable. The distance of the stable crystal nuclei configurations to the liquid branch is smaller in case of the softEffAO1 model. In addition, the extent of the region where stable nuclei exist is smaller for the softEffAO1 model.

As expected for both models, the pressure measured in the smallest system size $N = 6000$, has higher values. The largest system size $N = 10000$ results in the lowest pressures. Therefore, the nuclei in the smaller system sizes are smaller and the curvature of their interfaces is higher. Additionally, the nuclei are larger for higher total packing fractions η, which lowers the measured pressure in the liquid. All measured curves follow the expectations as given in section 2.2.

The same data with enlarged scales is displayed in both figures 7.4 and figure 7.5, the packing fraction in the liquid is included. One can see, that the measured values of η_f are lying on top of the liquid bulk branch in both cases. Hence, the liquid surrounding the nucleus has indeed bulk properties and the chosen cutoff value is not too small and no artefacts of the crystalline part are measured in the liquid part.

7.4 LAPLACE PRESSURE AND HOMOGENEOUS NUCLEATION BARRIERS

In the previous chapters, all properties for calculating the LAPLACE PRESSURE are determined and hence equation (4.12)

$$p_\mathrm{f} - p_\mathrm{coex} = \frac{1}{\eta_\mathrm{f}}(\mu_\mathrm{f} - \mu_\mathrm{coex}) = \frac{2}{3}\frac{A_w\gamma}{V^{*1/3}\left(\frac{\eta_\mathrm{m}}{\eta_\mathrm{f}} - 1\right)} ,$$

can be used to obtain the Laplace pressure as a function of the total packing fraction in the inhomogeneous system. In figure 7.6 (a) and 7.6 (c) obtained results for all three sides of the equation (4.12) are shown. Values for the coexistence properties are used as they are given by table 6.1 for each model. For the prediction of the classical nucleation theory the interfacial tension γ is needed. For this, results of the ENSEMBLE SWITCH METHOD are used. The interface of the (111) orientation has the lowest value for the softEffAO1 and softEffAO2 model and since this should therefore be the interface exposed most to the liquid, γ_{111} is used in the following. This is an approximation of course.

Additionally, an estimation of the size of the (meta)stable nucleus is required. As shown in section 7.2, there are several possibilities to obtain an estimate of the volume. For comparison, the volume via the lever rule and the volume estimated by $\bar{q}_4, \bar{q}_6$ histograms are displayed figure 7.6 (a) and figure 7.6 (c) for the softEffAO1 and softEffAO2 model, respectively. For the constant A_w in equation (4.14) the value for spherical nuclei is used, $A_w = (36\pi)^{1/3}$, in both cases. Due to the fact that the nuclei are smaller for the softEffAO1 model, the Laplace pressure $\delta p = p_\mathrm{f} - p_\mathrm{coex}$ is larger than for the softEffAO2 model. As shown, the predictions of CNT lie significantly below the measured Laplace pressures for both models.

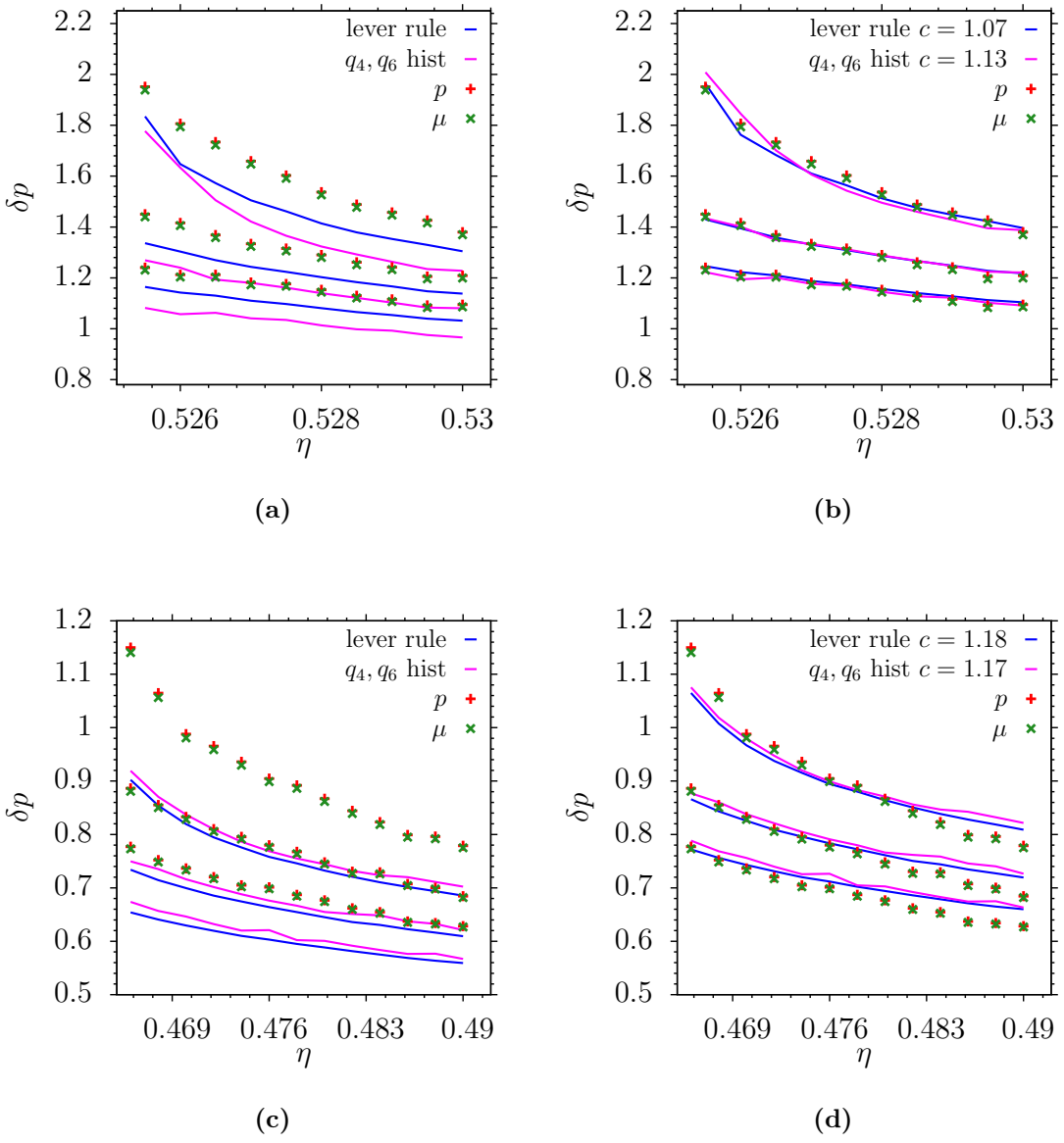

Figure 7.6: **(a)** Laplace pressure δp for the softEffAO1 model and the difference in chemical potential $\delta\mu$ (symbols) as a function of total packing fraction in the inhomogeneous system. Predictions from CNT for different volume definitions are shown (lines). **(b)** Same plot as in (a) but with scaled CNT predictions, using suitable values for c in equation (7.8). **(c)** Laplace pressure δp for the softEffAO2 model as in (a). **(d)** Same plot as in (c) but with scaled CNT predictions, analogous to (b).

Regardless of the specific way of determining the volume or the exact values, the results can be brought to a very good agreement if one introduces an additional scaling factor c to equation (4.12):

$$c \cdot \frac{2}{3} \frac{A_w \gamma}{V^{*1/3} \left(\frac{\eta_\mathrm{m}}{\eta_\mathrm{f}} - 1 \right)} \quad , \tag{7.8}$$

which can arise from several factors. First, the nucleus may not be spherical and therefore, A_w needs to be modified to take a deviation of the shape into account. Second, using the value γ_{111} for γ is a simplification, since this is a value for a flat interface and not a curved one and all other orientations, which are in fact exposed to the liquid, are ignored. The data are in almost perfect agreement for the softEffAO1 model, whereas small derivations are visible for the softEffAO2 model.

Apart from these effects related to the physical properties of the system, uncertainties in the coexistence value of the pressure and resulting shifts in μ_coex, η_f and η_m exist. For this reason, the two published papers [82] and [83] quote two slightly different values of the scaling factor for the curve obtained by the lever rule volume, namely $c = 1.07$ and $c = 1.1$. This difference is due to the finite size scaling method of the coexistence pressure, as shown in chapter 5. Note however, that the interfacial tension introduces an uncertainty of a few percent to the equation anyway.

To determine the nucleation barrier for homogeneous crystallisation, results from chapter 4 can be used, namely equation (4.7)

$$\Delta F^* = \frac{1}{3} A_w \bar{\gamma} V^{*2/3} = \frac{1}{2} (p_\mathrm{c} - p_\mathrm{f}) V^* \quad .$$

As shown in section 7.3, the pressure p_f of the fluid in the region surrounding the crystal nucleus can be measured using the virial expression. However, obtaining p_c inside the nucleus for small nuclei is not possible. Therefore, the pressure in the crystal p_c in equation (4.7) is replaced with equation (4.11)

$$p_\mathrm{c} = \frac{\eta_\mathrm{m}}{\eta_\mathrm{f}} (p_\mathrm{f} - p_\mathrm{coex}) + p_\mathrm{coex}$$

in order to be able to calculate ΔF without knowing p_c.

The resulting nucleation barriers are shown as a function of $V^{*2/3}$ in figure 7.7 for the softEffAO1 model. The data for the three different system sizes line up very nicely and no large finite size effects are visible. To illustrate the excellent agreement with classical nucleation theory, a fit is included, showing that $\Delta F^* \propto V^{*2/3}$ holds precisely in the regime where $\Delta F^* \geq 80$. As shown in figure 7.7 (b), the spherical approximation with $\gamma_{111} = 1.013$ is almost perfect.

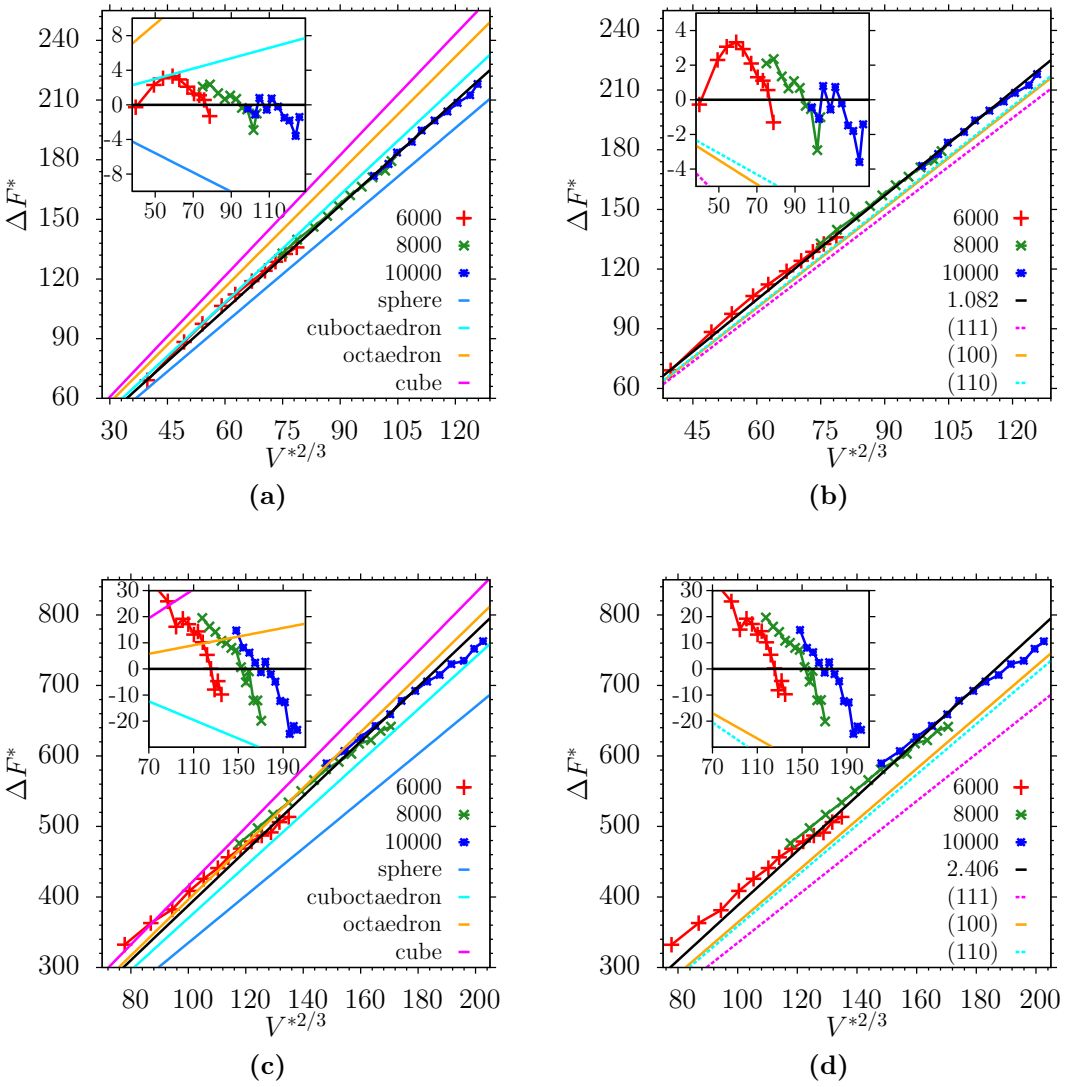

Figure 7.7: **(a)** Nucleation barriers for the softEffAO1 model (symbols). Lines show predictions of CNT with different geometries as indicated and a fixed value of $\gamma = 1.013$. The black line is a fit illustrating that the relation $\Delta F^* \propto V^{*2/3}$ holds precisely and the inset shows the difference of the data to the fit. **(b)** Same data as in (a), where straight lines are predictions of CNT assuming a spherical shape and different values for γ as indicated, $\gamma_{111} = 1.013$, $\gamma_{110} = 1.044$ and $\gamma_{100} = 1.039$. The inset shows the difference analogous to (a). **(c)** Nucleation barriers for the softEffAO2 model (symbols) **(d)** Same data as in (c), where straight lines are predictions of CNT assuming a spherical shape and different values for γ,$\gamma_{111} = 2.078$, $\gamma_{110} = 2.224$ and $\gamma_{100} = 2.256$. The inset shows again the difference of the data to the fit.

For comparison, other possible geometries are calculated and included and their corresponding nucleation barriers are higher than the numerical data. Since crystal faces in contact with a dense fluid are frequently atomically rough, the spherical approximation is expected to be quite good generally, in particular for somewhat smaller nuclei, for which the nucleation rates also would be larger. In figure 7.7 (b) the spherical approximation with the different values for the interfacial tension as calculated in section 4.3 is shown. In principle, one expects the interface with the lowest value for γ to be exposed to the liquid most, in this case the (111) orientation. However, the spherical approximation can be brought to a perfect agreement for slightly higher values of the interfacial tension. Assuming a sphere as nucleus shape and calculating $\tilde{\gamma}$ from the fit results in a value of $\tilde{\gamma} \approx 1.082$ for the softEffAO1 model.

For the softEffAO2 model the nucleation barriers are shown in figure 7.7 (c) and 7.7 (d). Here, the nuclei volume are slightly larger and the nucleation barrier is higher. Analogous to the figures for the softEffAO1 model, the spherical approximation is shown, using all known values for γ. For illustrating the relationship $\Delta F^* \propto V^{*2/3}$ a fit is drawn in both figures. From this fit, a value of $\tilde{\gamma} \approx 2.406$ is obtained. Larger systematic derivations from the fit are visible, and the curves for the different system sizes are not lining up perfectly, indicating larger finite size effects for the softEffAO2 model.

The packing fractions used for calculating the Laplace pressure are close to η_f due to the stability of the nucleus surrounded by liquid. As stated in section 7.1, lower values result in melting of the nuclei, whereas larger values would result in cylindrical solid phases. Therefore, the relative distance from the transition where freezing sets in $(\eta_l - \eta_\mathrm{f})/\eta_\mathrm{f}$ is limited to be at most $\approx 6\%$ for the softEffAO1 model and $\approx 19\%$ for the softEffAO2 model. In contrast, experiments [63] and simulations for hard spheres [6, 94, 95] are typically done for conditions where $(\eta_l - \eta_\mathrm{f})/\eta_\mathrm{f}$ is much larger than the values we used, resulting in total packing fractions of $0.53 < \eta < 0.57$. Note that this range of η for the experiments corresponds to huge values of $p_l - p_\mathrm{coex}$, and correspondingly the estimates for the critical radius R^* that classical nucleation theory would imply yields droplet radii that do not exceed about two colloid diameters, and barriers that are only of the order of 5 to 10 $k_B T$.

It is clear that for such small nuclei the approximations of the classical nucleation theory are expected to fail. On the other hand, for such dense colloidal suspensions the nucleation rate will be strongly affected by the slowing down that sets in when the colloidal glass transition [14, 96] is approached. Furthermore, Radu and Schilling [12] have pointed out a strong and nontrivial effect due to the kinetic prefactor of the nucleation rate. Since the slowing down associated with the glass transition is not a well understood problem [97], studies attempting to test nucleation theory should avoid this region, and focus on the region close to η_f, as done here.

8 CONCLUSIONS AND OUTLOOK

For the study of nucleation barriers and homogeneous nucleation with meaningful accuracy a soft variant of the well known Asakura-Oosawa model for colloid-polymer mixtures was introduced. The bulk phase behaviour was investigated and the phase coexistence pressure p_{coex} was determined by the INTERFACE VELOCITY METHOD. Unfortunately, this method requires a huge amount of computational resources due to large statistical fluctuations and finite size effects. More efficient and accurate methods to calculate p_{coex} are left for future work. Especially a method of PEDERSEN et al. [98] could be useful for this purpose.

For determining the chemical potential μ in very dense liquids, we have introduced walls to a system containing liquid. The key idea is to choose a wall potential that is repulsive and has a part that decays very slowly in the range where the strength of the potential is a few times the thermal energy. This has the consequence to create an extended region where the colloid density is rather low near the wall. This allows the estimation of μ in this region with the standard Widom particle insertion method. Hence, μ can be calculated for the liquid branch of the isotherm, even for pressures $p > p_{\text{coex}}$. The chemical potential of the system as a function of the packing fraction shows a loop, as discussed in section 2.2. With the presented method we are able to calculate the required values for the chemical potential with sufficient accuracy and feasible computational effort.

In configurations containing crystalline nuclei, the chemical potential μ as well as the pressure p_l in the liquid surrounding the nucleus are enhanced relative to μ_{coex} and p_{coex}, respectively. This difference in pressure and chemical potential contains information that can be used to estimate the surface excess free energy of the crystalline nucleus. Here, the difficulty is to find the correct packing fractions for (meta)stable nuclei in the finite system. The packing fractions depend on the system size.

To investigate the size of the crystal nuclei geometrical methods and thermodynamic analysis were used. The bond order parameters $\bar{q}_4$ and $\bar{q}_6$ were used to distinguish the phases locally. For the size estimation the number of solid particles N_{fcc} were used as well as $N_{\text{fcc}} + \frac{1}{2}N_{\text{int}}$. The bond order histogram can be used for obtaining an averaged radius of the nuclei. Even though this method ignores a possible shape anisotropy completely, the results are comparable. The size obtained by assuming a finite size version of the lever rule is the most accurate one and is based on no assumption of the shape of the nuclei and is therefore preferable. This latter treatment involves an equimolar dividing surface, i. e. no excess density is allocated to the interface. The density of the nucleus is taken to be the crystal density at the appropriate chemical

potential (which is homogeneous thorough the system, and hence taken from the fluid).

Despite several simplifications the classical nucleation theory is working rather well for the formation of liquid droplets from vapour. For the nucleation of crystals from melts, however, there are additional effects occurring.

First, the interface tension $\gamma(\mathbf{n})$ between a crystal surface and the fluid depends on the orientation of the unit vector $\mathbf{n}$ normal to the surface relative to the axes of the crystal lattice. The shape of the nucleus then is not a spherical droplet as in the case of vapour to liquid nucleation, but also exhibits an anisotropy. For strong enough anisotropy, facetted nanocrystals are expected. In general, the equilibrium crystal shape is non trivial and can only be obtained from $\gamma(\mathbf{n})$ via the Wulff construction as described in section 4.2. The interfacial tension of macroscopic flat interfaces can be used as first approximation of $\gamma(\mathbf{n})$. Due to limited computational resources, only the interfacial tensions of the (100), (110), and (111) orientation were calculated. The results are summarised in section 4.3. The corresponding calculations needed substantial computer resources and therefore the finite size scaling in the z-direction was not considered, assuming that the associated finite size effects are already negligible. The investigation of solid-liquid interfaces is clearly a challenging task and additional effort for this topic is desirable, although the computational costs are very high. An interesting question is the comparison of hcp nuclei with the fcc nuclei investigated in this thesis. Since the method here proposed is universal, it can be applied directly to different crystal structures. However, an explicit study of this case must be left to future work.

In addition, kinetic processes, such as the attachment of particles to the surface of a nanocrystal, may depend on the surface orientation [64]. If the nucleation barrier is not very high, and nucleation and growth proceed relatively fast crystal shapes, rather different from the equilibrium shape, could occur [63]. Since we performed Monte Carlo Simulations of stable crystal nuclei of rather large size, we are not able to investigate kinetic processes.

Often, the density at the melting/crystallization point is high and by increasing the density further, a glass transition is encountered [60]. At these high densities, the density dependence of the kinetic prefactor in the nucleation rate becomes an important factor [99]. Far from equilibrium, the separation of the nucleation rate into a static Boltzmann factor containing the nucleation barrier and a kinetic prefactor may be impossible. For the case of colloids described as a hard sphere liquid, the crystallisation transition is driven by increasing the density [5, 12, 14, 96, 100]. Similar problems arise if the crystallisation is induced by reducing the temperature: in fluids such as silica [61, 97, 101], strong supercooling is possible and ultimately a glass transition is reached. To avoid the problems arising due to glass formation, we chose rather low super-

saturations for our simulations. The glass transition is not investigated in this work.

We are only concerned with the first problem of predicting the nucleation barrier associated with the formation of crystalline nuclei. In our approach, we do not use any assumption on the anisotropy of $\gamma(\mathbf{n})$ or the shape of the nuclei. Closer investigation of the other effects is clearly desirable, but is out of scope for this thesis. This task must be left for future work.

We show that for the soft Asakura-Oosawa model with $\eta_p^r = 0.1$ the assumption that the anisotropy of $\gamma(\mathbf{n})$ can essentially be ignored, since the three calculated orientations for the liquid crystal interface show a difference of 0.31% only. Therefore, the investigated nuclei have effectively a spherical shape. However, this conclusion is not expected to hold in general. If the anisotropy $\gamma(\mathbf{n})$ is more pronounced, the spherical approximation must fail, but our thermodynamic method which only needs the information on the fluid pressure, fluid chemical potential, and nucleus volume, is still expected to work.

In the case of the soft Asakura-Oosawa model with $\eta_p^r = 0.2$, the anisotropy is slightly larger with 0.86%. The obtained nucleation barriers are higher and the difference to the prediction of the classical nucleation theory is more pronounced. It is desirable to perform simulations with smaller nuclei volumes to investigate the region where the nucleation barriers are also smaller.

In conclusion, we presented in the last chapters a reliable way to estimate the nucleation barrier without using the assumption of spherical nuclei and isotropic interfacial tension. The method can be applied to different stable crystal structures and adapted to several models. It is possible to investigate heterogeneous nucleation. The simulations for determining the chemical potential can be easily adapted for this purpose.

Part II

STRUCTURAL CROSSOVER

9 INTRODUCTION AND MODEL

It was pointed out by several groups, that there is an universal decay of the liquid structure for pure fluids and different fluid mixtures [102–107]. In 1969 Fisher and Widom found a line in the phase diagram of a simple liquid, which separates oscillatory and monotonic behaviour of the pair correlation function [108]. In this reference, an one-dimensional system was computed and it was concluded, that the same behaviour could occur in three dimensions. This line is called Fisher-Widom line and is shown in figure 9.1.

One implication of [108] is, that the average one-body density profile of an inhomogeneous fluid $\rho(r)$ is characterised equivalently to as the pair correlation function. The pair correlation function of a simple liquid in the long range limit exhibits an oscillatory, exponential decay with a characteristic length and an oscillatory wavelength. The density profile near a planar wall should, for example, exhibit the same behaviour. This also holds for liquid-vapour interfaces and has significant implications for the structure of these interfaces as stated in references [107, 109]. The value for the decay length and the oscillatory wavelength are determined by a bulk property, the pole structure of the Fourier transform of the direct correlation function $\hat{h}(r)$. Therefore, by understanding the asymptotic decay of the pair correlation function $g(r)$ insights in the details of the structure of interfaces can be gained.

A more recent experimental paper by Baumgartl et al. [110] investigated the behaviour of fluid mixtures in two dimensions. The authors of this paper relate the structural crossover to percolation of the nearest neighbour network. If a cluster in the system reaches from one edge of the system to the opposite edge, it is called a percolating cluster. The value of the packing fraction, where such a cluster occurs for the first time, is called percolation threshold. For a two component mixture in three dimensions, it is possible to have two percolating networks in the system.

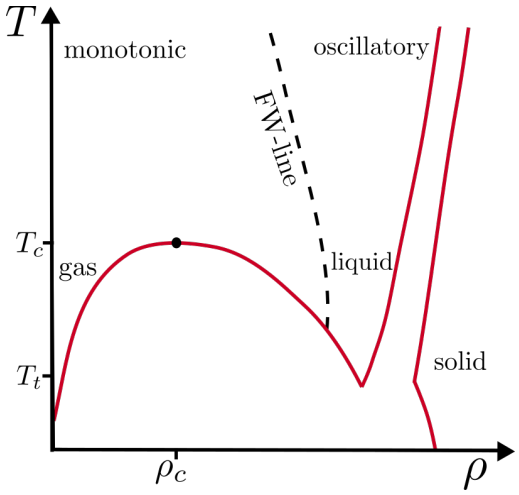

Figure 9.1: Sketch of a phase diagram (for a liquid with attractive forces) in the (ρ, T)-plane. For temperatures between T_t and T_c the liquid and gas phases are separated by a two phase coexistence region, for temperatures below T_t there is a gas-solid coexistence region, and for temperatures above T_t the solid and liquid can coexist in equilibrium. The dashed line indicates the location of the Fisher-Widom line. Adapted from [108].

In the following, the theory of the pair correlation function $g(r)$'s asymptotic behaviour is summarized, limited to the case of short ranged interaction potentials. Two component mixtures are discussed in section 11.2. The calculations in the next chapters are closely following the thesis of R. Leote De Carvalho [111] and related publications [107, 112–115].

In addition to theoretical calculations based on the Percus-Yevick approximation [116] Monte Carlo simulations, as well as experiments, were done to investigate the behaviour of mixtures of simple spheres. In these experiments colloidal particles were used to model hard spheres.

9.1 CORRELATION FUNCTIONS AND THE STRUCTURE FACTOR

The starting point for determining the structure and thermodynamic properties of a liquid is the pair interaction potential $U(\mathbf{r})$. The pair distribution function describes the distribution of distances between pairs of particles in the volume V. The pair distribution function $g^{(2)}(\mathbf{r}_1, \mathbf{r}_2)$ is given by

$$g^{(2)}(\mathbf{r}_1, \mathbf{r}_2) = \frac{\rho^{(2)}(\mathbf{r}_1, \mathbf{r}_2)}{\rho^{(1)}(\mathbf{r}_1)\rho^{(1)}(\mathbf{r}_2)} \quad , \tag{9.1}$$

where $\rho^{(n)}(\mathbf{r}_n)$ is the n-particle density. The total pair correlation function $h^{(2)}(\mathbf{r}_1, \mathbf{r}_2)$ plays an important role in the theory of simple liquids and is related to the pair distribution function by

$$h^{(2)}(\mathbf{r}_1, \mathbf{r}_2) = g^{(2)}(\mathbf{r}_1, \mathbf{r}_2) - 1 \quad , \tag{9.2}$$

which simplifies to $h(r) = g(r) - 1$ for isotropic systems, where r is given by $r = |\mathbf{r}_1 - \mathbf{r}_2|$. The radial pair correlation function $g(r)$ describes the probability of finding a particle i in the liquid at the distance r from particle j. If the pair correlation function and interaction potential is known, the pressure p and the potential energy U^{ex} per particle in the liquid can be calculated.

For obtaining $g(r)$ or $h(r)$ it is useful to define the direct correlation function $c(r)$. The direct correlation function was introduced by Ornstein and Zernike in 1914 for the first time [117]. They investigated density fluctuations near the critical point. For an isotropic homogeneous one-component system the direct correlation function $c(r)$ is defined by the Ornstein-Zernicke (OZ) equation

$$h(r) = c(r) + \rho \int c(|\mathbf{r}' - \mathbf{r}|)h(r')\mathrm{d}\mathbf{r}' \quad . \tag{9.3}$$

One can obtain a very simple form of this equation by Fourier transforming it and applying the convolution theorem

$$\hat{h}(q) = \frac{\hat{c}(q)}{1 - \rho\hat{c}(q)} \quad , \tag{9.4}$$

where $\hat{c}(q)$ and $\hat{h}(q)$ are referring to the three dimensional Fourier transforms of $c(r)$ and $h(r)$, respectively. Equation (9.3) needs to be solved for both $c(r)$ and $h(r)$. Alternatively, one can calculate $\hat{c}(q)$ and $\hat{h}(q)$ from equation (9.4). Therefore, one needs an additional equation, known as a closure relation. For the closure relation there are several possible choices, which are determined by the details of the system, especially the interaction potential $U(r)$. A widely used closure relation is the PERCUS-YEVICK approximation (PY) [116], which is suitable for particles with hard core interactions. This approximation and direct correlation functions for mixtures are discussed in more detail in Appendix B.

9.2 HARD SPHERE MODEL FOR SIMPLE LIQUIDS

The most simple model one can think of is the hard sphere model in 3D or hard disks in two dimensions. It was one of the first investigated models ever in computer simulations of liquids and phase transitions [118–120]. Due to the fact that the interaction is simple, an analytical theory is existing [121–124] and the usage of hard spheres as a model system dates back to KIRKWOOD [125] in 1942. One of the first experimental realisations was done in 1987 by PUSEY and VAN MEGEN [14]. They used a suspension of sterically-stabilised polymethylmethacrylate (PMMA) particles, which show hard-sphere-like behaviour. Later, the equation of state for hard-sphere-like colloids has been determined [126].

This model often serves as a basic approximation for systems with short ranged interactions due to its simplicity. The interaction between particles is given by

$$V(r) = \begin{cases} 0 & \text{for} \quad r \geq \sigma \\ \infty & \text{for} \quad r < \sigma \end{cases} \quad , \tag{9.5}$$

where $r = |\mathbf{r}_i - \mathbf{r}_j|$ denotes the distance between two particles i and j and σ is the hard-sphere diameter. Particles are not allowed to overlap and valid configurations have an energy value of exactly zero. Since this model includes no attractive forces, the value of the temperature has no influence on the phase behaviour. Nevertheless, the system shows a transition from a liquid state to solid fcc due to packing/entropy effects entirely. Hence, the packing fraction is the variable which controls phase behaviour. In this model, there is only one liquid phase and no vapour-liquid transition. The resulting phase diagram is shown in figure 9.2 (a) and is one dimensional. For $\eta < 0.494$, the hard

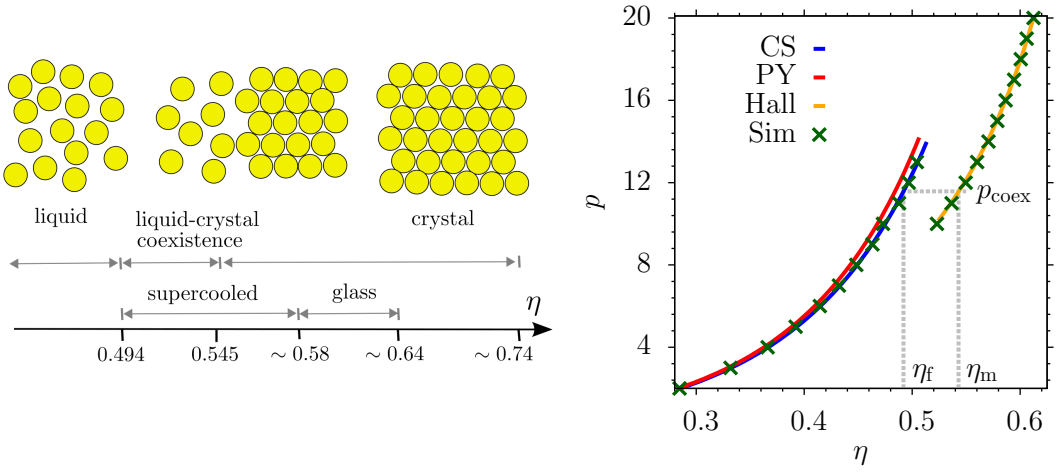

(a) **(b)**

Figure 9.2: (a) Sketch of the equilibrium phase diagram of hard spheres (there is only one control variable, density or pressure, the temperature does not play a role, so the "phase diagram" is just a line). The packing fractions for the phase transitions are indicated. The closest packing fraction of an fcc crystal is $\eta \approx 0.74$ and $\eta \approx 0.64$ for random close packing. The freezing transition occurs at $\eta = 0.494$ and the melting transition at $\eta = 0.545$. This picture is adapted from [127]. **(b)** Equation of state of hard spheres as a function of the packing fraction. Green crosses indicate NVT simulation results, the red curve shows the PY solution. The CARNAHAN-STARLING [128] solution is shown in blue. For the solid branch the equation of state from HALL [129] is included for comparison. The coexistence pressure p_{coex}, the melting and freezing packing fractions are indicated [42].

sphere is in the disordered liquid (or fluid) phase. For $\eta > 0.545$, the hard spheres form a crystalline fcc phase. The packing fraction $\eta = \frac{2\pi}{6} \approx 0.74$ is the maximum packing fraction, since then the hard spheres are close-packed. For $0.494 < \eta < 0.545$, the system separates into two coexisting phases and crystal nucleation occurs [130, 131]. In polydisperse colloidal suspensions, the boundaries between liquid and crystal are shifted, and also a glassy state [132] can occur, but we are not concerned with glasses in this thesis.

The equation of state for hard spheres can be obtained by Monte Carlo simulations and calculated by using the PY approximation or the CARNAHAN-STARLING approximation [128] as shown in figure 9.2 (b). As shown, the PY solution fits the simulation data very precisely up to high packing fractions, before it shows some deviations. Nevertheless, the PY approximation is an useful tool for predictions on the structure on the liquid.

10 EXPERIMENTS AND PARTICLE TRACKING

Invented in 1955 by Minsky [133, 134], confocal microscopy is an optical imaging technique to increase resolution and contrast of images obtained in experiments. A pinhole is placed at the confocal plane of the lens to eliminate out-of-focus light. This significantly increases image sharpness and contrast and led to many applications in numerous fields from medical diagnostics to geology. In this project, a laser scanning confocal microscope (Leica SP5 fitted with a resonant scanner, using a NA $63x$ oil immersion objective) is used to study colloidal binary mixtures. The pinhole blocks much of the light from the sample's fluorescence and therefore the signal intensity is decreased. By excluding out of focus light the pinhole enables the system to have a meaningful resolution in $z-$direction, hence, the pinhole leads to a diffraction limited point in x, y, and z. This enables the confocal microscopy to take 3D images. Since only one point in the sample is illuminated at a time, taking an image requires scanning over a regular raster. Parallel scanning lines result in a xy-

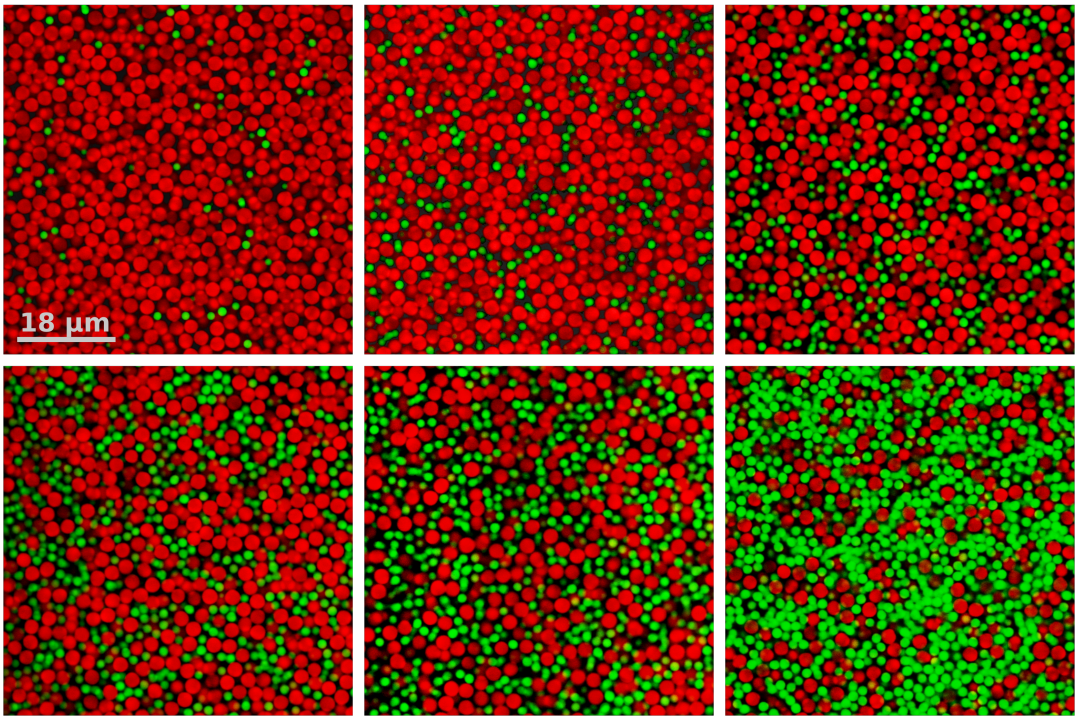

Figure 10.1: High resolution confocal microscopy images of the binary mixtures. 2D slices of systems with different relative volume fractions are shown. The green dyed small colloids are 1.88 µm in diameter and the large colloids are 2.9 µm. The scale bar in the upper left picture indicates 18 µm.

image of the sample, which represents a thin axial section. By scanning a series of the xy-images along the z-axis, a 3 dimensional image of the sample can be obtained.

For the investigation of binary mixtures, the different particle types of a single sample are labelled with different florescent dyes, where each dye emits at a different wavelength. Therefore, the signal output can be separated according to wavelength in different channels to display the spatial distribution of each labelled part. We used polymethylmethacrylate (PMMA) particles of size 2.9 µm and 1.88 µm, which are dyed with fluorescent rhodamine (red) and coumarin (green), respectively. High resolution images of a liquid mixture of the particles are shown in figure 10.1.

For preparing the samples, the colloids were solved in CHB-*cis*-decalin, which is chosen to match the density and refractive index of the PMMA particles. To screen charges and give hard-sphere-like interactions, the same mixture can be used with tetra-butylammonium bromide (TBAB) added to the CHB-*cis*-decalin solution. Note, however, that there remains a certain "softness" [40, 41]. The polydispersity was determined with static light scattering and is around 5% for the larger PMMA species. The smaller particle species was investigated with confocal images and the polydispersity was estimated to be of the same order as for the large colloids. A borosilicate glass square capillary with internal dimensions of 0.50×0.50 mm and glass thickness of 0.10 mm was filled with the suspensions and sealed on each end with epoxy glue to prevent evaporation.

After imaging the sample with the laser scanning confocal microscope, the particle coordinates have to be determined from the 3D volume. Essentially, the data from the microscope for each channel contains three coordinates (pixels, $p = \{i, j, k\}$) and the corresponding intensity $I(p)$ at this point in space. Due to simplicity, each channel is treated separately. The size of the image is $L_x \times L_y \times L_z$, where $L_x = L_y$ usually. The accuracy of finding and tracking particle coordinates depends on the image resolution, the particle size and the particle density.

The aim is to process the data in such a way, that an image is created, where each particle coordinate is represented by a region of high intensity, in which the pixel with the highest intensity is at the center of the particle. The basic assumption here is, that the particles are spherical and the locally brightest spot corresponds to the center of mass of the particle.

For this purpose a kernel (convolution matrix or mask) is applied to the input image I as a first step, as shown in figure 10.2(1) for one channel in a 2D slice. Note however, that the particle tracking algorithm is performed in 3D. The kernel is a binned Gaussian of pixel size $2l \times 2l \times 2l_z$ with height k_a and width k_b. The parameters for the kernel k_a, k_b as well as the size of the kernel can be tuned.

Since the axial resolution of the confocal microscope is around 600 nm, the particles can appear elliptical in z-direction. This is taken into account by an additional parameter z_e. The squared distance O to the Gaussian of each intensity value is calculated via

$$O[x-i, y-j, z-k] = \sum_{k=-l_z}^{l_z} \sum_{i=-l}^{l} \sum_{j=-l}^{l} \sum_{z=0}^{L_z} \sum_{y=0}^{L_y} \sum_{x=0}^{L_x} (I[x,y,z] - G[i,j,k])^2 \quad , \tag{10.1}$$

$$\text{where} \quad G[i,j,k] = k_a e^{-(i^2+j^2+(k\cdot z_\mathrm{e})^2)k_b} \tag{10.2}$$

and afterwards normalised. This procedure has the effect of smoothing and blurring the image slightly as shown in figure 10.2. The input image is shown on top (0) and the image with the applied kernel below (1). In figure 10.2, higher intensity pixels are black, whereas low intensity pixels are white.

As initial guess for the particle coordinates, a particle center is put at each pixel, whose intensity is higher than the intensity of all of its 26 neighbours. This step is visualised in figure 10.2(2). This can be used as a starting point for more refined estimates of particle positions, but misses a large percentage of the actual particles, since not every particle image will have one highest intensity pixel in the middle. It would be favourable to blur the image very strongly, since this would give Gaussian shaped images for each particle. Unfortunately, this is not possible for dense samples, since the blur also enlarges the area of the particle images and therefore the overlap between the particle images. In addition, due to imaging limitations, the image of a particle may appear slightly larger than the actual particle size, leading to apparent overlap and "smearing" between particles when particles are in close contact.

To improve the first guess, m particle centers are added randomly to the image at pixels $p = i, j, k$ in a second step. The particle diameter d in pixels and the number of inserted particle centers m are input parameters and are chosen at the beginning.

The algorithm can be described as follows

1. Apply kernel to original data
2. Perform initial guess on modified image
3. Add m particle centers randomly
4. Move all particles o times:
   a) Calculate the sum of the intensity values in a sphere of diameter d and volume V around the particle center p: $I_s(p) = \sum_{p' \in V} I(p')$
   b) Place the particle center at one adjacent pixel p_n
   c) Determine $\Delta I_s = I_s(p_n) - I_s(p)$ and
      i. if $\Delta I_s > 0$ move the particle center to the new pixel p_n
      ii. if $\Delta I_s \leq 0$ reject the move and stay at p
   d) Repeat step (a)-(c) for all 26 adjacent pixels
5. Remove overlap between all particles: keep the particle with higher $I_s(p)$ for each overlap
6. Repeat steps (3)-(5) n times
7. Remove "ghost" particles with $I_s(p) < I_{\min}$

Each particle is moved $o \approx 1.5d$ times, where d is the particle diameter, to ensure that the center of the particle can move to the closest high intensity spot. The move is deterministic and illustrated in figure 10.2(4). These moves do not take particle overlaps into account. Therefore, the last step in one cycle is to remove overlaps, as shown in 10.2(5). In order to decide which particle to delete, the sum of the intensity values for each overlapping particle is calculated and the particle with the highest value is kept. The complete cycle can be repeated n times to improve the results. From a computational point of view the application of the kernel is the most time consuming step. Adding particles and moving them is less computational effort and can be therefore repeated several times.

An isolated very high intensity pixel can give a false particle position, since the algorithm does take only the sum of intensities into account, not the distribution. Hence, particles with an I_s lower than a threshold value $I_{\min}$, the so-called "ghost" particles, are deleted as a last step in figure 10.2(7). The threshold is adjusted depending on the overall brightness of the image as well as on the level of noise in the image.

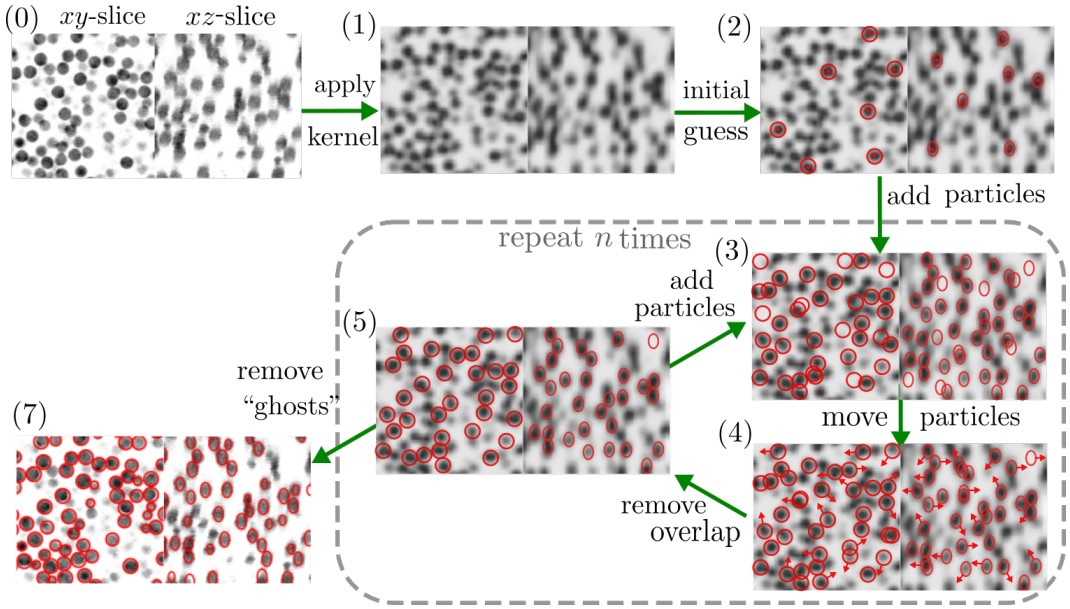

Figure 10.2: Sketch of the particle tracking algorithm for one channel for an 2D cut-out of the system in xy and xz-direction of size 122×122 pixel each. The applied kernel has parameters $k_b = 0.07$, $k_a = 250.0$, $z_e = 1.7$, and size 4. The image resolution is 0.251 µm per pixel in x- and y-direction, and 0.252 µm per pixel in z-direction. The particle positions at intermediate steps (1)-(5) only serve for illustrating purposes. For details refer to the text. The image (7) shows the actual output of the particle tracking.

The result of the particle tracking is shown in figure 10.2(7). As visible, the tracking is far from perfect, but gives reasonable results for the particle centers, if the appropriate input parameters were chosen for the algorithm. Crucial parameters are the kernel parameters for the Gaussian k_b and k_a and its size in pixel. Additionally, the approximate size in pixel of the particles must be known in order to ensure a good tracking.

For a mixture, the two channels are tracked separately and the overlaps between the two different particle types are removed afterwards. It is possible, that the light emitted by one fluorescent dye is recorded by the other detection channel. Even for a very good particle tracking, non-physical overlaps between the particles can appear. Since different particle types are dyed differently, the overall intensity and contrast of the channels, which are recorded at the same time, may differ as shown in figure 10.3 (a). Therefore, a direct comparison of the sum of intensities between the two channels is not possible. First, the distribution of the intensities of the particle images is determined and then the histograms are shifted and scaled so that the mean values and widths are on top of each other. One example is shown in figure 10.3 (b). This allows a comparison between the intensities of the two different channels. For each overlap the particle with the lower value of I_s^{norm} is deleted. This procedure leads to an

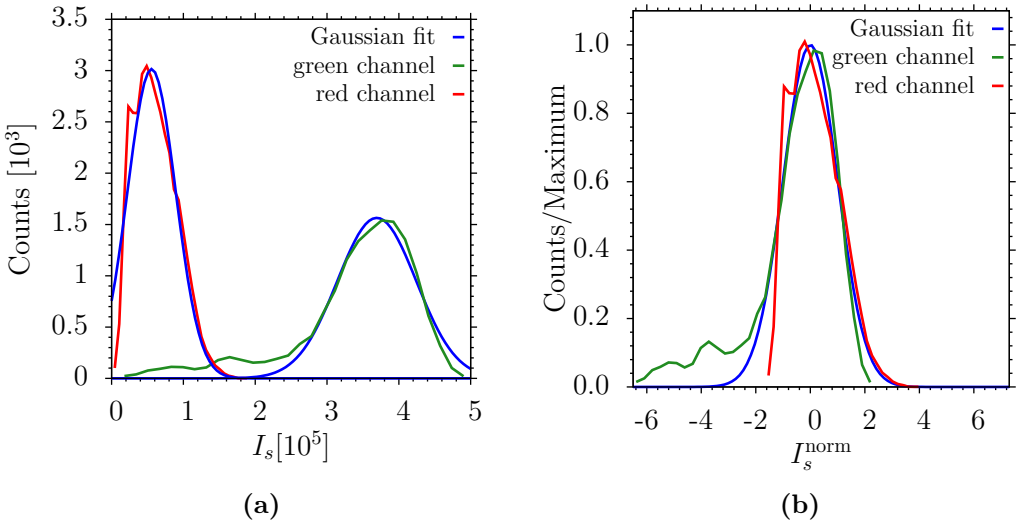

Figure 10.3: Histograms of the sum of intensities I_s for a two channel sample. The starting sets of coordinates contained $N_b = 14606$ red and $N_s = 37849$ green particles and after the overlap removal the sample contained $N_b = 13361$ and $N_s = 35770$ particles, corresponding to a loss of 5.49% and 8.5%. Part **(a)** shows the unscaled histograms and part **(b)** the scaled and normalised histograms which are used for the overlap removal.

additional loss of particles of around $5 - 15\%$. The result is a set of 3D pixel coordinates with no overlaps between the particles.

From the set of coordinates of the PMMA particles in the experiment, the pair correlation function $g(r)$ can be determined. Considering a homogeneous distribution of the particles in space, $g(r)$ represents the probability to find a particle in a shell of thickness $\mathrm{d}r$ at the distance r of another particle, which is chosen as a reference point. By dividing the sample volume into shells of thickness $\mathrm{d}r$, it is possible to compute the number of particle centers $\mathrm{d}n(r)$ at a distance between r and $r + \mathrm{d}r$ from a given particle. The pair correlation function $g(r)$ then is given by the following equation

$$\mathrm{d}n(r) = \frac{N}{V} g(r) 4\pi r^2 dr \quad , \tag{10.3}$$

where N represents the total number of particles and V the volume. For normalisation of the experimentally obtained pair correlation functions the pair correlation function of an ideal gas with equivalent density $\rho = N/V$ in a volume with exactly the same dimensions is used [135].

11 STRUCTURE AND CORRELATIONS IN SIMPLE FLUIDS AND THEIR MIXTURES

11.1 ASYMPTOTIC BEHAVIOUR OF $h(r)$ IN ONE-COMPONENT SYSTEMS

In this chapter, the pole structure of the OZ equation for a one-component liquid is investigated. First, general calculations are performed and afterwards predictions for the poles are calculated by using the PY approximation. As a last step, the results from experiments and simulations are compared to the PY calculations. Consider a system with an interaction potential $U(r)$ with a finite interaction range. Then one can calculate a Taylor expansion of the direct correlation function $\hat{c}(q)$ about $q = 0$ via

$$\hat{c}(q) = c^{(0)} + c^{(2)}q^2 + c^{(4)}q^4 + c^{(6)}q^6 + \dots \tag{11.1}$$

with

$$\hat{c}^{(2n)} = \frac{4\pi(-1)^n}{(2n+1)!}\int_0^\infty c(r)r^{2n+2}\mathrm{d}r \quad . \tag{11.2}$$

Since $\hat{c}(q)$ is even, all odd derivatives vanish. $\hat{h}(q)$ is even as well, and one can calculate that

$$rh(r) = \frac{1}{2\pi^2}\int_0^\infty \hat{h}(q)q\sin(qr)\mathrm{d}q \tag{11.3}$$

$$= \frac{1}{4\pi^2 i}\int_{-\infty}^\infty qe^{iqr}\frac{\hat{c}(q)}{1-\rho\hat{c}(q)}\mathrm{d}q \quad . \tag{11.4}$$

This equation is expected to have complex poles at $\alpha = \alpha_1 + i\alpha_0$ given by the condition

$$1 - \rho\hat{c}(\alpha) \equiv 0 \quad . \tag{11.5}$$

Using contour integration over an infinitely large semi-circle in the upper half complex plane, the right side of equation (11.4) can be calculated to

$$rh(r) = \frac{1}{2\pi}\sum_n e^{iq_n r}R_n = \sum_n e^{iq_n r}A_n \quad , \tag{11.6}$$

where A_n is the complex amplitude and q_n the n-th pole. R_n is the residue of $q\hat{c}(q)/(1-\rho\hat{c}(q))$ at $q = q_n$. In general there is an infinite number of poles [136]. Assuming that they are isolated, one can construct an appropriate

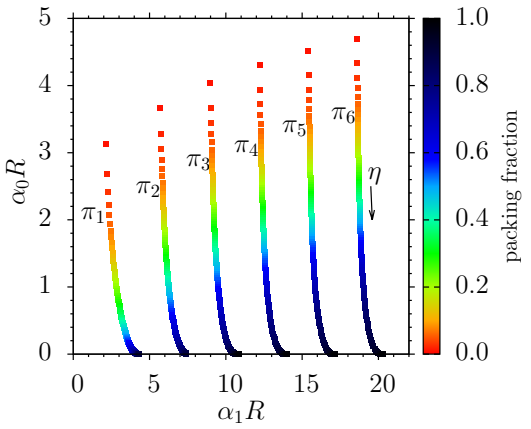

Figure 11.1: Pole structure of a one component hard sphere fluid in the PY approximation. R denotes the radius of the hard spheres. Colour indicates the value of the packing fraction from red $\eta = 0.01$ to black $\eta \to 1$. Note, that only $\alpha^+ = i\alpha_0 + \alpha_1$ poles are shown.

contour for integrating. The long range behaviour of $h(r)$ is determined by the pole with the smallest imaginary part.

Assuming simple poles, the residues can be calculated via

$$R_n = \frac{q_n}{\rho^2} \cdot \left(\frac{d}{dq} \hat{c}(q_n) \right)^{-1} \quad , \tag{11.7}$$

and therefore a pure complex pole $q_n \equiv i\alpha_0$ results in

$$rh(r) \sim Ae^{-a_0 r} \quad \text{with amplitude} \quad A = -\frac{i\alpha_0}{2\pi\rho^2 \frac{d}{dq}\hat{c}(i\alpha_0)} \quad . \tag{11.8}$$

Hence, a purely imaginary pole with $\alpha_1 \equiv 0$ results in a pure exponential decay of $rh(r)$. The poles fulfil the following equations

$$1 = 4\pi\rho \int_0^\infty r^2 c(r) \frac{\sinh(\alpha_0 r)}{\alpha_0 r} \cos(\alpha_1 r) \mathrm{d}r \tag{11.9}$$

and

$$1 = 4\pi\rho \int_0^\infty r^2 c(r) \frac{\cosh(\alpha_1 r)}{\alpha_1 r} \sin(\alpha_0 r) \mathrm{d}r \quad , \tag{11.10}$$

which are calculated by considering real and imaginary part of equation (11.5). Apart from the purely imaginary pole, these equations show that there are always conjugate pairs of poles. If $i\alpha_0 + \alpha_1$ is a solution to 11.9 and 11.10, it is straightforward to check that $i\alpha_0 - \alpha_1$ is a solution as well.

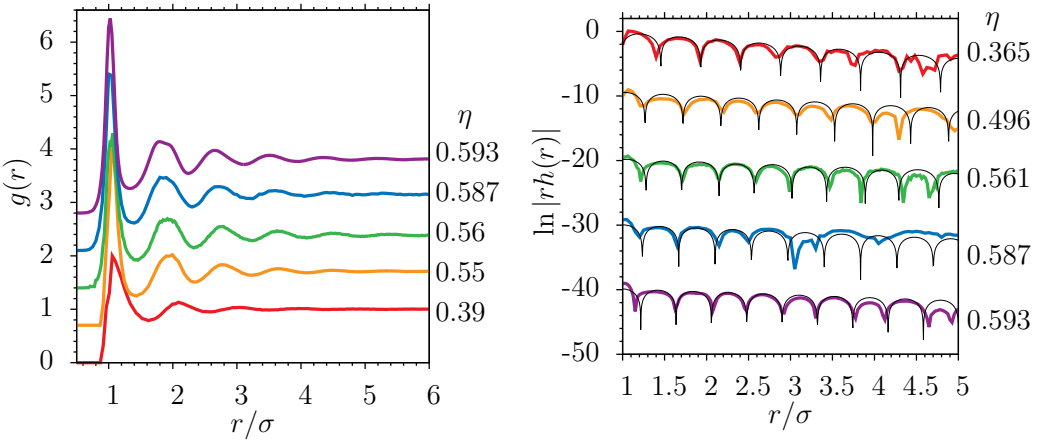

(a) **(b)**

Figure 11.2: (a) Pair correlation functions $g(r)$ of one component colloidal liquids in experiment for several different packing fractions η as indicated on the right. The curves are shifted vertically for clarity. **(b)** Resulting logarithms of the total correlation functions $\ln|rh(r)|$ from (a). The black lines are fits from which α_0 and α_1 are determined.

If $c(r)$ is of finite range, the pair of equations above can be used to calculate poles, hence the finite range ensures the existence of the integrals. A pair of complex poles $\alpha^{\pm} = i\alpha_0 \pm \alpha_1$ results in two contributions to equation (11.6) :

$$A^{+}e^{i\alpha+r} + A^{-}e^{i\alpha-r} \quad . \tag{11.11}$$

Since the amplitudes $A^{\pm}$ are complex, one can rewrite them to $|A^{\pm}|e^{-i\theta^{\pm}}$, where $|A^{\pm}|$ are real amplitudes and $\theta^{\pm}$ are real phases. As derived in [111] the following relations hold

$$|A^{+}| \equiv |A^{-}| = |A| \quad \text{and} \quad \theta = \theta^{+} \equiv -\theta^{-} \quad . \tag{11.12}$$

Therefore, the contribution from a complex conjugate pole to $rh(r)$ can be written as

$$rh(r) \sim |A|e^{-\alpha_0 r}\left[e^{i(\alpha_1 r-\theta)} + e^{-i(\alpha_1 r-\theta)}\right] \tag{11.13}$$

$$= |A|e^{-\alpha_0 r}\cos(\alpha_1 r - \theta) \quad . \tag{11.14}$$

Conjugate pairs of poles with $\alpha_0 \neq 0$ as well as $\alpha_1 \neq 0$m,accordingly, give rise to exponentially damped oscillatory behaviour of $rh(r)$ [102, 104, 106, 137] in the long range limit. The decay length is given by α_0^{-1} and the wavelength of oscillations by $2\pi\alpha_1^{-1}$. There are no poles on the real axis, apart from the liquid-vapour spinodal at $\alpha = 0$ and infinitely ranged oscillatory solutions [102] at very high densities ($\alpha_0 = 0, \alpha_1 \neq 0$), resulting from $\frac{d}{dq}\hat{c}(q_n) \equiv 0$ in equa-

tion (11.7). The calculations above hold in general for the above mentioned assumtions.

The FISHER WIDOM LINE is the line, where a pair of complex conjugate poles have exactly the same value α_0 as the pure imaginary pole. Hence, separating the two regions of either exponential decay or oscillatory behaviour of the total correlation function $h(r)$.

For calculating values for the poles α_0 and α_1, the direct correlation function is needed in equation (11.9)–(11.10). Therefore, we used the PY approximation in the following. As shown in figure 11.1 the first pole labelled with π_1 has the smallest imaginary part for all values of the packing fraction η. Hence, the hard sphere liquid in the PY approximation exhibits an exponentially damped oscillatory behaviour in the pair correlation function for all densities.

First, one component liquids in experiments were investigated. The samples were prepared at different packing fractions as indicated in figure 11.2 (a). For clarity, the pair correlation functions are shifted by a constant offset. The measurements of the two highest packing fractions were performed by ROYALL. The particles for these two samples had a diameter of 3230 nm and were dyed with rhodamine and hat a 6% polydispersity (determined with SEM). It is rather difficult to determine the packing fraction η in experiments [40]. Therefore, we fitted Fourier transforms of the structure factor given by the PY approximation. Details can be found in Appendix B and the fits are shown in figure C.2. From the pair correlation function $\ln|rh(r)|$ was calculated as shown in figure 11.2 (b).

For comparison, pair correlation functions of hard sphere fluids from simulations were calculated. The NVT-ensemble simulations were performed in a box of size $20 \times 20 \times 20$. For high packing fractions $\eta > 0.55$, the hard sphere fluid will start to crystallise. Therefore, the simulation time and maximum packing fraction are limited. Both experiment and simulations were fitted with the expected function from equation (11.14), as shown by the black lines in figure 11.2 (b) and 11.3 (a). For the experimental data, the fits are performed in the region $1.5 < r/\sigma_b < 4.0$ and the simulation results are fitted in a larger region $1.5 < r/\sigma_b < 5.5$. Due to the fact that the theory is valid only for the long range behaviour, the first peak in $\ln|rh(r)|$ is not matched perfectly for both cases. For simulation and experiment a very good agreement can be found in the used intermediate fit ranges. From the fits, α_0 and α_1 are calculated and compared to the PY approximation in figure 11.3 (b). A very good agreement between all data can be found. This shows that the theory for the long range oscillations is also applicable to medium ranges of approximately $1.5 < r < 5$. The results for the simulations are slightly above the PY approximation, which can be due to the fact that the PY approximation shows deviations for high packing fractions in the equation of state as visible in figure 9.2 (b). For $\eta > 0.55$, the α_0 does not decrease as the PY approximation

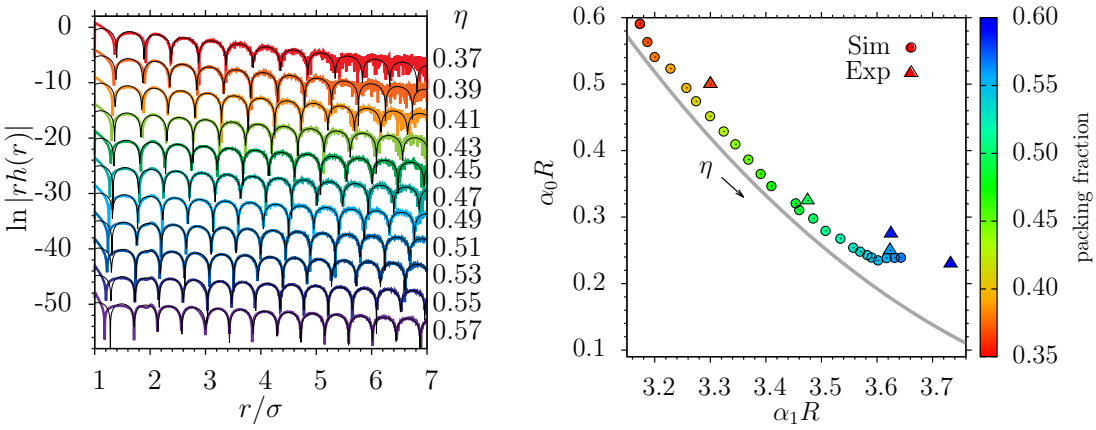

(a) **(b)**

Figure 11.3: (a) Results for $\ln|rh(r)|$ obtained by Monte Carlo simulations of a HS liquid at different packing fractions as indicated. The curves are shifted vertically. The poles $i\alpha_0 + \alpha_1$ are calculated by a fit, shown in black. **(b)** Comparison of the poles calculated from the experimental results (triangles), simulations (circles), and the PY approximation (line) for an one component HS fluid. The colour indicates the value of the packing fraction from red $\eta = 0.37$ to blue $\eta = 0.6$.

predicts, but stays constant, while the value α_1 increases further. The poles extracted from the experimental data for $\ln|rh(r)|$ are very close to the PY approximation for all measured packing fractions.

11.2 ASYMPTOTIC BEHAVIOUR OF $h(r)$ IN MIXTURES

In this thesis, only mixtures consisting of two different species of particles are considered. The simple case of hard spheres with two different diameters is investigated. Hence, the two different particles are labelled with b for "big" and s for "small" particles. The densities are denoted as ρ_s and ρ_b and the total density of the mixture is given by $\rho = \rho_s + \rho_b$. Three different pair correlation functions are existing in such a mixture, $h_{bb}(r)$, $h_{ss}(r)$ and $h_{bs}(r)$. Note, that the following analysis is valid for all kinds of two component mixtures and not limited to the simple hard sphere case. For a two component mixture the

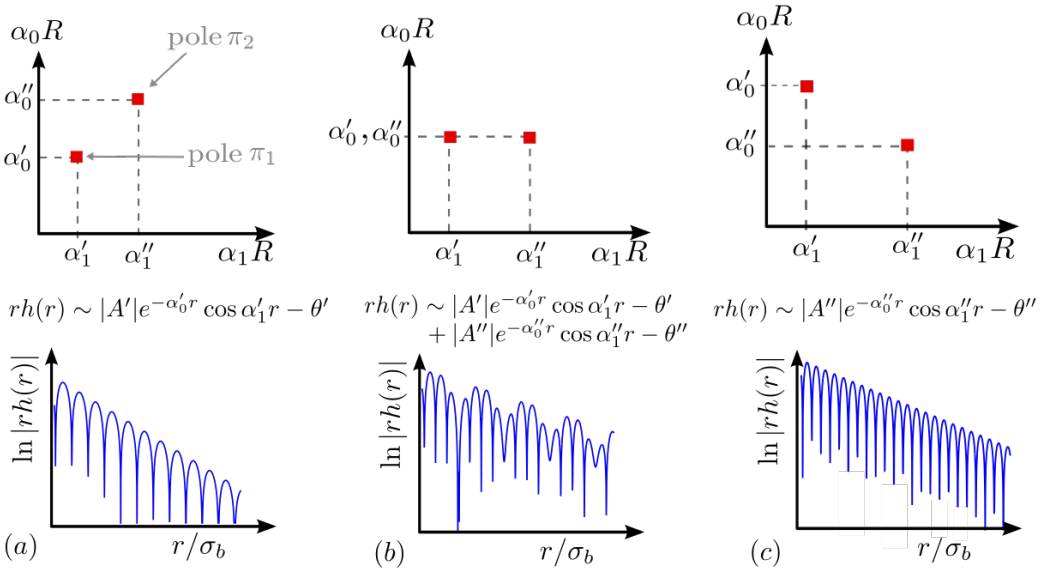

Figure 11.4: Sketch of possible pole structures of the α^+ for a two component fluid with $q \approx 0.5$. $h(r)$ denotes one example of $h_{ss}(r), h_{bs}(r)$ or $h_{bb}(r)$. **(a)** For small values of η_s, the pole π_1 has the lowest imaginary part with α_0' and the resulting $\ln|rh(r)|$ has oscillations of roughly the wavelength of the diameter of the larger particles σ_b. **(b)** For a sufficient high η_s both poles have the same imaginary part $\alpha_0' = \alpha_0''$ and a crossover occurs. **(c)** For even further increased packing fraction η_s, α_0'' is lower, and therefore the oscillation wavelength changes to roughly the diameter of the smaller particles, as shown in the bottom.

pole analysis provided in section 11.1 can be extended. The corresponding OZ equations in Fourier space are given by [138]

$$\hat{h}_{ii}(q) = \frac{\hat{c}_{ii}(q) + \rho_j \left[\hat{c}_{ij}^2(q) - \hat{c}_{ii}(q)c_{jj}(q)\right]}{D(q)} \tag{11.15}$$

$$\text{and} \quad h_{i\neq j}(q) = \frac{\hat{c}_{ij}(q)}{D(q)} \quad , \tag{11.16}$$

where i, j are labelling the two different particle species. Both correlation functions have a common denominator, which can be written as follows

$$D(q) = (1 - \rho_s \hat{c}_{ss}(q))(1 - \rho_b \hat{c}_{bb}(q)) - \rho_s \rho_b \hat{c}_{bs}^2(q) \quad . \tag{11.17}$$

Analogous to the one component case, the poles in the denominator determine the long range behaviour of $h_{ij}(r)$. Hence, all correlation functions $h_{ss}(r), h_{bs}(r)$ and $h_{bb}(r)$ exhibit the same common decay and oscillations in the long range limit for given values of η_b and η_s. They will only differ in their complex amplitude, hence, a real amplitude $|A|$ and a constant angle shift θ.

The control parameters of this kind of system are the packing fractions of both particle types, η_b and η_s and the size ratio q. In this thesis we are interested in

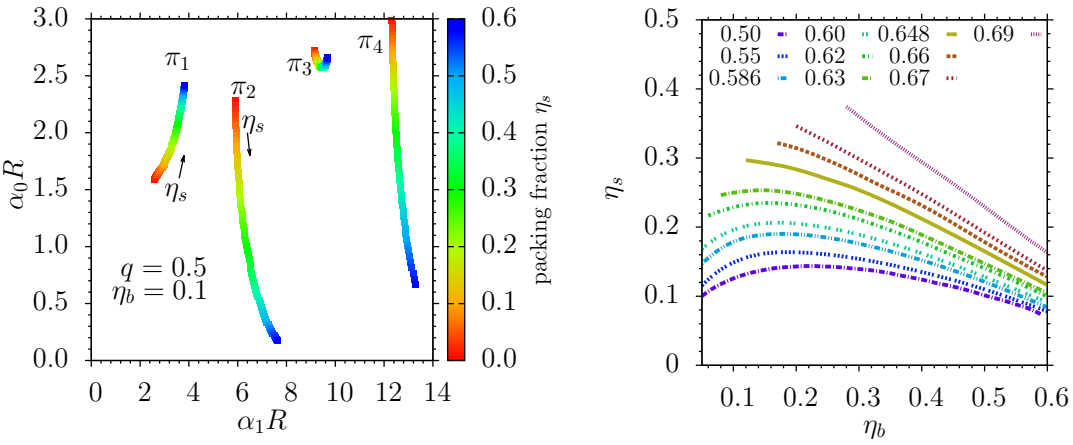

(a) **(b)**

Figure 11.5: (a) Pole structure for the α^+ of a two component hard sphere fluid in the PY approximation with size ratio $q = 0.5$ and fixed $\eta_b = 0.1$. Colour indicates the value of the packing fraction η_s from red $\eta_s = 0.01$ to blue $\eta_s = 0.6$. **(b)** Crossover lines in the (η_b,η_s)-plane for several size ratios, as indicated.

size ratios $1 > q \geq 0.5$ due to the experimental realisation. In contrast to the one component case, the pole π_1 of the denominator is not always the one with the lowest imaginary part. It is possible that the second pole π_2 has a lower value for α_0. As sketched in figure 11.4, for sufficient inhomogeneous mixtures, there is a crossover of the oscillatory behaviour in $h_{ss}(r), h_{bs}(r)$ and $h_{bb}(r)$. The oscillation wavelength changes from roughly the diameter of the large spheres to the diameter of the smaller spheres. The corresponding pole structure in the (α_0, α_1)-plane is shown in the top column and the resulting $h_{ss}(r), h_{bs}(r)$ and $h_{bb}(r)$ in the bottom row.

The pole structure for a fixed value of $\eta_b = 0.1$ is shown in figure 11.5 (a). For low values of η_s up to $\eta_s \approx 0.126$, the imaginary part of the pole π_1 is lowest. For higher values, π_2 has the lowest imaginary part. The imaginary part of other poles is higher on the full range of η_s. Hence, there is one crossover in the behaviour of $h(r)$ at $\eta_b = 0.1$, $\eta_s = 0.126$ for $q = 0.5$. These calculations can be performed for several size ratios q and packing fractions η_b, η_s. The resulting crossover lines are shown in figure 11.5 (b) in the (η_b, η_s)-plane. For each size ratio considered, the crossover occurs from π_1 to π_2, whereas above each line the pole π_2 dominates, resulting in larger oscillations than below, where π_1 dominates. For rather symmetric mixtures $q \geq 0.7$, the pole π_1 is always dominating and no crossover occurs. For slightly smaller size ratios, the crossover line is short. For a path which connects two points above and below the crossover line while not crossing the line, the poles change in a continuous manner.

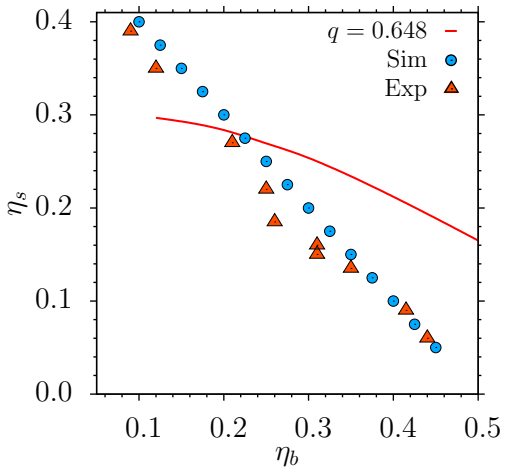

Figure 11.6: The packing fractions in the (η_b, η_s)-plane at which experiments and simulations are performed. The size ratio for the simulation is $q = 0.586$ and the total packing fraction is $\eta_{\text{tot}} = 0.58$ and for the experiments $q = 0.648$ and $\eta_{\text{tot}} \approx 0.5$. The lines show the corresponding crossover.

The mixtures are investigated in the same way as the one component fluids. Confocal microscopy images of the mixtures for different packing fractions are shown in figure 10.1. The larger colloids, dyed in red, have a size of 2.9 µm and the smaller colloids, dyed in green, are 1.88 µm large, resulting in a size ratio of $q = 0.648$.

For the experiments, we prepared the samples at high total packing fraction of roughly $\eta_{\text{tot}} \approx 0.5$, to ensure long range oscillations in the pair correlation function. Measurements of twenty samples in total were performed and ten are used for the analysis. The fraction of small and large particles was varied, as shown in figure 11.6. For the sample with the largest percentage of big particles this results in average particle numbers of $N_b = 18533$, $N_s = 3455$ and for the sample with the lowest percentage of big particles in $N_b = 2281$ and $N_s = 76935$. For each sample between 7 and 18 3D images were taken and the obtained pair correlation functions were averaged over the images. Detailed information for all used samples can be found in table C.1.

The packing fractions η_s, η_b and η_{tot} are determined by fits with Fourier transforms of the direct correlation functions given by the PY approximation. The results of the fits for the samples that were used in the analysis can be found in Appendix C. The obtained correlation functions $\ln|rh_{ij}(r)|$ are shown in the second row of figure 11.7

The simulations are performed at a higher total packing fraction of $\eta_{\text{tot}} = 0.58$. The size ratio is $q = 0.586$. All values used for η_s, η_b are shown in figure 11.6. All correlation functions $\ln|rh_{ij}(r)|$ are shown in the first row of figure 11.7. For all correlation functions shown, the amount of large particles increases from top (blue) to bottom (red). Consequently, the amount of small particles decreases from top to bottom and hence the oscillation wavelength is roughly the diameter of the small particles σ_s for the curves on top. At the bottom of each figure, all $h(r)$ show oscillation wavelengths of the order of the diameter

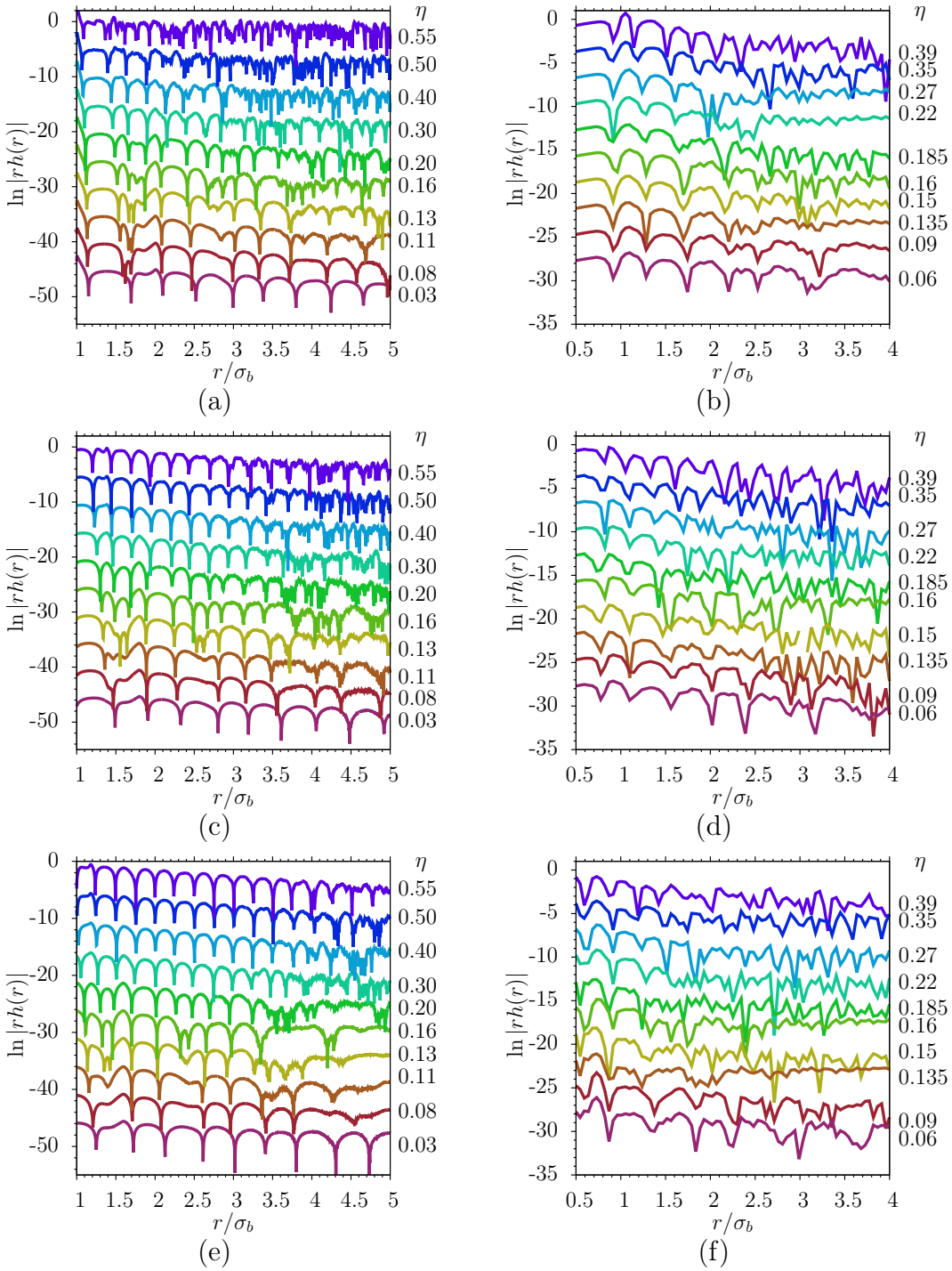

Figure 11.7: Direct correlation functions $\ln|rh_{bb}(r)|$ obtained by **(a)** simulations and **(b)** experiments, $\ln|rh_{bs}(r)|$ from **(c)** simulations and **(d)** experiments and $\ln|rh_{ss}(r)$ for **(e)** simulations and **(f)** experiments. The packing fraction η_b is increasing from top (blue) to bottom (red) for each case as labelled. The size ratio for the simulations is $q = 0.586$. The total packing fraction is fixed at $\eta_{\text{tot}} = 0.58$. For the experiments, the size ratio is $q = 0.648$ and $\eta_{\text{tot}} \approx 0.5$.

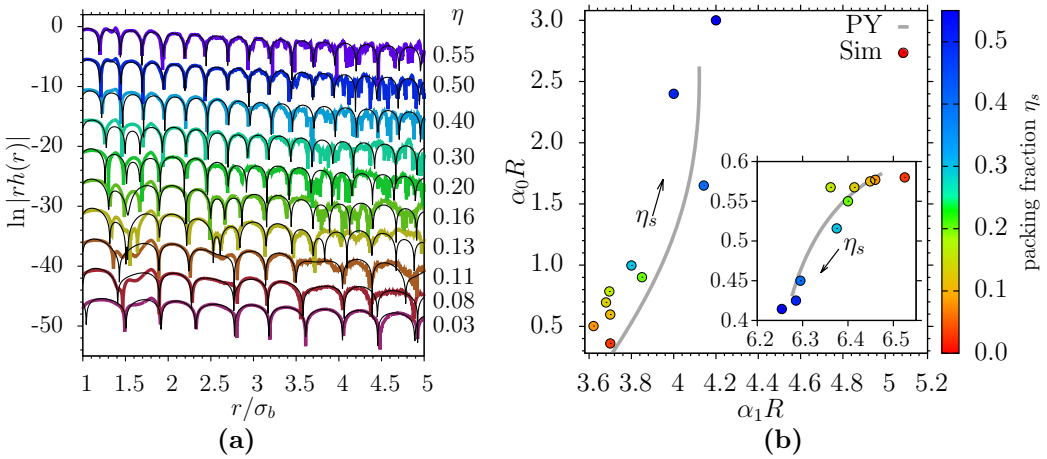

Figure 11.8: (a) Fits with functions of the form (11.18) for the $\ln|rh_{bs}(r)|$ from simulations with a size ratio $q = 0.586$. The total packing fraction is fixed at $\eta_{\text{tot}} = 0.58$ and η_s is varied from 0.03 (red) to 0.55 (blue). The obtained α_0', α_0'', α_1', and α_1'' values are shown in **(b)**. The grey line shows the PY approximation for the first pole π_1, the inset shows the second pole π_2. The colour indicates the packing fraction η_s from 0.03 (red) to 0.55 (blue).

of the large particles σ_b. As expected from the theory, this behaviour holds for all three different correlation functions.

The simulation data was fitted with functions of the form

$$rh(r) \sim |A'|e^{-\alpha_0' r}\cos\left(\alpha_1' r - \theta'\right) + |A''|e^{-\alpha_0'' r}\cos\left(\alpha_1'' r - \theta''\right) \tag{11.18}$$

and the values α_0', α_0'', α_1', and α_1'' are obtained. The fits are shown in figure 11.8 (a). A very good agreement can be achieved by the fits and the simulation data. The fits are performed in the region $1.8 < r/\sigma_b < 4.5$. In the region of the crossover, the fit with equation (11.18) does not exactly reproduce the behaviour near $r/\sigma_b \approx 1.5$. Since the function 11.18 is expected to be valid only for the long range oscillations, the deviation is not surprising. Figure 11.8 (b) shows a comparison of the values from the fits to the first pole (and the second pole in the inset) as calculated using the PY approximation. The results from the fits are close to the PY lines and the expected ordering of the poles with the amount of small particles can be seen. The fits with 8 parameters in total are numerically difficult and some deviations are expected. The obtained data shows, that the theory can be applied to the behaviour of the pair correlation function at moderate distances even if it is only valid in the long range limit.

To compare with [110], the radius of gyration of a network of size n^i

$$R_g^i = \sqrt{\frac{1}{n^i}\sum_{k=1}^{n^i}(\mathbf{x}_k^i - \mathbf{R}_0^i)^2} \quad , \tag{11.19}$$

is calculated, with $\mathbf{R}_0^i$ being the center of the network. Assuming there are N_C^i number of networks, one can calculate a weighted average of the radii of gyration

$$\langle R_g^i \rangle = \frac{1}{N}\sum_{m=1}^{N_C^i} n^i(m) R_g^i(m) \quad , \tag{11.20}$$

where N denotes the total number of particles i.

For the simulations, a VORONOI TESSELLATION [139, 140] of the network of small and large particles is performed. The Voronoi tessellation provides a list of neighbours for each particle in the sample. The experimental data has no periodic boundary conditions, therefore the edges were cutted (10 pixels in each dimension) after the Voronoi tessellation and the networks inside the sample are evaluated.

In the list of neighbours the clusters (in both networks of the big and small particles) need to be identified. For this purpose, we tested several cluster identification schemes, the DEPTH FIRST SEARCH [141], the DBSCAN algorithm [142], and a simple cutoff criterium with $r_{\text{cutoff}} = 1.5\sigma_i$ for each sub network. All methods yield the same results for the tested example configurations. Due to performance reasons we applied the depth first search for the analysis. The radius of gyration of each network is determined and the weighted average of the radii of gyration $\langle R_g^i \rangle$ is calculated and shown in figure 11.9 (a) for the simulations and 11.9 (b) for the experiments. Here, the averaged radius of gyration is divided by the box diagonal d. The system for the simulation was cubic, however, the experimentally measured volume is not. Here, each sample has a length of 512 pixel in x- and y-direction, whereas the z-direction is smaller and varies. Therefore, the box diagonal is more convenient for comparing the results. A percolating cluster which spans the system from one side to the other then has a radius of gyration of $\frac{1}{2\sqrt{3}} \approx 0.289$. In figure 11.9 is clearly visible, that a range of bicontinuous percolation occurs for both simulation and experiment. The crossover, however, is a single point at a certain value of η_b and may or may not coincidence with the range of bicontinuous percolation. For the parameters used in the simulation, the crossover is expected to be at $\eta_s = 0.141$ and $\eta_b = 0.439$. The experimental data is expected to show crossover at $\eta_s = 0.278$ and $\eta_b = 0.222$. The location of the crossover line in terms of η_b is marked in the graphs by a dashed line. For the simulations, this line is near to the point where the small particles stop to percolate. In the results of the experiments it is not clearly visible, however, it seems that

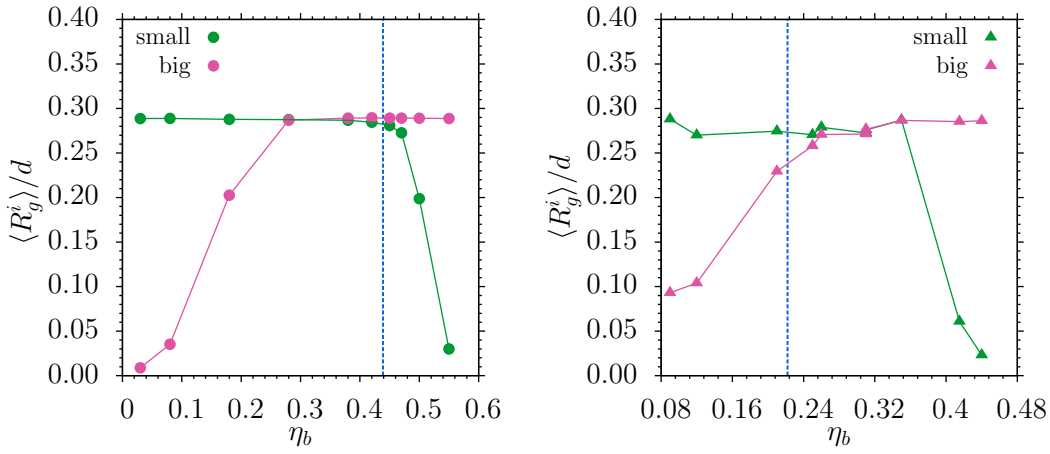

(a) **(b)**

Figure 11.9: The radius of gyration $\langle R_g^i \rangle$, obtained by a weighted average, divided by the box diagonal as a function of packing fraction η_b of the big particles. Results for **(a)** simulations and **(b)** experiments are shown. The dashed lines indicate the location of the crossover line.

the crossover occurs at the same value for η_b where the percolation for the bigger particles starts. This shows, that the crossover and the percolation in 3D cannot be related immediately. Further investigations of this question is needed to give an conclusive answer.

12 CONCLUSION AND OUTLOOK

We studied an important aspect of the structure of simple bulk liquids, namely the asymptotic decay of the correlation functions, for a one component case and a binary mixture of hard spheres. The theory of the asymptotic behaviour of the pair correlation function in three dimensions was tested in Monte Carlo simulations of a hard sphere fluid and experiments using colloidal particles.

For the investigation of a one-component liquid, pair correlation functions were measured in experiment and simulations . All pair correlation functions show oscillatory decay. We obtained values for the oscillation wavelength as well as for the decay length from fits. These values are in very good agreement to the one component theory results, which were computed using the PY approximation for the direct correlation functions.

We used two differently sized polymethylmethacrylate particles in experiment to perform measurements of the pair correlation function in dense liquids. In all pair correlation functions $g_{bb}(r), g_{bs}(r)$, and $g_{ss}(r)$ a clear manifestation of structural crossover can be seen, i. e. the wavelength of the oscillatory decay changes from approximately the diameter of the large particles to the diameter of the small particles if one increases the relative amount of small particles in the sample. In order to increase the quality of the experimental results, it would be helpful to improve the particle tracking algorithm. The particle tracking influences the obtained pair correlation functions directly. In addition, experiments with higher total packing fractions would lead to pair correlation functions which show more long range oscillations.

It would be desirable to perform simulations for the same size ratio q and total packing fractions as obtained from the experiments. This allows a direct comparison between theory, experiments and simulation. Nevertheless, the data from simulations allow a fit, the resulting poles can be compared to the PY theory, and a good agreement can be found. No investigation whether polydispersity or particle "softness" influences the crossover was made. In general, only hard spheres are considered in this thesis. For other pair potentials, it is of importance to find the direct correlation function in order to be able to calculate the poles. The determination of the direct correlation function in simulations remains challenging. Our simulations and experiments in 3D show clearly, that the theory for the long range asymptotic behaviour of pair correlation functions is also valid for intermediate ranges in the case of dense liquids.

The question whether the structural crossover in 3D between the two oscillatory wavelengths is related to the percolation of the neighbour networks cannot be answered satisfactorily. In any case, there occurs a range in η_b of bicontinuous percolation at the investigated total packing fractions, and the structural crossover is a single point, so there cannot be a direct relation between the

two phenomena in 3D. Further simulations for lower densities and smaller size ratios $q \approx 0.5$ could offer insights into the problem. The occurrence of a percolating cluster can be prevented by using lower total packing fractions, nevertheless, crossover may still be observed.

A

INTERFACE VELOCITY METHOD

The interface velocity method relies on linear fits to calculate a result for the coexistence pressure p_{coex}. The first linear fit is used to find the slopes of the volume change ΔV of the system as a function of MC cycles. Second, the slopes are fitted with a linear function to obtain the zero crossing point p_0 for each system size. The final step is a finite size extrapolation as a function of the lattice planes of the system sizes. All precise results of the fits mentioned above are dependent on the fit range. In the following, we attempt a systematic investigation on the influence of these linear fits.

The initial system contains liquid and solid connected by two interfaces which were equilibrated. Nevertheless, the system at the fixed pressure is not in equilibrium if one allows volume fluctuations and the system will evolve to a volume, which is different from the initial volume. For very long times the curves will reach a steady state with $\langle dV/dt \rangle \approx 0$ since the systems evolve towards equilibrium, as shown in figure A.1 (a). When the minority phase is already sufficiently small, the two interfaces start to interact, and ultimately the minority domain must disappear. Of course this late stage behaviour is of no concern for our purposes. For short times below $\approx 25 \cdot 10^3$ MC Steps as shown in figure A.1 (b), it becomes clear the volume change does follow a linear trend only in the first approximation. Hence, it is not obvious how to choose the fit range for extract-

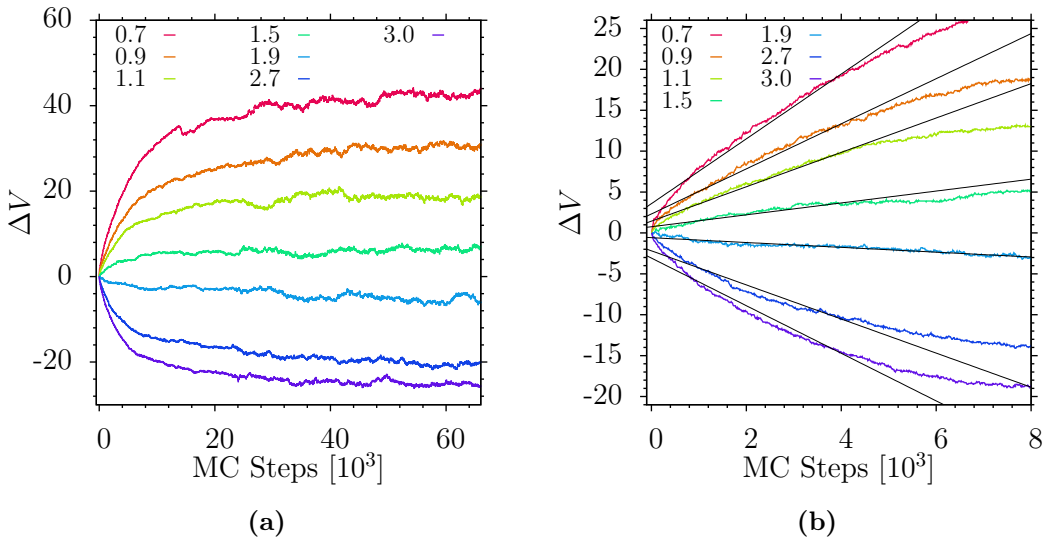

Figure A.1: (a) Volume change ΔV as a function of MC cycles of the softEffAO2 model. for different pressures as indicated. The system contains 15500 colloids, corresponding to $n = 10$ lattice planes in x- and y-direction. 120 independent runs were averaged. **(b)** Same plot as in (a) but with magnified axes. The solid lines are fits in the fit range $[0 : 5]$ from which $\langle dV/dt \rangle$ can be determined.

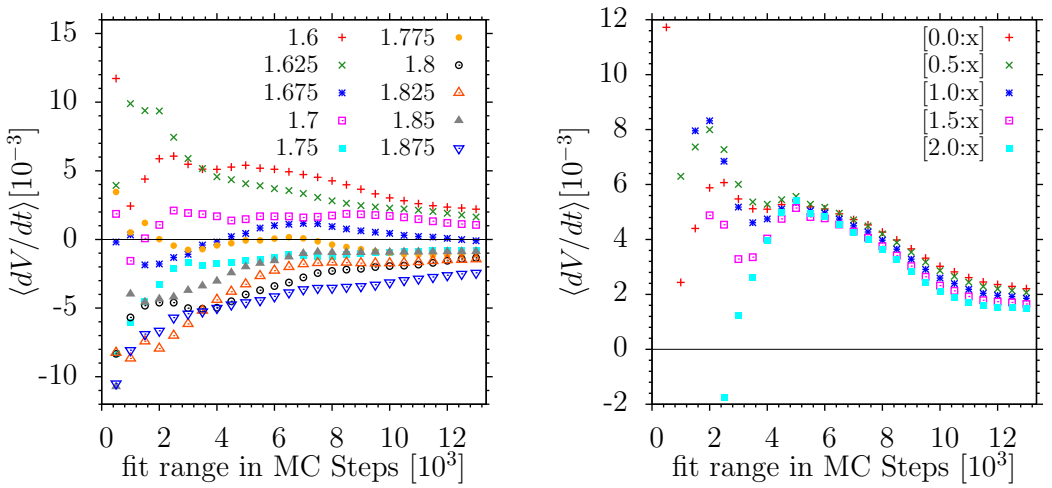

Figure A.2: (a) Value of the slope $\langle dV/dt \rangle$ as a function of the fit range, starting from 0. Various values for the pressure close to coexistence are shown, as indicated. The number of colloids is $N = 15500$ and $n = 10$. **(b)** Value of the slope $\langle dV/dt \rangle$ for the pressure $p = 1.6$ for different starting points of the fit range as indicated.

ing the slopes $\langle dV/dt \rangle$. We are mainly interested in the point where the slope is zero, so the onset will be close to zero and the curve will be linear.

To investigate the influence of the fit range, all system sizes and pressures were fitted in various different ranges as shown in figure A.2. Fit ranges are given in the notation $[x : y]$ where x- is the lower bound for the range and y- represents the upper bound. For pressures close to the coexistence value p_{coex}, one expects a very weak dependence of the slope $\langle dV/dt \rangle$ on the fitting range. Figure A.2 (a) shows the value of the slope for different pressure values close to p_{coex} for the largest system size containing $N = 15500$ colloids. For small fitting ranges the slope scatters significantly and for very large fitting ranges all slopes are approaching $\langle dV/dt \rangle \to 0$ since the system is evolving into a steady state for large enough MC steps, as shown in figure A.1 (a) for MC Steps $> 15 \cdot 10^3$. Unfortunately, there is no range where the slope value is constant, hence independent of the fit range, for all pressures. In figure A.1 (b) only $p = 1.6$ is shown, where the starting point of the fit range is varied as well. Below a fit range of $[x : 4]$ the slopes differ and a substantial difference between the different starting points can be seen. Above $\approx [x : 4]$, this difference vanishes and all fits are resulting in a very similar slope. For pressure values closer to the coexistence, the slope is lower and the difference between different starting points will reduce further. Resulting, fit ranges larger than $[x : 4]$ are chosen to minimize the ambiguity from the starting point.

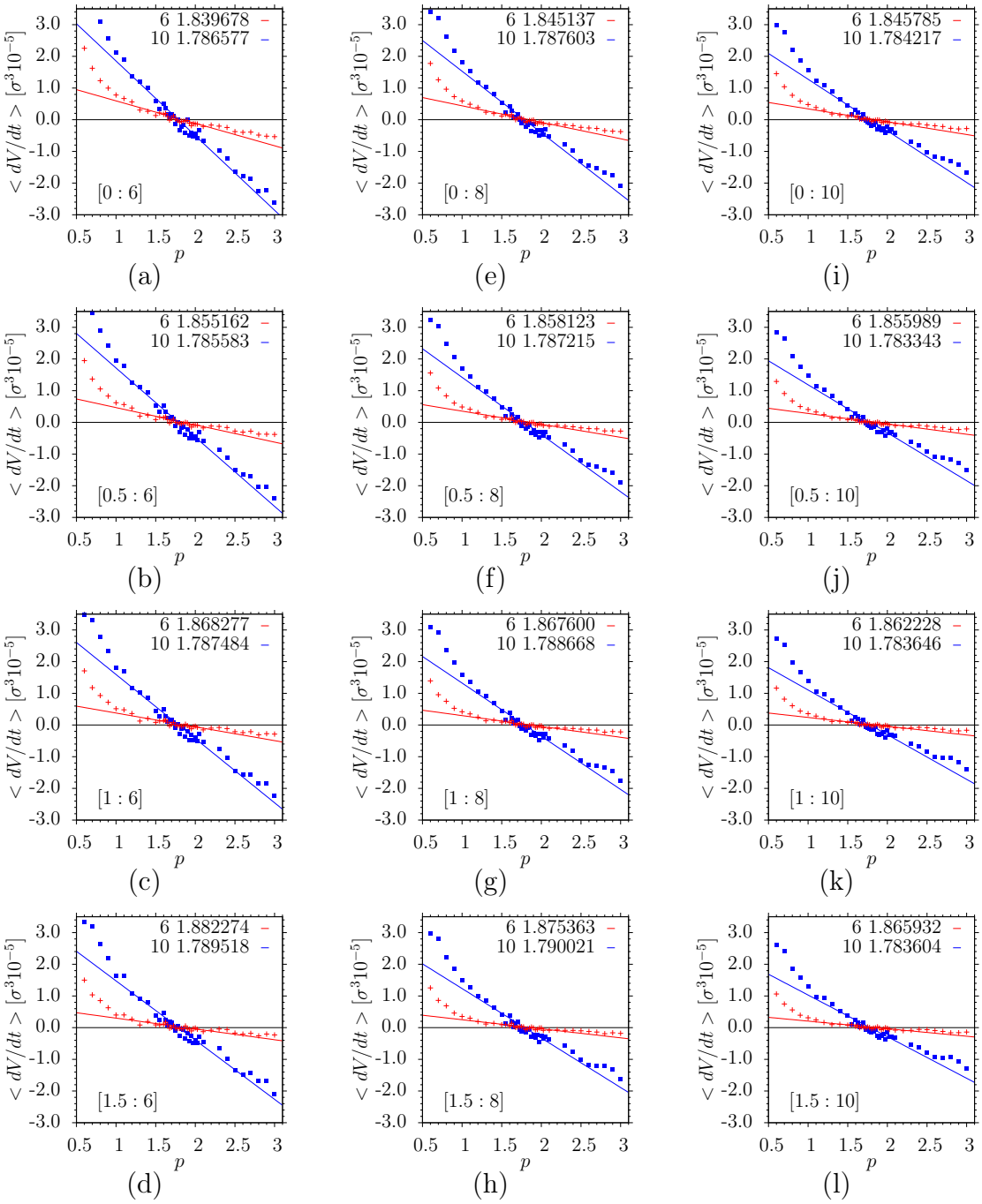

Figure A.3: Slopes as a function of pressure for the softEffA02 model of the smallest ($n = 6$) and the largest system size ($n = 10$). The fit ranges are varied from $0, 0.5, 1, 1.5$ for the starting point and $6, 8, 10$ for the end point. Resulting zero crossing points are indicated.

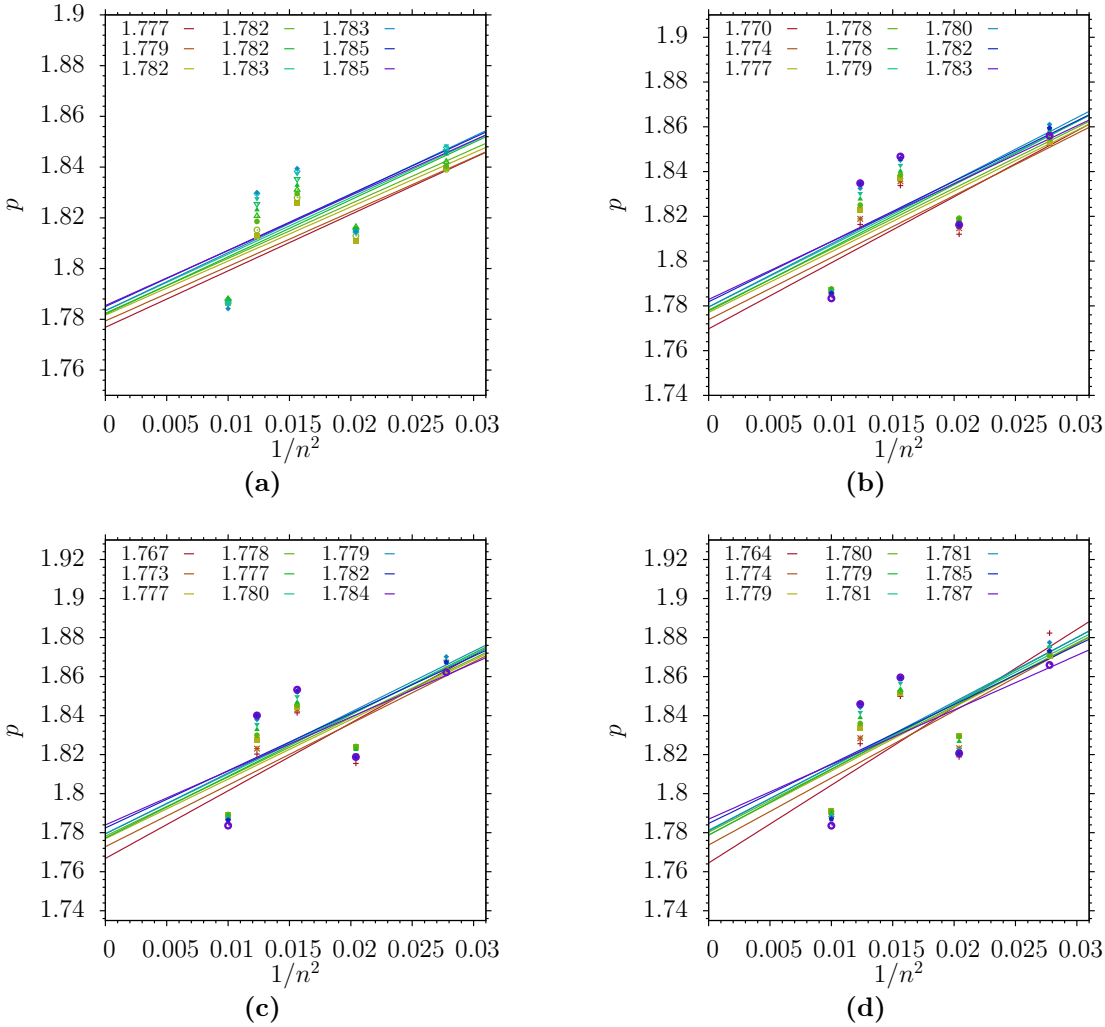

Figure A.4: **(a)** Coexistence pressure as a function of the system size $1/n^2$ for different fitting ranges from $[0:6]$ (dark red) to $[0:10]$ (blue). The resulting values for p_{coex} are given in the legend. **(b)** Same plot as in (a) but with fitting ranges from $[0.5:6]$ to $[0.5:10]$. **(c)** Same data with fitting ranges $[1.0:x]$ and **(d)** with $[1.5:x]$

The next step is to estimate the zero crossing point for the obtained values for the slopes. Figure A.3 shows the slopes of ΔV as a function of the pressure for various different fit ranges as indicated in each figure. Only the largest and smallest system size is shown for clarity. As shown, the slopes follow a linear function for pressures larger than ≈ 1.0 and smaller than ≈ 2.5 and differ significantly from the straight fit outside these values in all cases. Since the fits are used to obtain the zero crossing points p_0, it is not necessary to describe the functional dependency of the slope as a function of the pressure. Therefore, pressures in the range of $[1.0:2.5]$ were used to obtain p_0 for all system sizes and fit ranges. In general, this fit range represents an additional degree of freedom and changing it will influence the results.

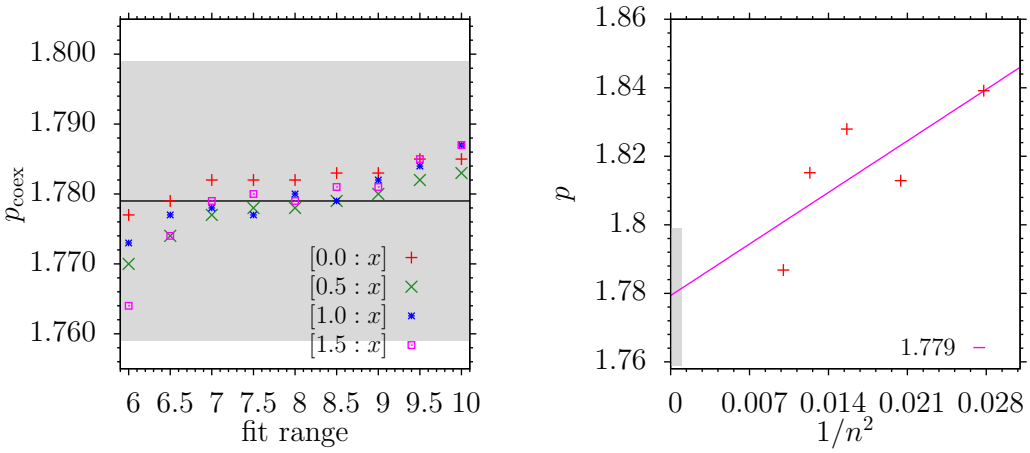

(a) **(b)**

Figure A.5: (a) Value for the coexistence pressure p_{coex} as a function of the fit range for 4 different starting points. The grey shaded area is the estimated uncertainty of ± 0.02 and the horizontal black line indicates the result for p_{coex}. **(b)** Picked result for the final determination of $p_{\text{coex}} = 1.779$. The fit of the slopes was performed in a range of $[0 : 6.5]$. The grey rectangle indicates the errorbar of ± 0.02 on the result.

The values of p_0 are shown as a function of the squared number of lattice planes n^2 in x- and y-direction in figure A.4. The coexistence value for the pressure p_{coex} is given by the extrapolation $1/n^2 \to 0$. The resulting linear fits and values for p_{coex} are shown in figure A.4(a)-(d) for different fitting ranges. In each case, all system sizes are used for the extrapolation. The results for p_{coex} as a function of the fit range is shown in figure A.5 (a). As visible, there is a small trend in the results. The coexistence pressure becomes slightly larger for larger fitting ranges. Additionally, increasing the fit range beginning results in a larger variance of the results. The smallest value is $p_{\text{coex}} = 1.764$ and the largest one $p_{\text{coex}} = 1.791$ for a fit range of $[1.5 : x]$. This gives a upper bound for the error estimation of the coexistence pressure. As final result we picked the range $[0 : 6.5]$, since the variance in the results is lower for the fit ranges starting from 0. The value for the coexistence pressure $p_{\text{coex}} = 1.779$ is in the middle of the obtained values. The uncertainty in the result is shown in figure A.5(a) and (b) as shaded grey area. Since the systematic errors are not completely investigated and the influence is unclear, the error was estimated to be ± 0.02.

As a general result, the interface velocity method suffers from several problems. One ambiguity is the choice of the fitting ranges for the three consecutive fits which needs to be made. This limits the accuracy of the result. Additionally, the influence of the possible artificial strain in the crystal is unclear. To investigate the systematic error introduced by the fixed x- and y-directions further

simulations are necessary. Since the systematic errors of this method are not fully understood, we have larger large errorbars in our final results, as explained above, in order to take precautions.

B PERCUS-YEVICK APPROXIMATION

ONE COMPONENT LIQUID

In statistical mechanics the PERCUS-YEVICK approximation (PY) [116, 143] is a closure relation to solve the ORNSTEIN-ZERNIKE equation (OZ) for hard spheres. It is also referred to as the PY equation. It is commonly used in fluid theory to obtain e.g. expressions for the radial distribution function. The direct correlation function represents the direct correlation between two particles in a system containing $N-2$ other particles. It can be represented by

$$c(r) = g_{total}(r) - g_{indirect}(r) \quad , \tag{B.1}$$

where $g_{total}(r)$ is the radial distribution function, i.e. $g(r) = \exp[-\beta w(r)]$ (with $w(r)$ the potential of mean force) and $g_{indirect}(r)$ is the radial distribution function without the direct interaction between pairs $u(r)$ included; i.e. we write $g_{indirect}(r) = \exp^{-\beta[w(r)-u(r)]}$. Thus we approximate $c(r)$ by

$$c(r) = e^{-\beta w(r)} - e^{-\beta[w(r)-u(r)]} \quad . \tag{B.2}$$

If we introduce the function $y(r) = e^{\beta u(r)} g(r)$ into the approximation for $c(r)$ one obtains

$$c(r) = g(r) - y(r) = e^{-\beta u} y(r) - y(r) = f(r) y(r) \quad . \tag{B.3}$$

This is the essence of the PERCUS-YEVICK approximation. If we substitute this result in the ORNSTEIN–ZERNIKE equation, one obtains the PY equation:

$$y(r_{12}) = 1 + \rho \int f(r_{13}) y(r_{13}) h(r_{23}) dr_3 \quad . \tag{B.4}$$

The approximation was defined by PERCUS and YEVICK in 1958. For hard spheres, the equation has an analytical solution. The exact solution for the PY integral equation for the hard sphere model was derived by WERTHEIM in 1963 [144, 121]. The direct correlation function is given by

$$C(r/R) = -\frac{(1+2\eta)^2 - 6\eta(1+1/2\eta)^2 (r/R) + \eta(1+2\eta)^2 1/2 (r/R)^3}{(1-\eta)^4} \quad , \tag{B.5}$$

and the equation of state is given by

$$\beta \frac{p}{\rho} = \frac{1+\eta+\eta^2}{(1-\eta)^3} \quad . \tag{B.6}$$

The static bulk structure factor $S(\mathbf{q})$ in Fourier space is of special importance, as it is directly measurable in experiments using neutron scattering, thus establishes the link between experiments an theory for the equilibrium structure of bulk liquids.

The structure factor is the auto-correlation function of the Fourier transform of the density $\rho(\mathbf{q})$

$$S(\mathbf{q}) = \frac{1}{N}\langle\rho(\mathbf{q})\rho(-\mathbf{q})\rangle \quad , \tag{B.7}$$

with

$$\rho(\mathbf{q}) = \int \rho(\mathbf{r})e^{-i\mathbf{q}\cdot\mathbf{r}}\mathrm{d}\mathbf{r} \quad . \tag{B.8}$$

For homogeneous fluids one can show that [87]

$$S(q) = 1 + \rho h(q) \tag{B.9}$$

holds. In general, the Fourier transform $\hat{f}(\mathbf{q})$ of a function $f(\mathbf{r})$ is given by

$$\hat{f}(\mathbf{q}) = \int f(\mathbf{r})e^{-i\mathbf{q}\cdot\mathbf{r}}\mathrm{d}\mathbf{r} \quad \text{and} \quad f(\mathbf{r}) = \frac{1}{2\pi^3}\int \hat{f}(\mathbf{q})e^{i\mathbf{q}\cdot\mathbf{r}}\mathrm{d}\mathbf{q} \quad , \tag{B.10}$$

and if one assumes spherical symmetry, this relation simplifies to

$$\hat{f}(q) = 4\pi\int_0^\infty f(r)r\frac{\sin(qr)}{q}\mathrm{d}r \quad \text{and} \quad f(r) = \frac{1}{2\pi^2}\int_0^\infty \hat{f}(q)q\frac{\sin(qr)}{r}\mathrm{d}q \quad . \tag{B.11}$$

MIXTURE OF SIMPLE LIQUIDS

The direct correlation functions for a two component mixture was calculated by LEBOWITZ in 1964 [123]. In the following, the larger particles with diameter σ_b are labelled with index b and the small with diameter σ_s as s. The size ratio is given by $q = \sigma_s/\sigma_b$.

$$-c_{ss}(r) = a_1 + b_1 r + dr^3 \qquad \text{for } r < \sigma_s \tag{B.12}$$

$$-c_{bb}(r) = a_2 + b_2 r + dr^3 \qquad \text{for } r < \sigma_b \tag{B.13}$$

and $-c_{ss}(r) = 0$ for $r > \sigma_s$, as well as $-c_{bb}(r) = 0$ for $r > \sigma_b$, and

$$-c_{bs}(r) = \begin{cases} a_1 & \text{for } r < \lambda \\ a_1 + \frac{1}{r}(bR^2 + 4d\lambda R^3 + dR^4) & \text{for } \lambda \leq r < \frac{1}{2}(\sigma_b + \sigma_s) \\ 0 & \text{for } r \geq \frac{1}{2}(\sigma_b + \sigma_s) \end{cases} \tag{B.14}$$

with $R = r - \lambda$ and $\lambda = 1/2(\sigma_b - \sigma_s)$. The coefficients a_1 and a_2 are given by

$$a_1 = \frac{\partial}{\partial \eta_s}\beta\rho' \qquad \text{and} \qquad a_2 = \frac{\partial}{\partial \eta_b}\beta\rho' \quad , \tag{B.15}$$

where $\beta\rho'$ is the reduced function

$$\beta\rho' = \frac{(\eta_s + \alpha^3\eta_b)(1 + \eta + \eta^2) - 3\eta_s\eta_b(1-\alpha)^2(1 + \eta_s + \alpha(1 + \eta_b))}{(1-\eta)^3} \quad . \tag{B.16}$$

The other coefficients are given by

$$d = \frac{1}{2\sigma_s^3}(\eta_s a_1 + \alpha^3\eta_b a_2) \quad , \tag{B.17}$$

$$b_1 = -\frac{6}{\sigma_s}(\eta_s w_{ss}^2 + \frac{1}{4}\eta_b(1+\alpha)^2\alpha w_{bs}^2) \quad , \tag{B.18}$$

$$b_2 = -\frac{6}{\sigma_b}(\eta_b w_{bb}^2 + \frac{1}{4}\eta_s(1+\alpha)^2\alpha^{-3} w_{bs}^2) \quad , \quad \text{and} \tag{B.19}$$

$$b = -\frac{3(1+\alpha)}{\sigma_b}(\alpha^{-2}\eta_s w_{ss} + \eta_b w_{bb}) w_{bs} \quad . \tag{B.20}$$

The functions w_{ij} are defined as

$$w_{ss} = \frac{(1 + 1/2\eta) + 3/2\eta_b(\alpha - 1)}{(1-\eta)^2} \quad , \tag{B.21}$$

$$w_{bb} = \frac{(1 + 1/2\eta) + 3/2\eta_s(1/\alpha - 1)}{(1-\eta)^2} \quad , \quad \text{and} \tag{B.22}$$

$$w_{bs} = \frac{(1 + 1/2\eta) + 3/2\eta_b\frac{1-\alpha}{1+\alpha}(\eta_b - \eta_s)}{(1-\eta)^2} \quad . \tag{B.23}$$

The resulting direct correlation functions $c_{bb}(r)$, $c_{ss}(r)$ and $c_{bs}(r)$ are shown in figure B.1 (a). The static structure factors $S_{bb}(q), S_{ss}(q)$ and $S_{bs}(q)$ for an isotropic mixture are defined by

$$S_{ij}(q) = (N_i N_j)^{-1/2}\langle \sum_{m,n} e^{-iq(\mathbf{r}_n^i - \mathbf{r}_m^j)} \rangle - (N_i N_j)^{1/2}\delta_{q,0} \tag{B.24}$$

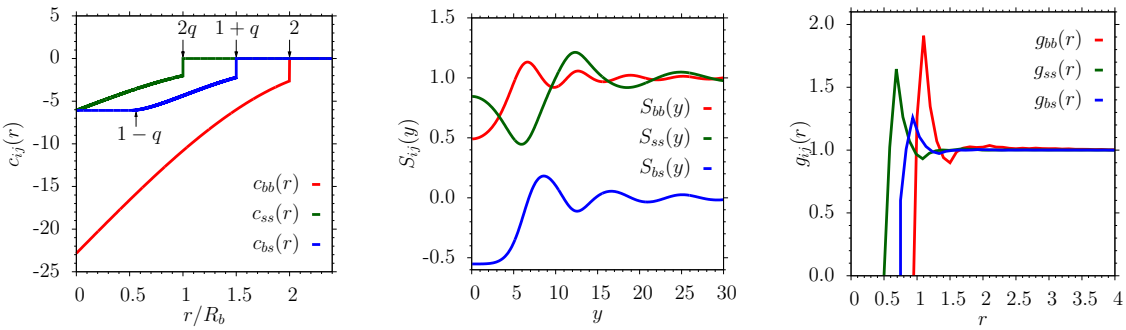

(a) **(b)** **(c)**

Figure B.1: (a) Direct correlation functions $c_{bb}(r)$, $c_{ss}(r)$ and $c_{bs}(r)$ as given by equation (B.12)-(B.14) in a hard sphere mixture given by the PY approximation. The packing fractions are $\eta_s = 0.15$ and $\eta_b = 0.13$ and the size ratio is $q = 0.5$. The arrows indicate the discontinuities of the correlation functions and R_b is the radius of the large spheres. Outside of the particle diameter the correlation function is zero. **(b)** Structure factors as calculated from equation (B.25)–(B.27), with $y = q \cdot 2R_b$ being the Fourier space variable. **(c)** Resulting pair correlation functions from Fourier transforms of (b). Note that the quality of the functions is limited due to a finite amount of used y values for the Fourier transform.

in Fourier space. We follow [145] for calculating the structure factor from the Fourier transform of the direct correlation functions for binary mixtures

$$S_{ss}(y) = \{1 - n_s\hat{c}_{ss}(y) - n_b n_s C_{bs}^2(y)/\left[1 - n_b\hat{c}_{bb}(y)\right]\}^{-1} \quad , \tag{B.25}$$

$$S_{bb}(y) = \{1 - n_b\hat{c}_{bb}(y) - n_b n_s C_{bs}^2(y)/\left[1 - n_s\hat{c}_{ss}(y)\right]\}^{-1} \quad , \tag{B.26}$$

$$S_{bs}(y) = (n_b n_s)^{1/2}\hat{c}_{bs}(y)\{\left[1 - n_b\hat{c}_{bb}(y)\right]\left[1 - n_s\hat{c}_{ss}(y)\right] - n_b n_s\hat{c}_{bs}^2(y)\}^{-1} \quad , \tag{B.27}$$

where $y = q\sigma_b$ is a scaled Fourier space variable. The n_i represent the respective number densities and $\hat{c}_{ss}, \hat{c}_{bb}$ and $\hat{c}_{bs}$ are the Fourier transforms of the direct correlation functions. The pair correlation functions $g_{ij}(r)$ are related to the static structure factors by inverse Fourier transforms analogous to the one component case. Exemplary results are shown in figure B.1 (c).

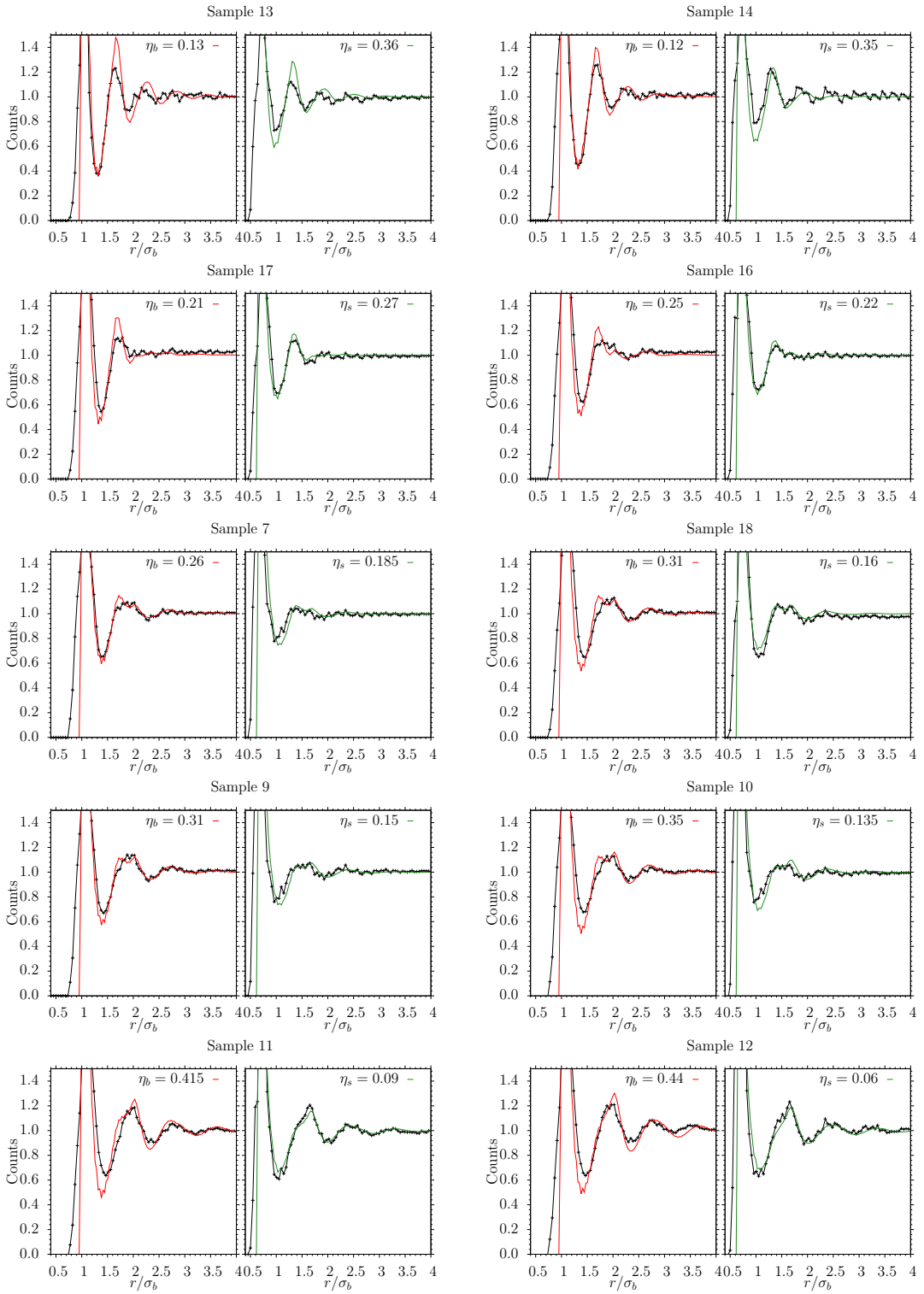

Figure C.1: Fits of Fourier transforms (lines) for the determination of the packing fractions η_s and η_b from experimental data (points) for the used Samples from top to bottom (from low values to high values of η_b), as labelled.

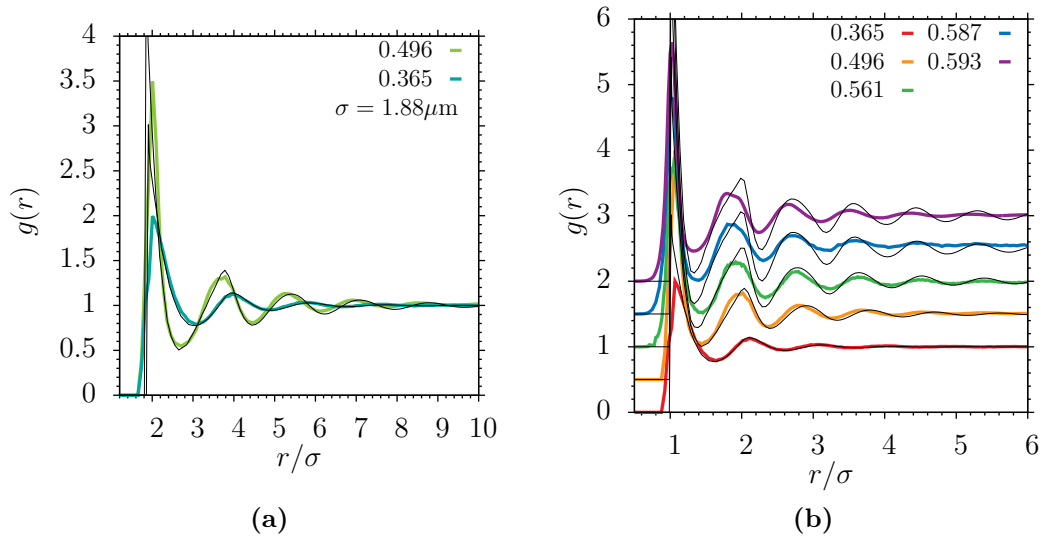

(a) **(b)**

Figure C.2: **(a)** Fit for the small colloids dyed with coumarin for two different packing fractions as indicated. The size is estimated to be 1.88 µm. **(b)** Vertically shifted pair correlation functions $g(r)$ for a one component liquid. Fits of Fourier transforms of the structure factor given by the PY approximation for the determination of the packing fraction η from experiments are shown as black lines. The results are indicated.

Table C.1: Average number of particles N_b, N_s and standard deviations σ_b, σ_s in the used experimental samples. The numbering is consistent with figure C.1.

SAMPLE	N_b	σ_b	N_s	σ_s	# IMAGES
Sample 13	2281	49	76935	239	11
Sample 14	2684	146	67160	858	12
Sample 17	5547	259	40449	1219	14
Sample 16	12936	599	34857	2500	10
Sample 7	7908	190	21179	625	19
Sample 18	12044	104	16445	420	14
Sample 9	28559	2536	36910	2122	7
Sample 10	19572	823	26750	3460	9
Sample 11	17928	734	5636	374	11
Sample 12	18533	978	3455	741	11

BIBLIOGRAPHY

[1] Kelton, K. F. & (Eds.), A. L. G. *Nucleation* (Pergamon, Oxford, 2009). (Cited on pages 1 and 39.)

[2] Nucleation (A. C. Zettlemoyer (Ed.) M. Dekker, New York, 1969). (Cited on pages 1 and 39.)

[3] Volmer, M. & Weber, A. Keimbildung in übersättigten Gebilden. *Zeitschrift für Physikalische Chemie* **119**, 277–301 (1926). (Cited on page 1.)

[4] Nucleation: Basic Theory with Applications (D. Kashchiev (Ed.), Butterworth-Heinemann, Oxford, 2000). (Cited on pages 1, 39, and 40.)

[5] Palberg, T. Crystallization kinetics of colloidal model suspensions: recent achievements and new perspectives. *Journal of Physics: Condensed Matter* **26**, 333101 (2014). (Cited on pages 1, 39, and 82.)

[6] Auer, S. & Frenkel, D. Prediction of absolute crystal-nucleation rate in hard-sphere colloids. *Nature* **409**, 1020–1023 (2001). (Cited on pages 1 and 79.)

[7] Filion, L., Ni, R., Frenkel, D. & Dijkstra, M. Simulation of nucleation in almost hard-sphere colloids: The discrepancy between experiment and simulation persists. *Journal of Chemical Physics* **134**, 134901 (2011).

[8] Schilling, T. *et al.* Mixtures of anisotropic and spherical colloids: Phase behavior, confinement, percolation phenomena and kinetics. *The European Physical Journal Special Topics* **222**, 3039–3052 (2013). (Cited on page 1.)

[9] Langer, J. Theory of the condensation point. *Annals of Physics* **41**, 108–157 (1967). (Cited on page 1.)

[10] Binder, K. & Stauffer, D. Statistical theory of nucleation, condensation and coagulation. *Advances in Physics* **25**, 343–396 (1976). (Cited on pages 1 and 39.)

[11] Binder, K. Theory of first-order phase transitions. *Reports on progress in physics* **50**, 783 (1987). (Cited on page 1.)

[12] Radu, M. & Schilling, T. Solvent hydrodynamics speed up crystal nucleation in suspensions of hard spheres. *Europhysics Letters* **105**, 26001 (2014). (Cited on pages 1, 39, 79, and 82.)

[13] van Blaaderen, A. Quantitative real-space analysis of colloidal structures and dynamics with confocal scanning light microscopy. In Palberg, T. & Ballauff, M. (eds.) *Optical Methods and Physics of Colloidal Dispersions*,

vol. 104 of *Progress in Colloid and Polymer Science*, 59–65 (Springer Berlin/Heidelberg, 1997). (Cited on page 2.)

[14] Pusey, P. N. & van Megen, W. Phase behaviour of concentrated suspensions of nearly hard colloidal spheres. *Nature* **320**, 340–342 (1986). (Cited on pages 2, 79, 82, and 89.)

[15] Landau, D. P. & Binder, K. *A Guide to Monte-Carlo Simulations in Statistical Physics* (Cambridge University Press, New York, 3rd ed., 2009). (Cited on pages 8, 10, 14, and 57.)

[16] Gentle, J. E. *Random number generation and Monte Carlo methods, page 217* (Springer Science & Business Media, 2003). (Cited on page 9.)

[17] Metropolis, N., Rosenbluth, A. W., Rosenbluth, M. N., Teller, A. H. & Teller, E. Equation of State Calculations by Fast Computing Machines. *Journal of Chemical Physics* **21** (1953). (Cited on page 10.)

[18] Frenkel, D. & Smit, B. *Understanding Molecular Simulation* (Academic Press, London, 2002). (Cited on pages 11 and 19.)

[19] Deb, D., Winkler, A., Virnau, P. & Binder, K. Simulation of fluid-solid coexistence in finite volumes: A method to study the properties of wall-attached crystalline nuclei. *Journal of Chemical Physics* **136**, 134710 (2012). (Cited on pages 12, 17, and 42.)

[20] Widom, B. Some Topics in the Theory of Fluids. *Journal of Chemical Physics* **39**, 2808–2812 (1963). (Cited on page 12.)

[21] Widom, B. Structure of Interfaces from Uniformity of the chemical potential. *Journal of Statistical Physics* **19**, 563–574 (1978). (Cited on page 12.)

[22] MacDowell, L. G., Shen, V. K. & Errington, J. R. Nucleation and cavitation of spherical, cylindrical, and slablike droplets and bubbles in small systems. *Journal of Chemical Physics* **125** (2006). (Cited on page 16.)

[23] Barber, M. & Green M.S. (Ed.), Phase transitions and critical phenomena. vol. 8, 145 (Academic Press, London, 1983). (Cited on page 18.)

[24] Fisher, M. E. & Green M.S. (Ed.) , in Critical Phenomena (Academic Press, London, 1971). (Cited on page 18.)

[25] Poon, W. C. K. The physics of a model colloid–polymer mixture. *Journal of Physics: Condensed Matter* **14**, R859–R880 (2002). (Cited on pages 23 and 26.)

[26] Ilett, S. M., Orrock, A., Poon, W. & Pusey, P. Phase behavior of a model colloid-polymer mixture. *Physical Review E* **51**, 1344–1352 (1995). (Cited on page 23.)

[27] Binder, K., Virnau, P. & Statt, A. Perspective: The Asakura Oosawa model: A colloid prototype for bulk and interfacial phase behavior. *Journal of Chemical Physics* (2014). (Cited on page 23.)

[28] Binder, K., Horbach, J., Vink, R. & De Virgiliis, A. Confinement effects on phase behavior of soft matter systems. *Soft Matter* **4**, 1555–1568 (2008).

[29] Horbach, J. & Vink, R. L. Grand canonical Monte Carlo simulation of a model colloid-polymer mixture: Coexistence line, critical behavior, and interfacial tension. *Journal of Chemical Physics* **121** (2004). (Cited on page 23.)

[30] Asakura, S. & Oosawa, F. Interaction between particles suspended in solutions of macromolecules. *Journal of Polymer Science* **33**, 183–192 (1958). (Cited on page 23.)

[31] Oosawa, F. & Asakura, S. Surface Tension Of High-polymer Solutions. *Journal of Chemical Physics* **22**, 1255 (1954). (Cited on page 23.)

[32] Vrij, A. Polymers at Interfaces and the Interactions in Colloidal Dispersions. *Pure Appl. Chem.* **48**, 471–483 (1976). (Cited on pages 23 and 24.)

[33] Aarts, D., Tuinier, R. & Lekkerkerker, H. Phase behaviour of mixtures of colloidal spheres and excluded-volume polymer chains. *Journal of Physics: Condensed Matter* **14**, 7551 (2002). (Cited on page 25.)

[34] Lekkerkerker, H. N. W., Poon, W. C.-K., Pusey, P. N., Stroobants, A. & Warren, P. B. Phase Behaviour of Colloid + Polymer Mixtures. *Europhysics Letters* **20**, 559 (1992). (Cited on pages 25 and 26.)

[35] Dijkstra, M., Brader, J. M. & Evans, R. Phase behaviour and structure of model colloid-polymer mixtures. *Journal of Physics: Condensed Matter* **11**, 10079 (1999). (Cited on page 25.)

[36] Gast, A., Hall, C. & Russel, W. Polymer-induced Phase Separations In Non-aqueous Colloidal Suspensions. *Journal of Colloid Interface Science* **96**, 251–267 (1983). (Cited on page 25.)

[37] Dijkstra, M., van Roij, R., Roth, R. & Fortini, A. Effect of many-body interactions on the bulk and interfacial phase behavior of a model colloid-polymer mixture. *Physical Review E* **73**, 041404 (2006). (Cited on page 26.)

[38] Brader, J. M., Evans, R. & Schmidt, M. Statistical mechanics of inhomogeneous model colloid-polymer mixtures. *Molecular Physics* **101**, 3349–3384 (2003). (Cited on page 26.)

[39] Colloids and the Depletion Interaction (H. N. W. Lekkerkerker and R. Tuinier (Eds.), Springer, Berlin, 2011). (Cited on page 26.)

[40] Poon, W. C. K., Weeks, E. R. & Royall, C. P. On measuring colloidal volume fractions. *Soft Matter* **8**, 21–30 (2012). (Cited on pages 27, 92, and 100.)

[41] Royall, C. P., Poon, W. C. K. & Weeks, E. R. In search of colloidal hard spheres. *Soft Matter* **9**, 17–27 (2013). (Cited on pages 27 and 92.)

[42] Zykova-Timan, T., Horbach, J. & Binder, K. Monte Carlo simulations of the solid-liquid transition in hard spheres and colloid-polymer mixtures. *Journal of Chemical Physics* **133**, 014705 (2010). (Cited on pages 31, 49, 50, 51, 52, 54, 56, 70, and 90.)

[43] Steinhardt, P. J., Nelson, D. R. & Ronchetti, M. Bond-orientational order in liquids and glasses. *Physical Review B* **28**, 784–805 (1983). (Cited on page 32.)

[44] Lechner, W. & Dellago, C. Accurate determination of crystal structures based on averaged local bond order parameters. *Journal of Chemical Physics* **129**, 114707 (2008). (Cited on page 33.)

[45] Mickel, W., Kapfer, S. C., Schröder-Turk, G. E. & Mecke, K. Shortcomings of the bond orientational order parameters for the analysis of disordered particulate matter. *Journal of Chemical Physics* **138** (2013). (Cited on page 36.)

[46] Balibar, S. & Caupin, F. *Comptes Rendus Physique* **988** (2006). (Cited on page 39.)

[47] Schmitz, F., Virnau, P. & Binder, K. Monte Carlo tests of nucleation concepts in the lattice gas model. *Physical Review E* **87**, 053302 (2013). (Cited on pages 39 and 45.)

[48] Binder, K. & Stauffer, D. Monte Carlo study of the surface area of liquid droplets. *Journal of Statistical Physics* **6**, 49–59 (1972). (Cited on page 39.)

[49] Rowlinson, J. S. & Widom, B. *Molecular theory of capillarity* (Courier Dover Publications, 2013). (Cited on page 39.)

[50] Viisanen, Y., Strey, R. & Reiss, H. Homogeneous nucleation rates for water. *Journal of Chemical Physics* **99**, 4680–4692 (1993). (Cited on page 39.)

[51] Fladerer, A. & Strey, R. Homogeneous nucleation and droplet growth in supersaturated argon vapor: The cryogenic nucleation pulse chamber. *Journal of Chemical Physics* **124**, 164710 (2006).

[52] Iland, K., Wölk, J., Strey, R. & Kashchiev, D. Argon nucleation in a cryogenic nucleation pulse chamber. *Journal of Chemical Physics* **127**, 154506 (2007). (Cited on page 39.)

[53] Schätzel, K. & Ackerson, B. J. Density fluctuations during crystallization of colloids. *Physical Review E* **48**, 3766–3777 (1993). (Cited on page 39.)

[54] He, Y., Ackerson, B. J., van Megen, W., Underwood, S. M. & Schätzel, K. Dynamics of crystallization in hard-sphere suspensions. *Physical Review E* **54**, 5286–5297 (1996).

[55] Harland, J. L. & van Megen, W. Crystallization kinetics of suspensions of hard colloidal spheres. *Physical Review E* **55**, 3054–3067 (1997).

[56] Gasser, U., Weeks, E. R., Schofield, A., Pusey, P. & Weitz, D. Real-space imaging of nucleation and growth in colloidal crystallization. *Science* **292**, 258–262 (2001).

[57] Wette, P., Schöpe, H. J. & Palberg, T. Microscopic investigations of homogeneous nucleation in charged sphere suspensions. *Journal of Chemical Physics* **123**, 174902 (2005).

[58] Schall, P., Cohen, I., Weitz, D. A. & Spaepen, F. Visualizing dislocation nucleation by indenting colloidal crystals. *Nature* **440**, 319–323 (2006).

[59] Iacopini, S., Palberg, T. & Schöpe, H. J. Ripening-dominated crystallization in polydisperse hard-sphere-like colloids. *Physical Review E* **79**, 010601 (2009).

[60] Herlach, D. M., Klassen, I., Wette, P. & Holland-Moritz, D. Colloids as model systems for metals and alloys: a case study of crystallization. *Journal of Physics: Condensed Matter* **22**, 153101 (2010). (Cited on pages 39 and 82.)

[61] Gutzow, I. & Schmelzer, J. *The Vitreous State: Thermodynamics, Structure, Rheology, and Crystallization* (Springer, Berlin, 1995). (Cited on pages 39 and 82.)

[62] Herlach, D. M., Galenko, P. & Holland-Moritz, D. *Metastable Solids from Undercooled Melts* (Pergamon, Oxford, 2007). (Cited on page 39.)

[63] H. Emmerich, G. W., P. Virnau & Spatschek, R. Heterogeneous Nucleation and Microstructure Formation: Steps Towards a System and Scale Bridging Understanding. *EPJ* **223** (2014). (Cited on pages 79 and 82.)

[64] Müller-Krumbhaar, H., Kurz, W. & Brener, E. Phase Transformations in Materials, p. 81 (Wiley-VCH, Weinheim, 2001). (Cited on pages 40 and 82.)

[65] Turnbull, D. Formation of Crystal Nuclei in Liquid Metals. *Journal of Applied Physics* **21**, 1022–1028 (1950).

[66] Burke, J. & Turnbull, D. Recrystallization and grain growth. *Progress in metal physics* **3**, 220–292 (1952).

[67] Biloni, H. Physical Metallurgy, p. 477 (North-Holland, Amsterdam, 1983).

[68] Boettinger, W. *et al.* Solidification microstructures: recent developments, future directions. *Acta materialia* **48**, 43–70 (2000). (Cited on page 39.)

[69] Tiller, W. A. (ed.) *The Science of Crystallization: Microscopic Interfacial Phenomena* (Cambridge Univ. Press, New York, 1991). (Cited on page 40.)

[70] Wulff, G. Xxv. Zur Frage der Geschwindigkeit des Wachsthums und der Auflösung der Krystallflächen. *Zeitschrift für Kristallographie-Crystalline Materials* **34**, 449–530 (1901). (Cited on page 43.)

[71] Herring, C. Some Theorems on the Free Energies of Crystal Surfaces. *Phys. Rev.* **82**, 87–93 (1951).

[72] Herring, C. Structure and Properties of Solid Surfaces, Page 5 (Univ. of Chicago Press, Chicago, 1952).

[73] Zia, R. & Avron, J. Total surface energy and equilibrium shapes: Exact results for the d= 2 Ising crystal. *Physical Review B* **25**, 2042 (1982).

[74] Rottman, C. & Wortis, M. Statistical mechanics of equilibrium crystal shapes: Interfacial phase diagrams and phase transitions. *Physics Reports* **103**, 59–79 (1984).

[75] Wortis, M., Vanselow, R. & Howe, R. *Chemistry and Physics of Solid Surfaces, Vol. II* (Springer, Berlin, 1988). (Cited on page 43.)

[76] Zucker, R. V., Chatain, D., Dahmen, U., Hagège, S. & Carter, W. C. New software tools for the calculation and display of isolated and attached interfacial-energy minimizing particle shapes. *Journal of Materials Science* **47**, 8290–8302 (2012). (Cited on page 44.)

[77] Binder, K. Monte Carlo calculation of the surface tension for two- and three-dimensional lattice-gas models. *Physical Review A* **25**, 1699–1709 (1982). (Cited on page 44.)

[78] Schmitz, F. Dissertation. *Johannes-Gutenberg-Universität Mainz, unpublished* (2014). (Cited on pages 45, 46, and 47.)

[79] Winkler, A. Dissertation. *Johannes-Gutenberg-Universität Mainz, unpublished* (2012). (Cited on page 45.)

[80] Deb, D. *et al.* Hard sphere fluids at a soft repulsive wall: A comparative study using Monte Carlo and density functional methods. *Journal of Chemical Physics* **134**, 214706 (2011). (Cited on page 45.)

[81] Virnau, P. & Muller, M. Calculation Of Free Energy Through Successive Umbrella Sampling. *Journal of Chemical Physics* **120**, 10925–10930 (2004). (Cited on page 46.)

[82] Statt, A., Virnau, P. & Binder, K. Finite-Size Effects on Liquid-Solid Phase Coexistence and the Estimation of Crystal Nucleation Barriers. *Phys. Rev. Lett.* **114**, 026101 (2015). (Cited on pages 54 and 77.)

[83] Statt, A., Virnau, P. & Binder, K. Crystal nuclei in melts: A Monte Carlo simulation of a model for attractive colloids. *Molecular Physics* (2015). (Cited on pages 55 and 77.)

[84] Powles, J. G., Holtz, B. & Evans, W. A. B. New method for determining the chemical potential for condensed matter at high density. *Journal of Chemical Physics* **101**, 7804–7810 (1994). (Cited on page 57.)

[85] Weeks, J. D., Chandler, D. & Andersen, H. C. Role of Repulsive Forces in Determining the Equilibrium Structure of Simple Liquids. *Journal of Chemical Physics* **54**, 5237–5247 (1971). (Cited on page 58.)

[86] Zausch, J., Virnau, P., Binder, K., Horbach, J. & Vink, R. L. Statics and dynamics of colloid-polymer mixtures near their critical point of phase separation: A computer simulation study of a continuous Asakura-Oosawa model. *Journal of Chemical Physics* **130**, 064906 (2009). (Cited on page 58.)

[87] Hansen, J. & McDonald, I. *Theory of simple liquids* (3rd ed. Academic, New York, 2006). (Cited on pages 59 and 118.)

[88] Rowlinson, J. S. & Widom, B. *Molecular Theory of Capillarity* (Oxford University Press, Volume 8, 1982). (Cited on pages 70 and 72.)

[89] Binder, K., Müller, M., Schmid, F. & Werner, A. 'Intrinsic' profiles and capillary waves at interfaces between coexisting phases in polymer blends. *Advances in Colloid and Interface Science* **94**, 237 – 248 (2001).

[90] Tarazona, P. & Chacón, E. Monte Carlo intrinsic surfaces and density profiles for liquid surfaces. *Physical Review B* **70**, 235407 (2004). (Cited on page 70.)

[91] Winter, D., Virnau, P. & Binder, K. Heterogeneous nucleation at a wall near a wetting transition: a Monte Carlo test of the classical theory. *Journal of Physics: Condensed Matter* **21**, 464118 (2009). (Cited on page 70.)

[92] Schrader, M., Virnau, P. & Binder, K. Simulation of vapor-liquid coexistence in finite volumes: A method to compute the surface free energy of droplets. *Physical Review E* **79**, 061104 (2009).

[93] Block, B. J., Das, S. K., Oettel, M., Virnau, P. & Binder, K. Curvature dependence of surface free energy of liquid drops and bubbles: A simulation study. *Journal of Chemical Physics* **133** (2010). (Cited on page 70.)

[94] Filion, L., Hermes, M., Ni, R. & Dijkstra, M. Crystal nucleation of hard spheres using molecular dynamics, umbrella sampling, and forward flux sampling: A comparison of simulation techniques. *Journal of Chemical Physics* **133**, 244115 (2010). (Cited on page 79.)

[95] Schilling, T., Dorosz, S., Schoepe, H. J. & Opletal, G. Crystallization in suspensions of hard spheres: a Monte Carlo and molecular dynamics simulation study. *Journal of Physics: Condensed Matter* **23**, 194120 (2011). (Cited on page 79.)

[96] Pusey, P. N. Liquids, Freezing, and the Glass Transition, Chapter 10 (Elsevier, Amsterdam, 1991). (Cited on pages 79 and 82.)

[97] Binder, K. & Kob, W. *Glassy materials and disordered solids: An introduction to their statistical mechanics* (World Scientific, 2011). (Cited on pages 79 and 82.)

[98] Pedersen, U. R., Hummel, F., Kresse, G., Kahl, G. & Dellago, C. Computing Gibbs free energy differences by interface pinning. *Physical Review B* **88**, 094101 (2013). (Cited on page 81.)

[99] Binder, K. Simulations clarify when supercooled water freezes into glassy structures. *Proceedings of the National Academy of Sciences* **111**, 9374–9375 (2014). (Cited on page 82.)

[100] Poon, W. C. K. & Pusey, P. N. Observation, Prediction and Simulation of Phase Transitions in Complex Fluids, p. 3 (Kluwer, Dordrecht, 1995). (Cited on page 82.)

[101] Jäger, C., Bach, H. & Krause, D. *Analysis of the Composition and Structure of Glass and Glass Ceramics* (Springer, Berlin, Heidelberg, 1999). (Cited on page 82.)

[102] Henderson, J. & Sabeur, Z. Liquid-state integral equations at high density: On the mathematical origin of infinite-range oscillatory solutions. *Journal of Physics* **97**, 6750–6758 (1992). (Cited on pages 87 and 99.)

[103] Evans, D., R. Hoyle & Parry, A. Length scales for wetting transitions: Beyond the continuum Landau approximation for the interfacial binding potential. *Physical Review A* 3823 (1992).

[104] Martynov, G. A. *Fundamental theory of liquids : method of distribution functions ; translated from the Russian by Vitaly I. Kisin* (A. Hilger Bristol ; Philadelphia, 1992). (Cited on page 99.)

[105] Attard, P., Bérard, D. R., Ursenbach, C. P. & Patey, G. N. Interaction free energy between planar walls in dense fluids: An Ornstein-Zernike approach with results for Hard-Sphere, Lennard-Jones, and dipolar systems. *Physical Review A* **44**, 8224–8234 (1991).

[106] Attard, P., Ursenbach, C. P. & Patey, G. N. Long-range attractions between solutes in near-critical fluids. *Physical Review A* **45**, 7621–7623 (1992). (Cited on page 99.)

[107] Evans, R., Henderson, J., Hoyle, D., Parry, A. & Sabeur, Z. Asymptotic decay of liquid structure: Oscillatory liquid-vapour density profiles and the Fisher-Widom line. *Molecular Physics* **80**, 755–775 (1993). (Cited on pages 87 and 88.)

[108] Fisher, M. E. & Widom, B. Decay of Correlations in Linear Systems. *Journal of Chemical Physics* **50**, 3756–3772 (1969). (Cited on page 87.)

[109] Henderson, J. R. Wetting phenomena and the decay of correlations at fluid interfaces. *Physical Review E* **50**, 4836–4846 (1994). (Cited on page 87.)

[110] Baumgartl, J., Dullens, R. P. A., Dijkstra, M., Roth, R. & Bechinger, C. Experimental Observation of Structural Crossover in Binary Mixtures of Colloidal Hard Spheres. *Physical Review Letters* **98**, 198303 (2007). (Cited on pages 87 and 107.)

[111] Leote De Carvalho, R. J. F. Dissertation. *H.H Wills Physics Laboratory,University of Bristol* (1996). (Cited on pages 88 and 99.)

[112] Evans, R., Leote de Carvalho, R. J. F., Henderson, J. R. & Hoyle, D. C. Asymptotic decay of correlations in liquids and their mixtures. *Journal of Chemical Physics* **100**, 591–603 (1994). (Cited on page 88.)

[113] Dijkstra, M. & Evans, R. A simulation study of the decay of the pair correlation function in simple fluids. *Journal of Chemical Physics* **112**, 1449–1456 (2000).

[114] Grodon, C., Dijkstra, M., Evans, R. & Roth, R. Decay of correlation functions in hard-sphere mixtures: Structural crossover. *Journal of Chemical Physics* **121**, 7869–7882 (2004).

[115] Grodon, C., Dijkstra, M., Evans, R. & Roth, R. Homogeneous and inhomogeneous hard-sphere mixtures: Manifestations of structural crossover. *Molecular Physics* **103**, 3009–3023 (2005). (Cited on page 88.)

[116] Percus, J. K. & Yevick, G. J. Analysis of Classical Statistical Mechanics by Means of Collective Coordinates. *Physical Review* **110**, 1–13 (1958). (Cited on pages 88, 89, and 117.)

[117] Ornstein, L. S. & Zernike, F. Accidental deviations of density and opalescence at the critical point of a single substance. *Proceedings of the National Academy of Sciences Amsterdam* 793–806 (1914). (Cited on page 88.)

[118] Rosenbluth, M. N. & Rosenbluth, A. W. Further Results on Monte Carlo Equations of State. *Journal of Chemical Physics* **22**, 881–884 (1954). (Cited on page 89.)

[119] Wood, W. W. & Jacobson, J. D. Preliminary Results from a Recalculation of the Monte Carlo Equation of State of Hard Spheres. *Journal of Chemical Physics* **27**, 1207–1208 (1957).

[120] Alder, B. J. & Wainwright, T. E. Phase Transition for a Hard Sphere System. *Journal of Chemical Physics* **27**, 1208–1209 (1957). (Cited on page 89.)

[121] Wertheim, M. S. Analytic Solution of the Percus-Yevick Equation. *Journal of Mathematical Physics* **5**, 643–651 (1964). (Cited on pages 89 and 117.)

[122] Thiele, E. Equation of State for Hard Spheres. *Journal of Chemical Physics* **39**, 474–479 (1963).

[123] Lebowitz, J. L. Exact Solution of Generalized Percus-Yevick Equation for a Mixture of Hard Spheres. *Physical Review* **133**, A895–A899 (1964). (Cited on page 118.)

[124] Mansoori, G. A., Carnahan, N. F., Starling, K. E. & Leland, T. W. Equilibrium Thermodynamic Properties of the Mixture of Hard Spheres. *Journal of Chemical Physics* **54**, 1523–1525 (1971). (Cited on page 89.)

[125] Kirkwood, J. G. & Boggs, E. M. The Radial Distribution Function in Liquids. *Journal of Chemical Physics* **10**, 394–402 (1942). (Cited on page 89.)

[126] Piazza, R., Bellini, T. & Degiorgio, V. Equilibrium sedimentation profiles of screened charged colloids: A test of the hard-sphere equation of state. *Physical review letters* **71**, 4267 (1993). (Cited on page 89.)

[127] Hunter, G. L. & Weeks, E. R. The physics of the colloidal glass transition. *Reports on Progress in Physics* **75**, 066501 (2012). (Cited on page 90.)

[128] Carnahan, N. F. & Starling, K. E. Equation of State for Nonattracting Rigid Spheres. *Journal of Chemical Physics* **51**, 635–636 (1969). (Cited on page 90.)

[129] Hall, K. R. Another Hard-Sphere Equation of State. *Journal of Chemical Physics* **57**, 2252–2254 (1972). (Cited on page 90.)

[130] Aastuen, D. J. W., Clark, N. A., Cotter, L. K. & Ackerson, B. J. Nucleation and Growth of Colloidal Crystals. *Physical Review Letters* **57**, 1733–1736 (1986). (Cited on page 90.)

[131] Schätzel, K. & Ackerson, B. J. Observation of density fluctuations. *Physical Review Letters* **68**, 337 (1992). (Cited on page 90.)

[132] Van Megen, W., Mortensen, T., Williams, S. & Müller, J. Measurement of the self-intermediate scattering function of suspensions of hard spherical particles near the glass transition. *Physical Review E* **58**, 6073 (1998). (Cited on page 90.)

[133] Minsky, M. Confocal scanning microscope. *Rapport technique, Patent* **3** (1955). (Cited on page 91.)

[134] Minsky, M. Memoir on inventing the confocal scanning microscope. *Scanning* **10**, 128–138 (1988). (Cited on page 91.)

[135] Royall, C. P., Leunissen, M. E. & van Blaaderen, A. A new colloidal model system to study long-range interactions quantitatively in real space. *Journal of Physics: Condensed Matter* **15**, S3581 (2003). (Cited on page 96.)

[136] Perram, J. W. & Smith, E. R. The role of poles of the structure factor in determining properties of the hard sphere fluid. *Journal of Physics A: Mathematical and General* **13**, 2219 (1980). (Cited on page 97.)

[137] Martynov, G. A. & Sarkisov, G. N. Asymptotics of the correlation functions for fluids. *Journal of Chemical Physics* **93**, 3445–3451 (1990). (Cited on page 99.)

[138] Pearson, F. J. & Rushbrooke, G. S. XX.-On the Theory of Binary Fluid Mixtures. *Proceedings of the Royal Society of Edinburgh. Section A. Mathematical and Physical Sciences* **64**, 305–317 (1957). (Cited on page 102.)

[139] Rycroft, C. H. *Multiscale modeling in granular flow*. Ph.D. thesis, Massachusetts Institute of Technology (2007). (Cited on page 107.)

[140] Rycroft, C. H., Grest, G. S., Landry, J. W. & Bazant, M. Z. Analysis of granular flow in a pebble-bed nuclear reactor. *Physical review E* **74**, 021306 (2006). (Cited on page 107.)

[141] Cormen, T. H., Leiserson, C. E., Rivest, R. L., Stein, C. *et al. Introduction to algorithms*, vol. 2 (MIT press Cambridge, 2001). (Cited on page 107.)

[142] Ester, M., Kriegel, H.-P., Sander, J. & Xu, X. A density-based algorithm for discovering clusters in large spatial databases with noise. In *Kdd*, vol. 96, 226–231 (1996). (Cited on page 107.)

[143] Wertheim, M. S. Exact Solution of the Percus-Yevick Integral Equation for Hard Spheres. *Physical Review Letters* **10**, 321–323 (1963). (Cited on page 117.)

[144] Wertheim, M. S. Exact Solution of the Percus-Yevick Integral Equation for Hard Spheres. *Physical Review Letters* **10**, 321–323 (1963). (Cited on page 117.)

[145] Ashcroft, N. W. & Langreth, D. C. Structure of Binary Liquid Mixtures. I. *Phys. Rev.* **156**, 685–692 (1967). (Cited on page 120.)

LIST OF ABBREVIATIONS

MC . . . . . Monte Carlo

fcc . . . . . face centered cubic

CNT . . . . . Classical Nucleation Theory

AO . . . . . Asakura-Oosawa model

EffAO . . . . . effective Asakura-Oosawa model

softEffAO . . . . . soft effective Asakura-Oosawa model

softEffAO1 . . . . soft effective Asakura-Oosawa model with $\eta_p^r = 0.1$

softEffAO2 . . . . soft effective Asakura-Oosawa model with $\eta_p^r = 0.2$

HS . . . . . hard sphere model

PY . . . . . Percus-Yevick approximation

OZ . . . . . Ornstein-Zernike equation

PMMA . . . . . polymethylmethacrylate

TBAB . . . . . tetra-butylammonium bromide

CHB . . . . . cyclohexyl bromide